UNIVERSITÀ
DEGLI STUDI
FIRENZE

DOTTORATO DI RICERCA IN FISICA E ASTRONOMIA

CICLO XXXI

COORDINATORE Prof. Raffaello D'Alessandro

The Role of External and Endogenous Noise in Neural Network Dynamics and Statistics

Settore Scientifico Disciplinare FIS/02 Fisica teorica delle interazioni fondamentali

Dottorando
Clément Zankoc

Tutore
Prof. Roberto Livi

Prof. Duccio Fanelli

Dr. Francesco Ginelli

Coordinatore
Prof. Raffaello D'Alessandro

Anni 2015/2018

Abstract

Noise is ubiquitous, stemming from the surrounding environment or arising from the inherent stochasticity of the system under consideration. Its presence may qualitatively change the behavior of a physical system, possibly leading to surprising and unexpected phenomena, and, as such, it should be accommodated for in realistic models.

In this work, I present several models, that bear interest for neuroscience, in which noise plays a role of paramount importance. Throughout my thesis, investigations are conducted by means of both analytical and computational methods. First, I introduce, and further develop key analytical tools for tackling analytically the dynamics of a stochastic system. More specifically, I develop a perturbative technique which allows for computing the statistics of such systems even if they do not obey a gradient dynamics. Second, I focus on purely stochastic oscillators. I show that a collection of such oscillators, occupying the nodes of a generic network, can organize at the macroscopic level yielding noise-sustained spatiotemporal pattern with long-range correlations. Then, the same oscillators are organized in a directed unidirectional lattice with adjacent connections. The endogenous component of noise, coupled to a certain topology of the embedding space, seeds

a coherent amplification of the signal across the lattice. Almost periodic oscillations emerge that I thoroughly investigate. Finally, I demonstrate that the coherent amplification of an imposed noisy perturbation destabilizes the synchronous state of an ensemble made of deterministic oscillators also when a conventional linear stability analysis would deem the system resilient to small external disturbances.

A mes parents.

Declaration

This document has been composed in its totality by the candidate. No part of it has been accepted in any previous application for a degree. The work in this thesis has been done by the candidate and, in parts where work has been done with collaborators. All quotations have been distinguished by quotation marks and the sources of information specifically acknowledged.

Acknowledgements

I would firstly like to state my gratitude and my recognition towards my supervisors, Prof. Roberto Livi, Prof. Duccio Fanelli and Dr. Francesco Ginelli, for their patience, their attention, their generosity and their guidance. I am glad to have been able to work under their supervision, I have learnt so much from them both on a academic and on a human level.

I would also like to address my thanks to all the persons that made possible the COSMOS project. All along my Ph.D., I have benefited from a fantastic working environment. I had the opportunity to interact with great scientists from many different fields across the world. Thanks to all the participants of this project, it was such a rewarding experience to know all of you.

A special thank you to Giovanna and Giulia, who had the misfortune to share an office with me, for having borne me for almost two years. Thanks you Marco and Mallory for all those conversations, laughings and nice moments we have shared.

Contents

Chapter 1

Introduction

In 1827, botanist Robert Brown observed that pollen grains suspended in water were executing a jittery motion. He demonstrated that this peculiar phenomenon was not the manifestation of living mechanisms by showing that the same kind of erratic dynamics could be observed in the suspension of inorganic fine particles. It took almost 80 years including much progress in kinetic theory and statistical physics to find a satisfactory explanation for this phenomenon. In 1905 Albert Einstein published an article in which he proposed the reason behind such motion, the fine particle undergoes frequent and isotropic collisions from the molecules of the liquid in which they are suspended [1]. He pointed out that, considering the complexity of the motion and the staggering number of variables involved, a probabilistic formulation was necessary. It is worth mentioning that Smoluchowski independently gave the same explanation [2]. Subsequently after, Paul Langevin proposed a complementary approach in which he considered the dynamics of the suspended particle to be described by a differential equation containing an additional

term acting as a random force and sharing the same statistical properties as the fluctuations of the particle position [3]. This random force, here to contain all the collisions undergone by the suspended particle, may be denoted *noise*, and since it typically does not depend on the system itself, it is said to be *external*. Brownian motion is the seminal example of a ubiquitous phenomenon: doubtlessly there is all but one physical system perfectly isolated and "external noise" takes on the role of an environment that is unpredictable and incoherent due to its vast number of degrees of freedom. Take the radio as an example: many of us experienced this unpleasant background crackling when listening to it. There, noise takes its origin from the pollution of the signal by all the natural electromagnetic processes in the atmosphere and the interferences from other man-made radio signals.

I mentioned external noise, induced by interaction with the outside environment. However, most physical systems are inherently stochastic, either at the fundamental level or by the level of description one chooses (i.e. population dynamics). In this thesis, I will primarly focus on the latter. Let me clarify what I mean by "level of description". Every system which involves entities in limited number, such as reactants for chemical reactions or animals for ecological systems, can be described at a coarse-grained level by average population densities. In this coarse-grained approach, either one opts for a deterministic description by ordinary differential equations (ODEs) and therefore disregard populations' fluctuations, or one can probe the system at an intermediate scale taking into account its finite nature and the discreteness of its dynamics. The first option works well when the quantities in play are large in numbers, but, and this constitutes one of the major point of my

thesis, it lacks of accuracy for small size systems, where intrinsic fluctuations may have remarkable effects that can qualitatively alter deterministic predictions. There, the system is subject to its own fluctuations, which take on the form of an endogenous noise term, which turns the mean field ordinary differential equations (ODEs) into stochastic differential equations (SDEs). This endogeneus noise can be *multiplicative*. Due to the central limit theorem, it vanishes for large particles numbers, $N \to \infty$, scaling as $1/\sqrt{N}$, so that in the thermodynamic limit the purely deterministic mean-field descriptions is recovered [4, 5]. It therefore becomes vital to use the stochastic formalism to study these systems. This allows for making explicit the contribution of endogenous noise for a system initially given in terms of birth-deat equations. A detailed description of this procedure will be given in the second chapter, where I will derive the correct form of this endogenous noise term through an original perturbative approach.

Most of this thesis, however, is concerned with the following question: what is the role played by noise in a mesoscopic level description regardless of its nature? Often seen as a disturbance limiting the efficiency of the system under consideration, noise may play an operative role: stochastic resonance, noise-induced transitions or coherence resonance are just a few important examples [6, 7, 8]. I will stress this point notably by showing how noise can shift bistability bifurcation points and can lead to pattern formation with long distance correlations or even sustain macroscopic oscillations instead of the trivial fixed point dynamics achieved in the thermodynamic limit. I will also show how certain non-normal network topologies are capable of largely amplify arbitrarily small stochastic terms. These results are significant, as

they show that properly taking into account stochastic corrections – often of endogenous type – can *qualitatively* alter the deterministic mean-field dynamics. To elaborate along these lines, I will consider a set of models related to neuroscience.

The thesis work consists in four main chapters.

- In the second chapter, I will introduce the Wilson-Cowan (WC) model which provides a coarse-grained representation of a simplified visual cortex model, where two populations of neurons, excitatory and inhibitory ones, interact through idealized feedback synaptic loops [9, 10]. Then, I will provide an inventory of tools to perform a mesoscopic investigation of a system which carries finite-size populations of neurons. To test for the consistency of the calculations, I will compute the stationary probability distribution for both species under study in a region where the system displays bistability, and to compare it with simulations performed using Gillespie algorithm [11]. I observed that noise extends the region of effective bistability. More importantly, I will present a pertubative technique that allows for pursuing analytical calculations despite the non-potential nature of the system.

- In the third chapter, I will consider a reduced version of the WC model. This time the system under consideration displays purely stochastic oscillations or quasi-cycles that I will fully characterize by means of the power spectral density matrix [12, 13, 14]. The same tool suits to demonstrate that a collection of such stochastic oscillators disposed over a network may become coherent resulting in spatiotemporal patterns, where contiguous nodes are in anti-phase. This result stresses

that fluctuations, endogenous or external, may contribute to the processing of information or to the spatiotemporal organization of physical systems.

- In the fourth chapter, I will study this reduced WC model in a feedforward unidirectional chain. Starting from a trivial fixed point behavior, which characterizes the mean field deterministic dynamics, I observed both an amplification and a modulation of arbitrarly small stochastic oscillations (due to either internal or external noise) along the chain. Indeed, these oscillations converge towards a limit cycle dynamics with a well-defined frequency. After quantifying and explaining those phenomena, I will present a few possible applications for such a pacemaking system and give its thermodynamic interpretation.

- In the fifth chapter, I will keep the unidirectional chain topology but replace the stochastic oscillators with Ginzburg-Landau oscillators disturbed by external noise. The same amplification takes place for the fluctuations normal to the limit cycle. This destabilizes the fully synchronized solution and leads to pattern formation, which is not expected using linear stability analysis.

- In the final section I will draw my conclusions, highlight the most important results of my work and suggest future developments.

Chapter 2

Endogenous noise in neural system

In this chapter we consider a stochastic version of the Wilson-Cowan model which accommodates for discrete populations of excitatory and inhibitory neurons. The model assumes a finite carrying capacity, namely that the maximum population size of the populations that its environment can sustain indefinitely in time is finite. The master equation that governs the dynamics of the stochastic model is analyzed by an expansion in powers of the inverse population size, yielding a coupled pair of non-linear Langevin equations with multiplicative noise. Gillespie simulations show the validity of the obtained approximation, for the parameter region where the system exhibits dynamical bistability. We report analytical progress by silencing the retroaction of excitatory neurons on inhibitory neurons, while still assigning the parameters so as to fall in the region of deterministic bistability for the excitatory species. The proposed approach forms the basis of a perturbative generalization which

applies to the case where a modest degree of coupling is restored.

2.1 Neural population dynamics: Wilson-Cowan model

Neural models aim at elucidating the grounding architecture that regulates information processing in biological systems [15]. The level of abstraction that is accommodated for in the chosen mathematical scheme reflects the specific topic under investigation. Detailed single neurons models can be devised, which account for the sharp changes in the action potential. The number of neurons in the human cortex is extraordinarily large and for many practical aspects a bottom-up approach that moves from a detailed representation of each individual unit is virtually impracticable. The physiology of neurons is also quite intricate. A single neuron receives input from thousands of axon terminals coming from other neurons, but the inherent degree of redundancy contributes to drastically reduce the effective connections to a limited subset. Irrespective of their intimate characteristics, neurons can be pictured as complex switching devices organized, in the simplest scenario, in two macroscopic families of homologous constituents, *excitatory* and *inhibitory* neurons. This enables, in turn, to climb the hierarchy of complexity, and elaborate, to a suitable level of coarse graining, on the interlaced dynamics of homogenous populations of neurons. Several approaches have been indeed proposed in the literature to reduce the dynamics of individuals neurons interacting via pulse-like signals to low dimensional systems characterized by few collective variables [16, 17, 18, 19, 20]. The WilsonCowan (WC) [9, 10]

model and its further extensions [21] provide an interesting, although highly idealized, arena to shed light onto the complex dynamics of a multi-species neuronal system. The model displays limit cycle behavior, mimicking neural oscillations. Stimulus-dependent evoked responses are also predicted, as well as the existence of multiple stable states. The original WC model is deterministic in nature and the average concentration of active/inactive excitatory/inhibitory neurons appear to be self-consistently ruled by a pair of coupled ordinary differential equations. A schematic representation of this version of the WC is given in Figure 2.1. It has been used to predict the qualitative and quantitative features of epileptiform activity especially the propagation speed of epileptic seizures which is slower than normal brain wave activity [22]. Spatially extended versions of the model can be designed which in turn amount to operate with partial differential equations [23].

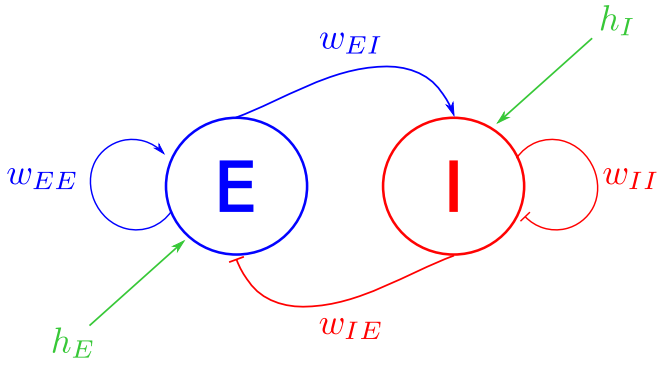

Figure 2.1: Schematic view of the Wilson-Cowan model. Here E stands for excitatory neurons population while I stands for inhibitory. Inhibitory and excitatory interactions as displayed in the figure are controlled by a set of positive constants $w_{\cdot}$. The coefficients h represent eventual input currents from the outside.

2.2 On the stochastic model

As said, the WC model has originally been formulated as a deterministic model. Here, we want to understand the particular role played by intrinsic perturbations [1], stemming from the intimate discreteness of the system under scrutiny. Individual-based effects should be taken into account in any sensible model of natural phenomena; this yields to an endogenous stochastic contribution. At first sight it might appear surprising that stochastic effects are important when the interacting populations consist of a large number of individual constituents. Populations fluctuations can however amplify through resonant effects [24] and drive the spontaneous emergence of collective macroscopic patterns, both in time [25, 26] and in space [27, 28, 29, 30, 31], marking a clear distinction between stochastic and deterministic viewpoints. Endogenous noise can be certainly relevant to neural systems [32]. Channel noise arising from the variability in the opening and closing of a finite number of ion channels, is a microscopic source of intrinsic disturbance. At the population level, the instantaneous state of the system is drawn by looking at the number of active neurons, which are in on a given patch. The evolution of the inspected system can be monitored via a suitably defined master equation, the mean field deterministic picture being eventually recovered in the thermodynamic limit. Following these lines of reasoning, the WC model has been recently revised under the generalized stochastic angle. This allows for understanding on the specific traits which ultimately emanates from the endogenous component of the noise[33].

[1] A point that we need to clarify before pursuing is that many deterministic systems may look as if they were stochastics (set of inhomogeneously connected oscillators,...). It is important to not confound erratic behaviour with stochasticity.

We will first write the dynamics of our system in terms of chemical rate equations with non-linear transition rates. By means of step operators, the obtained master equation will then be expanded in powers of the inverse population size so to yield a Fokker-Planck equation giving an approximate stochastic description for the density of the interacting species. The final step will consist of mapping it onto a pair of non-linear Langevin equations with multiplicative noise.

2.2.1 Birth and death reactions

In the historical derivation of the WC model, neurons are divided into two classes, *excitatory* and *inhibitory*. Within those populations, we consider two subpopulations, one is called *active* (a) and can be viewed as the fraction of neurons that are spiking, the other is called *inactive* or *quiescent* (q) and refers to neurons at rest. It is worth emphasizing that it defines a minimal setting for carrying out the future analysis. Other effects, like time delays, could be possibly invoked, so yielding a generalization of the aforementioned framework (by e.g. motivating the introduction of a third distinct subpopulation, that of the refractary neurons) [34].

In the following, individual excitatory and inhibitory neurons will be respectively identified with the symbols X and Y. To identify to which subpopulation a neuron belongs, the quantities X and Y will be decorated with the index a or q. More concretely, we will denote by X_a (resp. Y_a) an activated neuron of the excitatory type (resp. inhibitory), whereas X_q (resp. Y_q) identifies a quiescent excitatory (resp. inhibitory) neuron. The stochastic dynamics of the system is ruled by a minimal set of birth and death reactions,

as summarized in the following:

$$\begin{array}{lll} X_q & \xrightarrow{f_E[s_E]} & X_a \\ X_a & \xrightarrow{\alpha_E} & X_q \\ Y_q & \xrightarrow{f_I[s_I]} & Y_a \\ Y_a & \xrightarrow{\alpha_I} & Y_q \end{array} \tag{2.1}$$

where $\alpha_{E,I}$ are constant rate function; $f_{E,I}(\cdot)$ are non-linear firing rates, sigmoid in shape, function of the synaptic currents $s_{E,I}$, and bound to the interval $[0, 1]$. Before completing the description of the elements that define the stochastic model, we remark that, by definition, the number of excitatory (resp. inhibitory) neurons, N (resp. M), is an invariant quantity. Label with n_{X_a} the number of neurons of the type X_a, and with n_{X_q} the number of elements X_q. Clearly, by virtue of equations (2.1), $n_{X_a} + n_{X_q} = N$. Similarly, and with an obvious meaning of the involved notation $n_{Y_a} + n_{Y_q} = M$. Simply stated, the conservation laws that we have here identified enable one to reduce to a total of two the number of independent variables that uniquely lay out the dynamics of the system. The idealized synaptic currents, as introduced in [9], read:

$$\begin{aligned} s_E &= w_{EE}\frac{n_{X_a}}{N} - w_{EI}\frac{n_{Y_a}}{M} + h_E \\ s_I &= w_{IE}\frac{n_{X_a}}{N} - w_{II}\frac{n_{Y_a}}{M} + h_I \end{aligned} \tag{2.2}$$

where the weights w_{kl} are positive defined for any $k, l = E, I$. s_E (resp. s_I) stands for the idealized synaptic current received by the excitatory (resp. inhibitory) populations of neurons, since all the coefficients w_{kl} are positively defined it becomes clear that the more the coefficient w_{EE} (resp. w_{IE}) is large, the more activated excitatory neurons will have a tendency to activate

quiescent excitatory (resp. inhibitory) neurons. On the contrary, the more w_{EI} (resp. w_{II}) is large, the more the activated inhibitory neurons will prevent excitatory (resp. inhibitory) neurons from activating. The constants h_E and h_I encode the interaction of the examined families of neurons with the surrounding environment. These synaptic currents are then mediated by a sigmoid function to compute the mean rate of activation for both populations of neurons. The specific form of the sigmoid function $f_k(s_k)$, with $k = E, I$ is not essential for the forthcoming discussion.

2.2.2 Master equation

The chemical equations introduced above define a *continuous-time Markov process* which means that the probability of the system to be in state (x, y) at time t solely depends on the (immediate) preceding state as reached by the system. A probabilistic approach is necessary to understand such process. The dynamics of the probability $P(x, t)$ of seeing the system in a given state at a given time can be described by means of a Master equation. A general form of the Master equation is given below

$$\frac{\partial P(\mathbf{x}, t)}{\partial t} = \sum_{\mathbf{y} \neq \mathbf{x}} [P(\mathbf{y}, t)T(\mathbf{x}|\mathbf{y}) - P(\mathbf{x}, t)T(\mathbf{y}|\mathbf{x})] \tag{2.3}$$

where $\mathbf{x}$,$\mathbf{y}$ denote two distinct states of the system and $T(\mathbf{x}|\mathbf{y})$ is the transition rate from state $\mathbf{x}$ to state $\mathbf{y}$. We can distinguish 8 possible transitions

for our system, each associated to a specific transition rate

$$\begin{array}{ll} T_1 : (x + \frac{1}{N}, y) \to (x, y) & T_2 : (x - \frac{1}{N}, y) \to (x, y) \\ T_3 : (x, y + \frac{1}{M}) \to (x, y) & T_4 : (x, y - \frac{1}{M}) \to (x, y) \\ T_5 : (x, y) \to (x - \frac{1}{N}, y) & T_6 : (x, y) \to (x + \frac{1}{N}, y) \\ T_7 : (x, y) \to (x - \frac{1}{M}, y) & T_8 : (x, y) \to (x, y + \frac{1}{M}) \end{array} \tag{2.4}$$

where we have introduced the number density $x = n_{X_a}/N$ and $y = n_{Y_a}/M$. We further label with $P(x, y, t)$ the probability of seeing the system in the state (x, y), at time t. In our case, the Master equation reads

$$\begin{aligned} \frac{\partial P(x,y,t)}{\partial t} = [& -T_1(x + \tfrac{1}{N}, y|x, y)P(x, y, t) - T_2(x - \tfrac{1}{N}, y|x, y)P(x, y, t) \\ & -T_3(x, y + \tfrac{1}{M}|x, y)P(x, y, t) - T_4(x, y - \tfrac{1}{M}|x, y)P(x, y, t) \\ & +T_5(x, y|x - \tfrac{1}{N}, y)P(x - \tfrac{1}{N}, y, t) + T_6(x, y|x + \tfrac{1}{N}, y)P(x + \tfrac{1}{N}, y, t) \\ & +T_7(x, y|x, y - \tfrac{1}{M})P(x, y - \tfrac{1}{M}, t) + T_8(x, y|x, y + \tfrac{1}{M})P(x, y + \tfrac{1}{M}, t)] \end{aligned} \tag{2.5}$$

The Master equation then be reformulated in a compact form involving the so called step operators $\epsilon_x^{\pm}$ and $\epsilon_y^{\pm}$ defined as:

$$\begin{aligned} \epsilon_x^{\pm} f(x) &= f(x \pm \tfrac{1}{N}) \\ \epsilon_y^{\pm} f(y) &= f(y \pm \tfrac{1}{M}) \end{aligned} \tag{2.6}$$

They allow to reduce the number of distinct transition rates since

$$\begin{array}{lllll} T_5(x, y|x - \frac{1}{N}, y) & = & \epsilon_x^- T_1(x + \frac{1}{N}, y|x, y) & = & (1 - x)f_E(x, y) \\ T_6(x, y|x + \frac{1}{N}, y) & = & \epsilon_x^+ T_2(x - \frac{1}{N}, y|x, y) & = & \alpha_E x \\ T_7(x, y|x, y - \frac{1}{M}) & = & \epsilon_y^- T_3(x, y + \frac{1}{M}|x, y) & = & (1 - y)f_I(x, y) \\ T_8(x, y|x, y + \frac{1}{M}) & = & \epsilon_y^+ T_4(x, y - \frac{1}{M}|x, y) & = & \alpha_I y \end{array} \tag{2.7}$$

Therefore, one can re-write the Master equation in the following form:

$$\begin{aligned} \frac{\partial P(x,y,t)}{\partial t} &= [(\epsilon_x^- - 1)T_1 + (\epsilon_x^+ - 1)T_2 \\ &\quad (\epsilon_y^- - 1)T_3 + (\epsilon_y^+ - 1)T_4]P(x,y,t) \end{aligned} \tag{2.8}$$

The Master equation (2.8) provides an exact description of the Markov dynamics. We'll see that will be able to extract from it both the ideal mean field dynamics (formally recovered in the limit of infinite system size) and the associated finite-size corrections.

In most cases, the Master equation cannot be solved analytically. Two options are then available: we can resort to analytical techniques to obtain an approximate solution or we can employ numerical methods to shed light onto the system under inspection. The first option will be dealt with in the following sections. The second one is based, for example, on the Gillespie algorithm which enables one to generate trajectories of the underlying stochastic dynamics, which are consistent with the governing master equation [11]. An important fraction of the numerical results displayed within this thesis, make use of the Gillespie algorithm. More details on the implementation of the algorithm, as well on the mathematical foundation, are given in Appendix A.

2.2.3 Kramers-Moyal expansion

To pursue our analytical investigations, we seek to approximate the exact Master equation, via the Kramers-Moyal perturbative recipe [35, 36, 37, 38, 39]. To this end we first Taylor expand the step operators (assuming $1/N$

and $1/M$ small) up to the second order in $\frac{1}{N^2}$[2] and get:

$$\begin{aligned}\epsilon_x^{\pm} f(x) = f(x \pm \tfrac{1}{N}) \approx (1 \pm \tfrac{1}{N}\tfrac{\partial}{\partial x} + \tfrac{1}{2N^2}\tfrac{\partial^2}{\partial x^2} + \dots) f(x) \\ \epsilon_y^{\pm} f(y) = f(y \pm \tfrac{1}{M}) \approx (1 \pm \tfrac{1}{M}\tfrac{\partial}{\partial y} + \tfrac{1}{2M^2}\tfrac{\partial^2}{\partial y^2} + \dots) f(y)\end{aligned} \tag{2.9}$$

Then, inserting in the Master equation and performing the following time rescaling $\tau = Nt$, one eventually obtains

$$\begin{aligned}\frac{\partial P(x,y,t)}{\partial \tau} &= [(-\frac{\partial}{\partial x} + \frac{1}{2N}\frac{\partial^2}{\partial x^2})T_1 + (\frac{\partial}{\partial x} + \frac{1}{2N}\frac{\partial^2}{\partial x^2})T_2 \\ &\quad (-\frac{1}{\gamma}\frac{\partial}{\partial y} + \frac{1}{\gamma^2}\frac{1}{2N}\frac{\partial^2}{\partial y^2})T_3 + (\frac{1}{\gamma}\frac{\partial}{\partial y} + \frac{1}{\gamma^2}\frac{1}{2N}\frac{\partial^2}{\partial y^2})T_4]P(x,y,t)\end{aligned} \tag{2.10}$$

where $\gamma = M/N$ measures the relative population of inhibitors over activators. This is a two dimensional Fokker-Planck equation, which we shall write in a more transparent form by introducing the vector $\mathbf{x} = (x, y)$. In formulae:

$$\frac{\partial P(\mathbf{x},t)}{\partial \tau} = -\sum_i \left[\frac{\partial}{\partial x_i} A_i(\mathbf{x}) P(\vec{x},t)\right] + \frac{1}{2N}\sum_{i,j}\frac{\partial}{\partial x_i}\frac{\partial}{\partial x_j}\left[B_{ij}(\mathbf{x})P(\mathbf{x},t)\right] \tag{2.11}$$

where A is called the drift vector and B the diffusion matrix. They are respectively given by

$$A = \begin{bmatrix} T_1 - T_2 \\ \frac{1}{\gamma}(T_3 - T_4) \end{bmatrix} \quad , \quad B = \begin{bmatrix} T_1 + T_2 & 0 \\ 0 & \frac{1}{\gamma^2}(T_3 + T_4) \end{bmatrix} \tag{2.12}$$

[2]Here, the truncation has been done with out preliminary verification.

2.2.4 Langevin equation

While the Fokker-Planck equation reflects the statistical evolution of our system, it is also interesting to look at individual stochastic trajectories. To this aim we invoke the well known equivalence between a Fokker Planck equation and its associated Langevin description [40, 41]. To this end, we also need to choose the most convenient stochastic calculus. We decide to pick the Itô description for two reasons; because it implies simpler calculations, and more importantly because it shows good agreement with the simulations performed using the Gillespie algorithm. This was expected since the Itô convention is often used to describe stochastic processes discrete in time and that the Gillespie scheme is itself a discrete time algorithm. Hereinafter, we are always going to use the Itô description. Please refer to Appendix B for more information. This leads to the following system of non-linear Langevin equations

$$\begin{aligned} \dot{x} &= -\alpha_E x + (1-x) f_E(x,y) + \tfrac{1}{\sqrt{N}} \sqrt{\alpha_E x + (1-x) f_E(x,y)}\, \eta_1 \\ \dot{y} &= \tfrac{1}{\gamma} \left(-\alpha_I y + (1-y) f_I(x,y)\right) + \tfrac{1}{\sqrt{\gamma N}} \sqrt{\alpha_I y + (1-y) f_I(x,y)}\, \eta_2 \end{aligned} \tag{2.13}$$

where η_i stands for a *Gaussian white noise* process with zero mean and delta correlated in time $\langle \eta_i(t)\eta_j(t')\rangle = \delta_{ij}\delta(t-t')$, with $i,j = 1,2$. Also we have

$$f_E(x,y) = f_E^{(1)} + f_E^{(2)} \tanh(\beta_E s_E) \tag{2.14a}$$

$$f_I(x,y) = f_I^{(1)} + f_I^{(2)} \tanh(\beta_I s_I) \tag{2.14b}$$

where $s_{E,I}$ are the idealized synaptic currents introduced previously and which depends on the parameters w_{kl} and $h_{E,I}$, the coefficients $\beta_{E,I}$ are called the slope parameters.

We have hence obtained a system of non-linear Langevin equations that constitute the fluctuating hydrodynamics approximation of the exact Markov dynamics. Note that the noise is *multiplicative*: the amplitude of the stochastic perturbation is self-consistently adjusted, as function of the density of the simultaneously evolving species.

2.3 Effects of noise

2.3.1 Thermodynamic limit

Before pursuing our investigations on the role played by endogenous fluctuations we must better understand the deterministic dynamics of the system. We consider the thermodynamic limit $N \to \infty$ (at constant γ). The noise term vanished and one recovers a slightly modified version of the classic WC model

$$\begin{aligned} \dot{x} &= -\alpha_E x + (1-x) f_E(x,y) \\ \dot{y} &= \tfrac{1}{\gamma}\left(-\alpha_I y + (1-y) f_I(x,y)\right) \end{aligned} \tag{2.15}$$

As compared to the original WC formulation, the first (resp. second) equation of (2.15) displays an additional factor $(1-x)$ (resp. $(1-y)$), which multiplies the sigmoid function f_E (resp. f_I). This term reflects the finite carrying capacity of the system, as imposed at the microscopic level: working under diluted condition, i.e. assuming $x, y << 1$ one readily converge to an other version of the WC model [32]. Based on the choice made for the

parameters (ω_{kl}, $\alpha_{E,I}$, $h_{E,I}$, $\beta_{E,I}$, and $f^{(1,2)}_{E,I}$) the system may evolve toward a single fixed point, present multiple fixed points with their associated basins of attraction or even exhibits an oscillatory periodic attractor. In this chapter, we will be primarily interested in a parameter setting that yields bistability. As illustrated in Figure 2.2, the system possesses two attractive fixed points (green dots), which are separated by an unstable saddle point (not displayed). Deterministic WC trajectories are asymptotically attracted towards one of the stable equilibria, depending on their initial condition. The dynamics of the system in the thermodynamic limit is therefore quite trivial. We will show that the stochastic corrections, presently silent, are going to reestablish the dynamics.

2.3.2 Effect of endogeneous noise

More rich is the dynamics of the WC model in its stochastic representation: endogenous noise drives seemingly erratic transitions between the two, deterministically stable, fixed points. This picture is exemplified in Figure 2.3, where the time evolution of species x is plotted. This is an individual trajectory obtained upon integration of the Markov WC model via the already mentioned Gillespie algorithm which belongs to the Monte Carlo class of algorithm. At each iteration two random numbers are generated; one to decide, depending on the transition rates, which will be the next reaction to occur, and the second to determine the timestep increment. More details on the Gillespie algorithm are given in Appendix A.

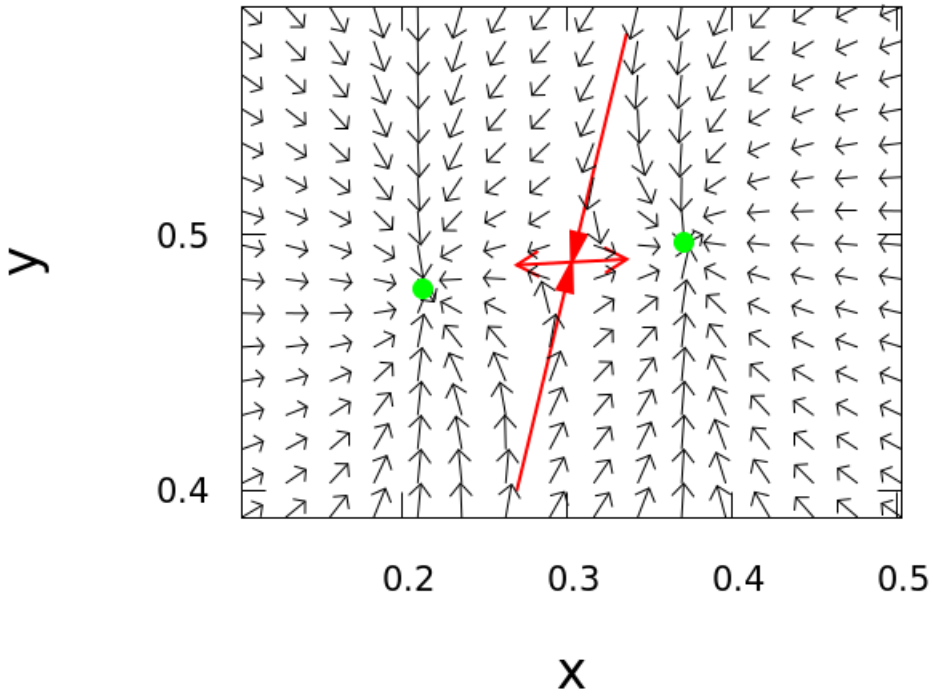

Figure 2.2: The phase space of the deterministic WC model is displayed. The (green) filled circles stands for the stable fixed points. Large (red) arrows represent the stable and unstable manifolds of the saddle node (not displayed). Tiny (black) arrows provide a quantitative description of the velocity vector field of the model in its deterministic limit. Here, $f_{E,I} = f_{E,I}^{(1)} + f_{E,I}^{(2)} \tanh(\beta_{E,I} s_{E,I})$ where β is the gain parameter. The quantities $f_{E,I}^{(1)}$ and $f_{E,I}^{(2)}$ enters in the definition of the sigmoid non-linear function and allow for a swift control of the location of the fixed points. The offset $f_{E,I}^{(1)}$ sets in particular the degree of residual activity when $s_{E,I} = 0$. The parameters here employed read $w_{II} = 1$, $w_{IE} = 0.5$, $w_{EI} = 2$, $w_{EE} = 7.2$, $\alpha_E = 1.5$, $\alpha_I = 0.4$, $h_E = 1.2$, $h_I = 0.1$, $N = 300$, $\gamma = 0.25$, $\beta_E = 3.7$, $f_E^{(1)} = 0.25$, $f_E^{(2)} = 0.65$, $\beta_I = 1$, $f_I^{(1)} = 0.5$, $f_I^{(2)} = 0.5$.

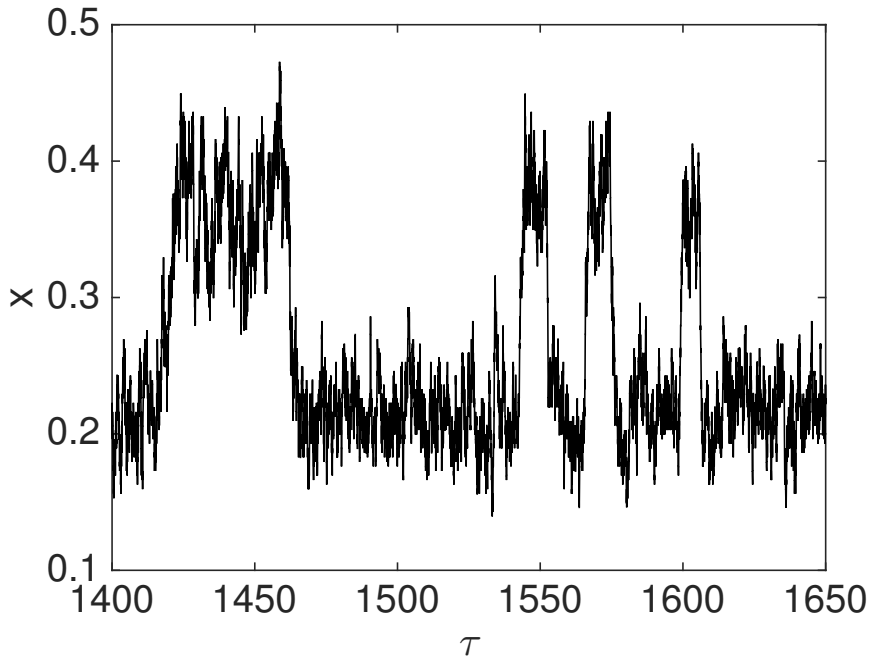

Figure 2.3: The number density $x = n_{X_a}/N$ is plotted versus time. The time series is obtained as an individual realization of the stochastic WC model, integrated via the Gillespie Monte Carlo scheme. The parameters are set as in figure 2.2

To test the adequacy of the approximate Langevin description, we conducted a series of numerical simulations. The distribution $P(x)$ (resp. $P(y)$) as obtained via the Gillespie algorithm [11], in accordance with the exact governing master equation, are displayed in Figure 2.4, with (cyan) symbols. The same quantities computed via a direct integration of the Langevin equation is depicted with (light purple) diamonds [42] . The agreement is very good and points to the validity of the approximate Langevin picture. The multiplicative component of the noise is essential to reach this level of correspondence at moderate system sizes. $P(x)$ shows the typical bimodal distribution, signature of a bistable dynamics. Conversely, at this noise level

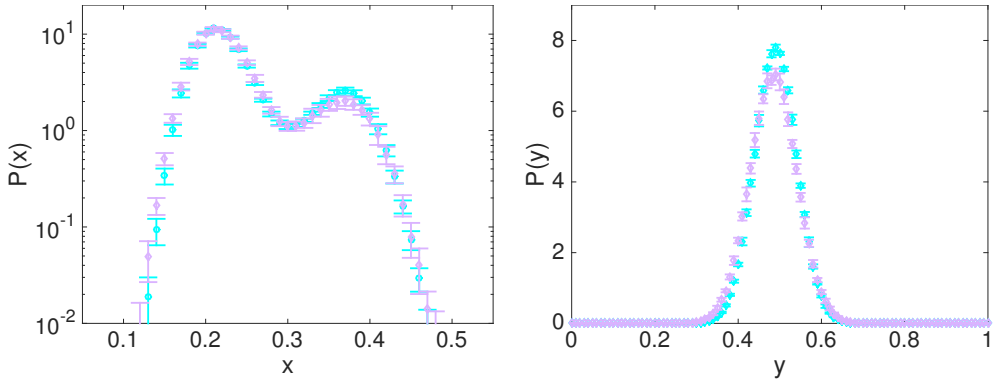

Figure 2.4: Left panel: the distribution $P(x)$ is plotted versus x in semi-logarithmic scale. The (cyan) circles refer to the exact, Gillespie based, stochastic simulation. The error bars are computed by averaging over 10 independent realizations. The (light purple) diamonds are obtained by integrating numerically the approximate Langevin equations (2.13) via a standard Euler-Maruyama scheme and averaging over 10 independent realizations. Right panel: $P(y)$ is plotted versus y. The choice of symbols (and colors) follows that of the left panel.

the two bumps of $P(y)$ merge together in a unique isolated crest.

After this preliminary analysis, the remaining part of this chapter is devoted to analytically characterizing the above probability distributions in the region of bistability. We will in particular start to explore a simplified setting, which ignores the excitatory feedback on the inhibitors population (w_{EI}). By operating in this context, one can significantly reduce the complexity of the model: the two governing Langevin equations, as obtained under the Kramers-Moyal expansion, will be packed in just one stochastic differential equation for the excitatory species. Remarkably, the inhibitors will be shown to affect the amplitude of the multiplicative noise, and thus magnify the stochastic component of the excitatory dynamics.

In principle, the coupled non-linear Langevin equations introduced above could be studied by resorting to methods from multiscale stochastic analysis [43]. The two aforementioned equations define a paradigmatic example of a stochastic system with different temporal scales, γ acting in this respect as a crucial parameter.

2.4 Analytical characterization of the distribution: the case w_{IE}=0

The aim of this section is to proceed further in the study of the fluctuating hydrodynamics of the WC model. We will start from the Langevin equations (2.13), which proved adequate versus numerical simulations of the underlying Markov process, to build up an approximate analytical solution for the distribution of of the stochastic variables x and y. To pursue this objective we shall specialize first on the simplified setting that is recovered when $\omega_{IE} = 0$. In concrete, we will ignore the action of the activators over the inhibitors, while still constraining the system to evolve in the region of deterministic bistability for the excitatory species. The concentration of the inhibitors will instead converge to a stationary stable fixed point, in the mean field limit. This is a definite simplification which enables us to reduce the system to just one Langevin equation for the excitatory species. In Figure 2.5 the phase space portrait of the system as obtained under these operating condition is outlined. The two stable fixed points (represented as green filled circles) lie horizontally, since, by construction, they display an identical value of inhibitory concentration.

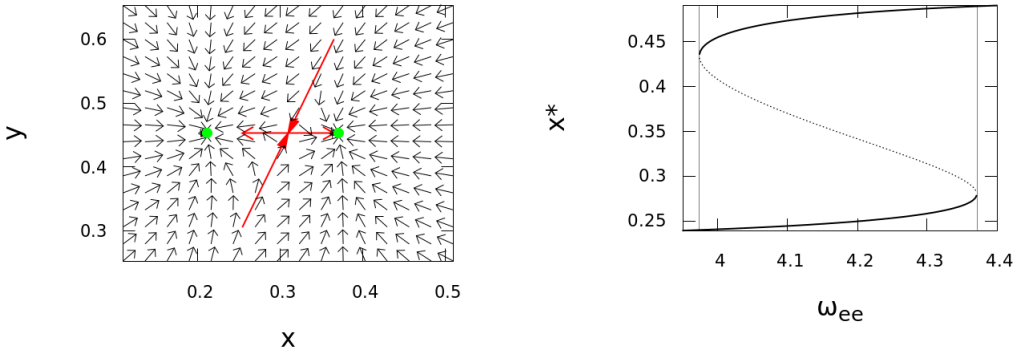

Figure 2.5: The phase space of the deterministic WC model is displayed. The (green) filled circles identify the location of the stable fixed points. Large (red) arrows stands for the stable and unstable manifolds of the saddle node (not shown). Tiny (black) arrows represents the vector field of the model. The parameters are set as in Figure 2.2, except for $w_{IE} = 0$. Right panel: the excitators xed $\bar{x}$ point is plotted as function of w_{EE} to visualize the region of bistability. Solid traits stand for the stable branch, dashed line for the unstable one.

For convenience, we write the Langevin equations (2.13) in the compact form

$$\begin{aligned} \dot{x} &= A(x,y) + \tfrac{1}{\sqrt{N}}\sqrt{B(x,y)}\,\eta_1 \\ \dot{y} &= \tfrac{1}{\gamma}\left(C(y) + \tfrac{1}{\sqrt{N}}\sqrt{D(y)}\,\eta_2\right) \end{aligned} \tag{2.16}$$

with:

$$\begin{aligned} A(x,y) &= -\alpha_E x + (1-x) f_E(x,y) \\ B(x,y) &= \alpha_E x + (1-x) f_E(x,y) \\ C(y) &= -\alpha_I y + (1-y) f_I(y) \\ D(y) &= \alpha_I y + (1-y) f_I(y) \end{aligned} \tag{2.17}$$

and where $C(\cdot)$ and $D(\cdot)$ are just function of y. To proceed in the analysis we take advantage of the fact that y has a peaked distribution, under the

chosen operating conditions. More precisely, we will operate under the small noise approximation. To that end, we first proceed to the following change of variable:

$$y = \bar{y} + u \tag{2.18}$$

where $\bar{y}$ solves the mean field equilibrium condition $C(\bar{y}) = 0$ and u encodes for the stochastic contribution. This yields to

$$\dot{u} \;=\; \tfrac{1}{\gamma}\left(C(\bar{y}+u) + \tfrac{1}{\sqrt{N}}\sqrt{D(\bar{y}+u)}\,\eta_2\right) \tag{2.19}$$

where $\langle \eta_2(t)\eta_2(t')\rangle = \delta(t-t')$. We then expand for u[3] and arrest the perturbative calculation at the first order. In formulae one readily gets:

$$\dot{u} = \frac{1}{\gamma}\left(\partial_y C|_{\bar{y}}\, u + \frac{1}{\sqrt{N}}\sqrt{D(\bar{y})}\eta_2\right) \tag{2.20}$$

This is a linear Langevin equation for the variable u which stationary probability distribution reads

$$P(u) = \mathcal{N}\exp\left(-\frac{1}{2\sigma^2}u^2\right) \tag{2.21}$$

where $\mathcal{N}$ stands for a proper normalization constant and σ denotes its variance which itself reads

$$\sigma^2 = -\frac{D(\bar{y})}{2N\gamma\partial_y C|_{\bar{y}}} \tag{2.22}$$

We can then easily compute, $P(y)$, the probability distribution of inhibitory

[3]The expansion may seem not valid since u is an unbounded variable. The a posteriori results will tend to justifiy this perilous operation.

neurons, that takes the followin form:

$$P(y) = \mathcal{N} \exp\left(-\frac{1}{2\sigma^2}\left(y - \bar{y}\right)^2\right) \tag{2.23}$$

Let us now return to the first of equations (2.16) and assume, in light of the above, we decide to write $y \simeq \bar{y} + \sigma\eta_3$, where η_3 is a normally distributed random variable, with zero mean and variance equal to one. Expanding the Langevin equation for x at the first order in the stochastic perturbation v one obtains

$$\dot{x} = A(x, \bar{y}) + \partial_y A|_{\bar{y}} \sigma\eta_3 + \frac{1}{\sqrt{N}}\sqrt{B(x, \bar{y})}\,\eta_1 \tag{2.24}$$

This is a non-linear stochastic equation with two distinct noise sources, which can be combined by using the sum rule for Gaussian variables yielding the more compact expression:

$$\dot{x} = A(x, \bar{y}) + \frac{1}{N}\sqrt{-\frac{D(\bar{y})}{2\gamma\partial_y C|_{\bar{y}}}\left(\partial_y A|_{\bar{y}}\right)^2 + B(x, \bar{y})}\,\xi \tag{2.25}$$

where ξ is a Gaussian white noise with zero mean and variance equal to one. Note that the derivative $\partial_y C|_{\bar{y}}$ is negative, leaving the term under the square root to be always positive. The dynamics of the activator species is therefore ruled by a non-linear Langevin equation, endowed with a multiplicative noise term, whose amplitude encodes, at this order of approximation, for the inhibitors contribution. The strength of the noise is modulated by γ. Decreasing the ratio M/N, which in turn signifies reducing the relative weight of inhibitory over excitatory neurons, enhances the degree of effective stochas-

ticity. It is possible to obtain an equivalent Fokker-Planck equation:

$$\frac{\partial P(x,t)}{\partial t} = -\frac{\partial}{\partial x}\left[A(x,\bar{y})P(x,t)\right] + \frac{1}{2}\frac{\partial^2}{\partial x^2}\left[\Gamma(x)P(x,t)\right] \tag{2.26}$$

where:

$$\Gamma(x) = \frac{1}{N^2}\left(-\frac{D(\bar{y})}{2\gamma\partial_y C|_{\bar{y}}}\left(\partial_y A|_{\bar{y}}\right)^2 + B(x,\bar{y})\right) \tag{2.27}$$

Based on the above, one can immediately calculate $P(x)$ the stationary probability distribution for species x, as [41]

$$P(x) = \frac{\mathcal{N}}{\Gamma(x)}\exp\left(2\int_0^x \frac{A(x',\bar{y})}{\Gamma(x')}\mathrm{d}x'\right) \tag{2.28}$$

Equations (2.23) and (2.28) constitute a theoretical approximation for the probability distributions of species x and y, as determined via the governing stochastic model. However, the above solution applies to a rather specific parameter settings: ω_{IE} is in fact set to zero to silence the retroaction of the activators on the inhibitors. The analysis will then be extended in the forthcoming section to the case where a small modulation ω_{IE} is allowed for.

In Figure 2.6 the numerically determined distributions are plotted: in both panels, (cyan) circles refer to the exact Master equation and (light purple) diamonds stand for a direct numerical integration of the Langevin equations (2.16). The parameters have been set as in Figure 2.5. The activated inhibitory concentration y admits therefore a unique fixed point, while two stationary stable equilibria are found for x. The distribution $P(y)$ (right panel of Figure 2.6) displays the expected bell shaped profile, the peak being located in $\bar{y}$. The solid line refers to the analytical solution (2.23) which

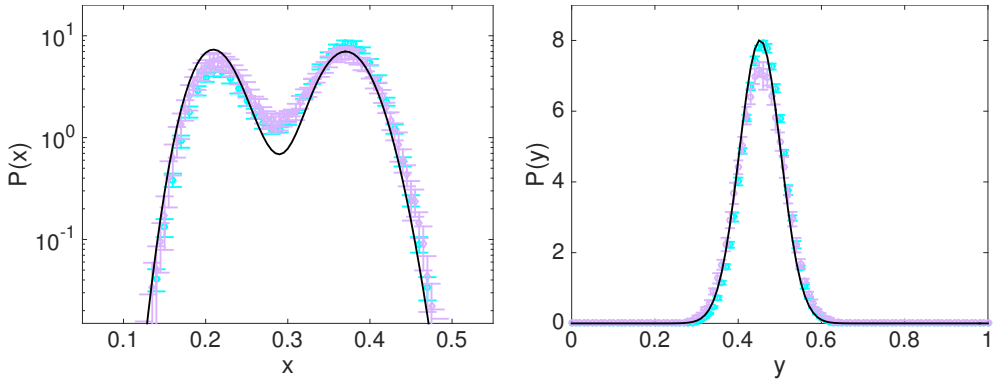

Figure 2.6: The distributions $P(x)$ (left panel) and $P(y)$ (right panel) are depicted. The (cyan) circles stand for the Gillespie stochastic simulation. The (light purple) diamonds refer to the numerical solution of the Langevin equations (2.13), via a straightforward implementation of the Euler-Maruyama scheme. In both cases the error bars are computed by averaging over 10 independent realizations. The solid lines are the theoretical predictions computed after equations (2.23) and (2.28).

.

appears to correctly interpolate the recorded numerical profiles. The distribution $P(x)$, as reported in the left panel of Figure 2.6: in this case, a bimodal profile is found, which reflects the simultaneous presence of two competing equilibria for the associated deterministic dynamics. The analytic profile traced after Equation (2.28) (solid line) agrees with the simulated data, at a satisfying degree of accuracy.

In Figure 2.7 the comparison between simulated and analytic $P(x)$ is drawn for different choices of the parameters β_E. The data reported in the upper panels of Figure 2.7 are obtained for a choice β_E that positions the system inside the region of x bistability. The correspondence between theory and simulations is again satisfying. The lower left plot refers instead to a choice of β_E that falls outside the region of bistability: in this case the deterministic

model predicts the presence of an isolated stable fixed point, characterized by a low level of activity. The distribution $P(x)$ extends however to large x, the small rightmost bump being a relic of the lost bistability. By modulating γ, one can eventually make the second bump more pronounced, seeding a noise induced bistability, which has no immediate counterpart in its corresponding deterministic framework.

2.5 Extending the analysis to the general setting: the case $\omega_{IE} \neq 0$.

The purpose of this section is to discuss a possible extension of the previous analysis. We assume a feedback of excitatory neurons on the population of inhibitors, that is, $\omega_{IE} \neq 0$. The approach that we shall present hereafter implements a perturbative iterative scheme, which implies dealing with a weak coupling, or stated differently, a sufficiently small value of ω_{IE}. The key idea is to treat the additional contribution stemming from ω_{IE} as a perturbation. As a first step, one needs to inspect the null unperturbed scenario which corresponds to setting $\omega_{IE} = 0$. One can follow step by step the approach outlined in the preceding section and eventually obtain a probability distribution function for x. We will hereafter denote the distribution obtained under this limiting condition, namely for $\omega_{IE} = 0$, by $P_0(x)$.

The stochastic dynamics of y is ruled by the following non-linear Langevin equation:

$$\dot{y} = \frac{1}{\gamma}\left(C(z,y) + \frac{1}{\sqrt{N}}\sqrt{D(z,y)}\eta_2\right) \tag{2.29}$$

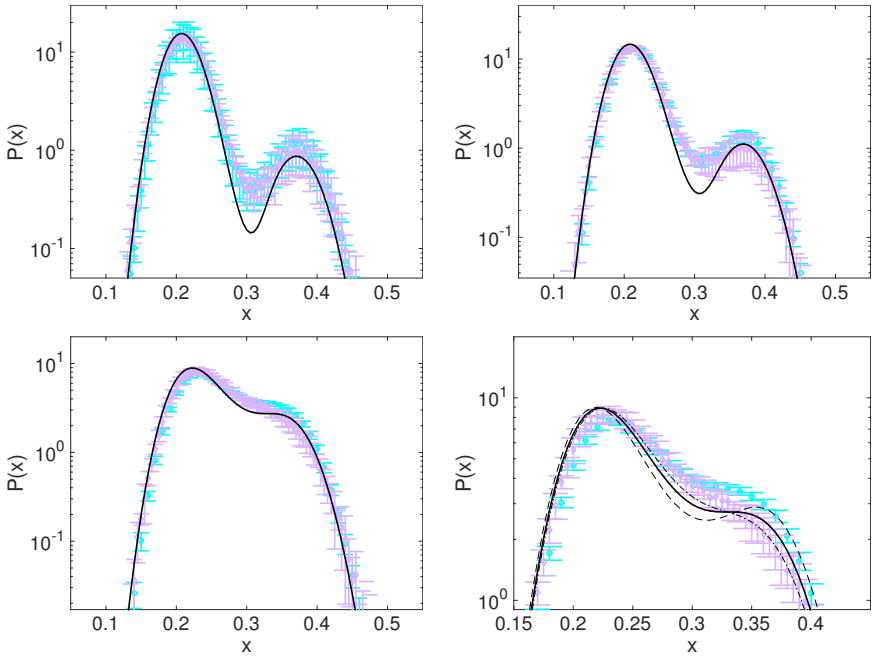

Figure 2.7: The distributions $P(x)$ is plotted for different choices of the gain parameter β_E. The two upper panels refer to $\beta_E = 4.5$ and $\beta_E = 3.7$. In both cases the system falls in the region of deterministic bistability. The lower panels refer instead to $\beta_E = 2$. In this case the deterministic bistability is lost, and the mean field dynamics for the species x predicts the existence of an isolated stationary stable fixed point. The other parameters are set as in Figure 2.2. Symbols stand for the simulations (see caption of Figure 2.4 for details on the selected graphic outline). The solid line stands for the theoretical prediction based on (2.28). Dot-dashed and dashed curves are traced according to (2.23) for, respectively, $\gamma = 1$ and $\gamma = 0.1$.

where:

$$\begin{aligned} C(z,y) &= -\alpha_I y + (1-y) f_I(s_I) \\ D(z,y) &= \alpha_I y + (1-y) f_I(s_I) \end{aligned} \tag{2.30}$$

and $s_I = z - \omega_{EI} y + h_I$ with $z = \omega_{IE} x << 1$. By exploiting the fact that ω_{IE} is small one can assume that a Taylor expansion is possible, we eventually obtain:

$$C(z,y) \simeq C(0,y) + R(x,y) + O(\omega_{IE}^2) \tag{2.31}$$

where $R(x,y) = \omega_{IE} x \frac{\partial s_I}{\partial z} \frac{\partial C}{\partial s_I} \mid_{0,y}$. Notice that $\frac{\partial s_I}{\partial z}$ is the gain parameter, identically equal to β_I for the family of non-linear function $f_I(\cdot)$ here considered (see caption of Figure 2.3). In equation (2.29) the function $D(z,y)$ is rescaled by $1/\sqrt{N}$, a small factor that encodes for the system size. For this reason, we set as a first approximation $D(z,y) \simeq D(0,y)$ and ignore all terms that combine ω_{IE} and $1/\sqrt{N}$. Summing up, for small ω_{IE}, the above equation (2.29) can be cast in the approximate form:

$$\dot{y} = \frac{1}{\gamma} \left(C(0,y) + R(x,y) + \frac{1}{\sqrt{N}} \sqrt{D(0,y)} \eta_2 \right) \tag{2.32}$$

Note that the deterministic term in equation (2.32) depends linearly on x, a non trivial modification which restores the bidirectional coupling with the homologous Langevin equation for species x. The assumed bistability on x reflects in fact on y, which also faces the simultaneous coexistence of two attracting equilibria. The linear noise approximation hence breaks down, as it is not possible to identify a unique fixed point of y that would act as pivotal point for the linear noise expansion to be carried out. On the other hand, for ω_{IE} sufficiently small, the two fixed points associated to y are evidently close.

It seems plausible to hypothesize that the two peaks of $P(y)$ would merge together, giving rise to a single bell shaped profile. Clearly, the endogenous noise should be large enough (hence the system size sufficiently small) for the coalescence of the peaks to take place. This is the scenario depicted in Figures 2.2 and 2.3 and which ultimately inspires the analysis to which the remaining part of this section is entirely devoted.

To proceed further we propose to replace the time dependent factor x appearing in equation (2.32) with $\bar{x}_0 = \int x P_0(x) dx$, a constant approximate quantity which follows the determination of the distribution function $P_0(x)$, as obtained in the limiting setting $\omega_{IE} = 0$. The fixed point $\bar{y}_1$ of equation (2.32) should fulfill the condition

$$C(0, \bar{y}_1) + R(\bar{x}_0, \bar{y}_1) = 0 \tag{2.33}$$

Here, a single fixed point is expected, the distribution $P(y)$ being, by assumption, unimodal. To characterize the fluctuations associated to the stochastic variable y, we perform a linearization of (2.32) around the fixed point $\bar{y}_1$. More explicitly we posit $y = \bar{y}_1 + u$, and carry out a Taylor expansion in u, the supposedly small stochastic perturbation. A mathematical operation yields the linear stochastic equation:

$$\dot{u} = Q(\bar{y}_1)u + \frac{1}{\gamma\sqrt{N}}\sqrt{D(0, \bar{y}_1)}\eta_2 \tag{2.34}$$

where $Q(\bar{y}_1) = \frac{\partial C}{\partial s_I} \mid_{0,\bar{y}_1} + \left(\frac{\partial^2 C}{\partial y \partial s_I}\right) \mid_{0,\bar{y}_1}$. Note that in the last term we have deliberately dropped the linear contribution in u. As remarked earlier, the

amplitude of the stochastic term is already scaled by $1/\sqrt{N}$, a small factor that senses the size of the system. We approximate u as a Gaussian δ-correlated noise of variance:

$$\sigma_1^2 = \left(\frac{-D(0, \bar{y}_1)}{2\gamma N C'} \frac{1}{1 + C''/C'} \right) \tag{2.35}$$

where $C' = \left(\frac{\partial C}{\partial s_I} \right) |_{0,\bar{y}_1}$ and $C'' = \left(\frac{\partial^2 C}{\partial y \partial s_I} \right) |_{0,\bar{y}_1}$. Summing up, at this order of approximation, the stochastic variables y follow a Gaussian distribution $P_1(y)$ of mean $\bar{y}_1$ and variance σ_1^2. With this we can proceed as illustrated in the preceding Section to eventually obtain an updated expression for the distribution of x, namely $P_1(x)$. The reasoning can be repeated further, by exploiting $P_1(x)$ to calculate a novel estimate $\bar{x}_2$, which would allow in turn to self-consistently calculate $P_2(x)$ and $P_2(y)$, the updated distribution of, respectively, x and y. In Figure 2.8 the distributions computed according to the above procedure are confronted to direct simulations assuming the parameters setting of Figures 2.2 and 2.3. The 0^{th} order of approximation corresponding to the limiting condition $\omega_{IE} = 0$ is depicted with a dashed line. The solid line refers to the prediction obtained after three successive iterations of the outlined procedure. The method converges quickly, and the improvements are already remarkable after the first round of iteration.

2.6 Observations and conclusions

Endogenous fluctuations arising from finite-size fluctuations can play a role of paramount importance in shaping the self-emerging macroscopic dynamics of

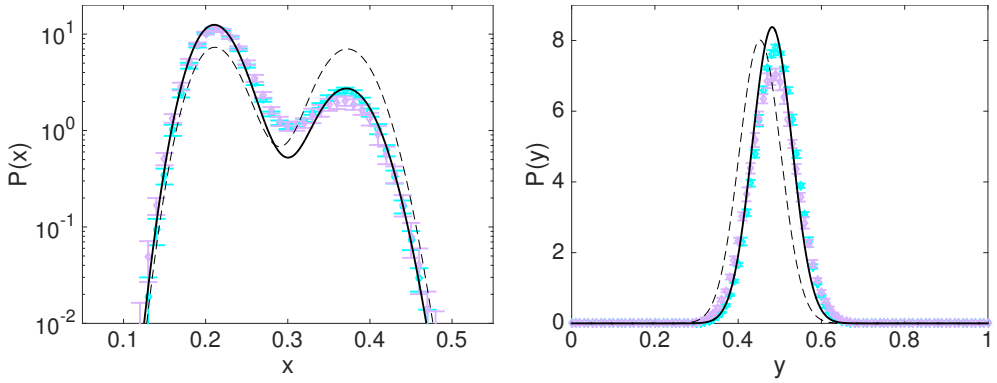

Figure 2.8: The distributions $P(x)$ (left panel) and $P(y)$ (right panel) are represented. The (cyan) circles refer to the stochastic Gillepsie based simulations. The (light purple) diamonds are obtained upon integration of the non-linear Langevin equations (2.13). The dashed lines represent the initial theoretical guess ($\omega_{IE} = 0$). The solid lines stand for the solution obtained after three consecutive iterations of the method described in the main body of the paper. In particular, $\omega_{IE} = 0.5$.

a multi-species model. Populations perturbations resulting from the inherent discreteness of the inspected medium can be rationalized by resorting to a linear noise treatment, which proves perfectly adequate when the underlying deterministic dynamics admits a trivial fixed point. In general, non-linearities are present and may eventually yield more complex dynamical behaviors, including multistability.

In this case, the linear noise machinery can be punctually employed to resolve the local dynamics of the system around each of the mutually competing equilibria. To quantify the statistics of rare events that materialize in the transitions from one attractor of the deterministic dynamics to another, and reconstruct the underlying stationary probability distributions, requires extending beyond the domain of application of the linear noise ap-

proximation. We have here considered a stochastic version of the Wilson Cowan (WC) model, which accommodates for a finite population of excitatory and inhibitory neurons. The model assumes a finite carrying capacity, the population census summing up to a constant. The relative ratio of inhibitory over excitatory neurons acts as a control parameter of the model. The master equation that rules the dynamics of the stochastic WC model is expanded in powers of the inverse population size: a diffusion approximation is consequently obtained, which consists in a coupled pair of non-linear Langevin equations, with multiplicative noise. These latter equations are solved numerically and shown to return a statistical description of the stochastic dynamics, which adheres quantitatively with that displayed by the exact Markov model.

Our analysis is specifically targeted to the region of bistability, a phenomenon that can a priori interest both the interacting families. To gain analytical insight into the investigated process we considered a simple scenario, assigning the parameters to have just one stationary stable equilibrium for the population of inhibitors. The excitatory neurons can instead undergo bistable behavior. There, we operate a substantial reduction in complexity since the equation ruling the dynamics for the inhibitors becomes one dimensional and therefore solvable. In particular, the dynamics of the excitatory species is ruled by an independent, non-linear Langevin equation: the indirect imprint of the inhibitors is reflected in a modified noise term, while the deterministic contribution is evaluated at the fixed point of species y. The population of inhibitors can be considered as an additional noise source. This latter contribution becomes the more pronounced the smaller the rel-

ative ratio of inhibitory versus excitatory neurons are broadening in turn the region where a bistable-like behavior is detected. Analytical expressions for the distributions of, respectively, excitatory and inhibitory neurons are obtained, which show a satisfying degree of agreement with the simulated data. The methods are subsequently generalized to the setting in which both populations display multiple fixed points. An iterative scheme is in fact devised that builds on the zeroth order approximation described above and allows us to explain the modifications displayed in the recorded probability distribution function when a modest feedback of the excitatory on inhibitory neurons is accommodated for. In conclusion, we have contributed to the understanding of the stochastic WC model, focusing on a dynamical regime for which the linear noise approximation is manifestly inadequate. The non-linear Langevin equations which represent the diffusion approximation limit of the original model can be characterized under suitable operating conditions, so contributing to shed light on the subtle dynamical interplay between distinct families of interacting neurons.

We also want to end this chapter by pointing out an interesting feature. Indeed, finite size noise and its inhibitory based component cause an extension of the region deputed to the excitatory bistability, as compared to deterministic predictions. This contributes, in turn, to elevate the degree of inherent exibility of the system and broaden its adaptiveness.

This work led to the following publication: *Diffusion approximation of the stochastic Wilson-Cowan model*, Zankoc C., Biancalani T., Fanelli D. and Livi R., Chaos, Solitons & Fractals **103** 504-512 (2017)

Chapter 3

Entangled stochastic motifs in networks

[1] In the second chapter, we have considered a stochastic version of the WC model accounting for the finiteness of the system. We decided to set our system parameters in a region where it displays bistability. Working in this setting, we introduced, and then applied, a selection of techniques for dealing with stochastic systems. These latter tools will be hereafter employed to shed light on a different problem: our system will no longer be a single, isolated unit but an assembly of identical nodes organized on a network.

Living systems execute an extraordinary plethora of complex functions that result from the intertwined interactions among key microscopic actors [44]. Positive and negative feedbacks appear to orchestrate the necessary degree of macroscopic coordination [45], by propagating information to distant sites while supporting the processing steps that underly categorization

[1] By motifs we mean a pattern or design.

and decision-making. Excitatory and inhibitory circuits play, in this respect, a role of paramount importance. As an example, networks of excitatory and inhibitory neurons constitute the primary computational units in the brain cortex [9, 10, 15]. They can flexibly adjust to different computational modalities, as triggered by distinct external stimuli [46, 47]. Genetic regulation is also relying on sophisticated inhibitory and excitatory loops [48, 49, 50, 51]. Specific genes are customarily assigned to the nodes of a given structure, which can be abstractly pictured as a complex network [52, 53, 54] .

In this chapter, we will to consider a network made of identical patches on which stochastic oscillations, termed in the literature *quasi-cycle*, take place. In fact, quasi-cycles are simply stable focus driven by noise. We want to understand whether and how stochastic oscillations from distant nodes can eventually synchronize. We will realize that inter-nodes correlation exist and persist even at large distances. Anti-phase synchrony at small frequencies is resolved on adjacent nodes and found to promote the spontaneous generation of coordinated pattern of actions, that invade the network as a whole. These patterns are absent under the idealized deterministic scenario, and could provide novel hints on how living systems implement and handle a large gallery of delicate computational tasks. They could indeed represent the basic architectural units for natural systems to perform efficient computations [55, 56, 57].

As a first step in the analysis we shall introduce the minimal stochastic model to be investigated. We will begin by discussing an isolated system and turn then to consider the coupled dynamics of a multispecies, excitatory and inhibitory model distributed on a network. The simple setting where just

two nodes are considered will serve as a basis to develop the main reference tools.

3.1 Reduced Wilson-Cowan model and quasi-cycles

3.1.1 Reduced WC model

Here again we denote by X and Y two individuals of, respectively, the excitatory and the inhibitory populations. We further label with V the volume of the patch (node) where the dynamics takes place. This time X and Y undergo the following reactions:

$$\begin{array}{rcl} \emptyset & \xrightarrow{f[s_x]} & X \\ X & \xrightarrow{1} & \emptyset \\ \emptyset & \xrightarrow{f[s_y]} & Y \\ Y & \xrightarrow{1} & \emptyset \end{array} \tag{3.1}$$

where $\emptyset$ denotes an infinite reservoir. This set of reactions is different from 2.1, as it describes the stochastic dynamics in the diluted limit. Here again f is a sigmoid function but this time the synaptic currents are

$$\begin{array}{rcl} s_x & = & -r\left(\frac{n_X}{V} - \frac{1}{2}\right) \\ s_y & = & r\left(y - \frac{n_Y}{V}\right) \end{array} \tag{3.2}$$

We notice that $r > 0$ is the only free parameter. Indeed, we have proceeded to a substantial reduction in the number of parameters (8 in the original

WC model), hence its name of *reduced Wilson-Cowan model.* n_X and n_Y respectively identify the numbers of elements of type X and Y. From the definition of $s_{x,y}$, and recalling the expression for $f(\cdot)$, it is immediately clear why X and Y are referred to as the excitatory and the inhibitory species. To obtain the deterministic dynamics of our system we can proceed following the same strategy as outlined in the Chapter 2, that is, writing down the master equation, expanding it in powers of the inverse of the volume V to get a Fokker-Planck that we convert into an equivalent set of Langevin equation and finally take the deterministic limit $V \to \infty$. To avoid redundancy, we will skip technicalities and simply write the equations we derived. In the limit where the volume V (hence the number of molecules) is large, one can describe the system in terms of the concentrations of the chemical species $x = \lim_{V\to\infty} \frac{<X>}{V}$ and $y = \lim_{V\to\infty} \frac{<Y>}{V}$, this leads to

$$\begin{aligned} \dot{x} &= -x + f\left(-r(y - \tfrac{1}{2})\right) \\ \dot{y} &= -y + f\left(r(x - \tfrac{1}{2})\right) \end{aligned} \tag{3.3}$$

where $f(s_{x,y}) = \frac{1}{1+\exp(-s_{x,y})}$ is a sigmoid function. The above system admits a single nontrivial fixed point (or steady state) $x_f = y_f = \frac{1}{2}$. Note that the refraction terms $(1 - x), (1 - y)$ in front of the sigmoid functions in both equations were dropped since we are in the high diluted limit. It is straightforward to characterize the stability of (x_f, y_f) by computing the eigenvalues λ of the Jacobian matrix $\mathbf{J}$ associated to system (3.3), evaluated at fixed point

$$\mathbf{J} = \begin{bmatrix} -1 & -r/4 \\ r/4 & -1 \end{bmatrix} \tag{3.4}$$

Performing the calculation one gets $\lambda = \lambda_{Re} + i\lambda_{Im} = -1 \pm i\sqrt{r}/4$. The real part of λ is negative and the fixed point is therefore stable. Furthermore, the eigenvalues are complex: sustained stochastic oscillations around the fixed point, also called *quasi-cycle*, can eventually set in.

3.1.2 Quasi-cycles

To understand what happens when we turn on stochastic corrections we are going to employ once again the small noise approximation [35]. More specifically, we proceed to the following change of variables

$$\begin{aligned} x(t) &= x_f + V^{-1/2}\xi_1 \\ y(t) &= y_f + V^{-1/2}\xi_2 \end{aligned} \tag{3.5}$$

where $\xi = (\xi_1, \xi_2)$ stands for the stochastic perturbation. The small noise limit assumes V to be large, so that only linear terms in ξ are to be retained when the above ansatz is inserted in the governing Master equation. The fluctuations can be shown to obey a set of linear Langevin equations [58] in the form

$$\dot{\xi}_i = \sum_j \boldsymbol{J}_{ij}\xi_j + \eta_i \tag{3.6}$$

where $\eta_i(t)$ is a Gaussian noise term with zero mean and with correlator $\langle \eta_i(t)\eta_j(t')\rangle = \delta_{ij}\delta(t-t')$, and $\mathbf{J}$ the Jacobian of the system given by (3.4).

To solve the above linear system we perform a Fourier transform. Denot-

ing the Fourier transform of the $\xi_i(t)$ as $\tilde{\xi}_i(\omega)$, one readily gets

$$\tilde{\xi}_i(\omega) = \sum_{j=1}^{2} \mathbf{\Phi}_{ij}^{-1}(\omega)\tilde{\eta}_j(\omega) \tag{3.7}$$

where $\mathbf{\Phi}_{ij} = -\boldsymbol{J}_{ij} - i\omega\boldsymbol{\delta}_{ij}$. One can hence calculate the power spectral density matrix (PSDM):

$$\boldsymbol{P}_{ij}(\omega) = < \tilde{\xi}_j(\omega)\tilde{\xi}_j^*(\omega) > = \sum_{l=1}^{2}\sum_{m=1}^{2} \mathbf{\Phi}_{il}^{-1}(\omega)\delta_{lm}\left(\mathbf{\Phi}^{\dagger}\right)_{mj}^{-1}(\omega) \tag{3.8}$$

The diagonal entries of the PSDM are real and coincide with the power spectra for the fluctuations, associated to each species. The (generally complex) off-diagonal elements of the PSDM can be properly normalized so to yield the Complex Coherence Function (CCF) or Coherency [59]

$$\boldsymbol{C}_{ij}(\omega) = \frac{\boldsymbol{P}_{ij}(\omega)}{\sqrt{\boldsymbol{P}_{ii}(\omega)\boldsymbol{P}_{jj}(\omega)}} \tag{3.9}$$

As explained in [60] the magnitude $|\boldsymbol{C}_{ij}|$ tells us the coherence between two signals, as a function of ω. The phase $\phi_{ij} = \arctan[(\boldsymbol{C}_{ij})_{Im}/(\boldsymbol{C}_{ij})_{Re}]$ quantifies the phase lag between the two inspected signals. In Figure 3.1 we depict the power spectra P_{11} and P_{22} (scale on the left), together with $|\boldsymbol{C}_{12}| = |\boldsymbol{C}_{21}|$ (scale on the right). The power spectra display an identical profile (due to the symmetry of the equations) which is peaked at $\omega \simeq \lambda_{Im}$: the endogenous fluctuations are amplified through a resonant mechanism that yields quasi-cycle oscillations. Symbols in the upper panel of Figure 3.1 refer to the numerically computed power spectra via the Gillespie scheme and con-

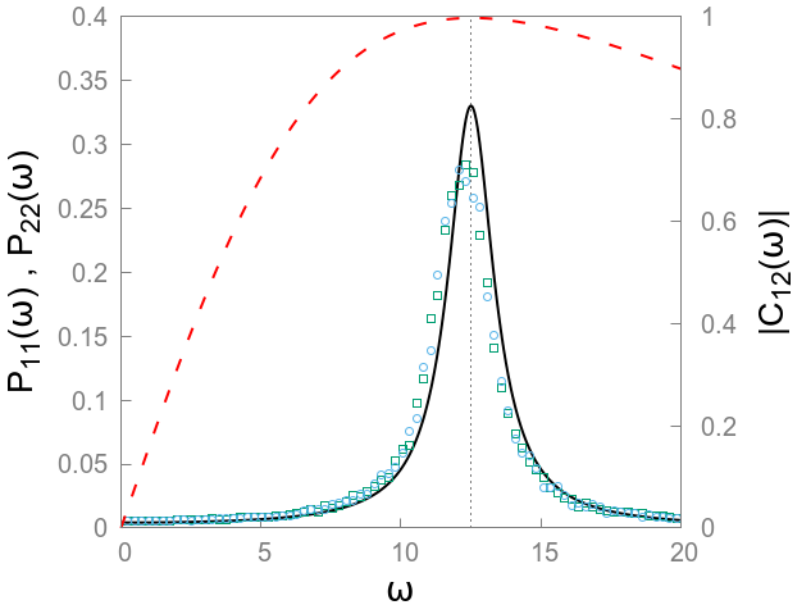

Figure 3.1: The theoretical power spectrum $\boldsymbol{P}_{11}(\omega) = \boldsymbol{P}_{22}(\omega)$ is depicted with a solid line. Symbols refer to the power spectra computed from averaging independent realization of the Gillespie dynamics. The squares refers to excitators (X), while the circles stand for inhibitors (Y). The vertical dotted line is traced at $\omega = \lambda_{Im} = \sqrt{r}/4$. The dashed line represents $|\boldsymbol{C}_{12}| = |\boldsymbol{C}_{21}|$. A phase lag equal to $\pi/2$ is predicted. Here $r = 50$ so to allow for the isolated peak in the power spectra to be distinctively revealed.

firm the adequacy of the linear noise calculation. The magnitude of $|C_{12}|$ is maximum, when the power spectra are. At this point the phase lag between the two oscillators, the excitators and the inhibitors, is $\pi/2$. In Figure 3.2 we plot the dynamics of both species, as obtained via the Gillespie scheme. The quasi-cycle oscillations around the mean-field equilibrium are evident, as well as the phase lag of about $\pi/2$ predicted by the LNA.

Starting from this, and building on the just introduced methodology, we shall proceed to study the issue of synchronization when two or more replica

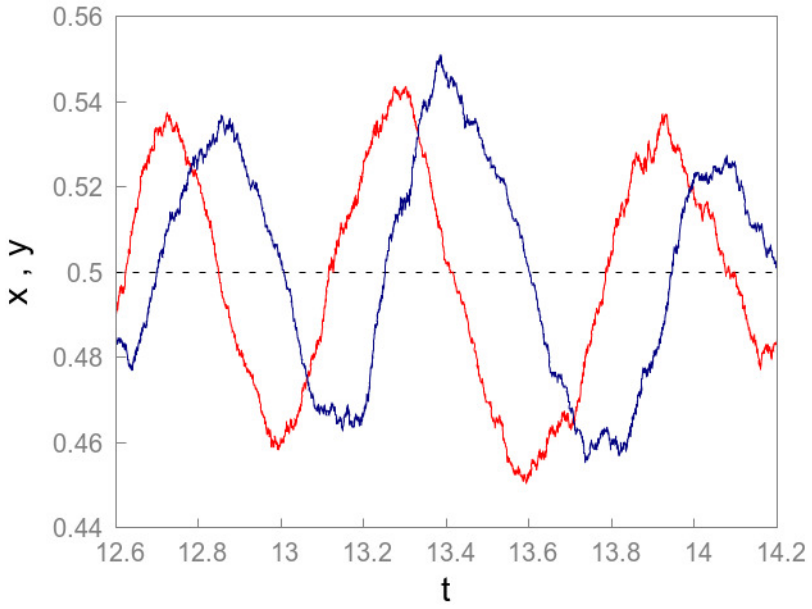

Figure 3.2: Stochastic trajectories ($\frac{n_x}{V}$ and $\frac{n_Y}{V}$ versus time). The fixed point of the underlying deterministic model is depicted with a dashed black line.

of model (3.1) are coupled together.

3.2 A two patches model of coupled excitatory-inhibitory dynamics

3.2.1 Deterministic dynamics and stability

We now turn to a more complex version of the above model. We begin by assuming a simple two patches (nodes) model. Symbols used to identify individual entities are now decorated with an additional index, so to specify the node to which they refer to. More concretely, we now deal with the elements X_i and Y_i, with $i = 1, 2$. Each element obeys the same birth and

death chemical equations given by (3.1). The only noticeable modification has to do with the definition of the synaptic currents $s_{(\cdot)}$. More specifically, and with an obvious meaning of the notation involved we have

$$\begin{aligned} s_{x_1} &= -r\left(\tfrac{n_{Y_1}}{V} - \tfrac{1}{2}\right) + D\Delta \\ s_{y_1} &= r\left(\tfrac{n_{X_1}}{V} - \tfrac{1}{2}\right) + D\Delta \\ s_{x_2} &= -r\left(\tfrac{n_{Y_2}}{V} - \tfrac{1}{2}\right) - D\Delta \\ s_{y_2} &= r\left(\tfrac{n_{X_2}}{V} - \tfrac{1}{2}\right) - D\Delta \end{aligned} \tag{3.10}$$

where $\Delta(n_{X_1}, n_{X_2}, n_{Y_1}, n_{Y_2}) = (\frac{n_{X_2}}{V} - \frac{n_{X_1}}{V}) - (\frac{n_{Y_2}}{V} - \frac{n_{Y_1}}{V})$ and D is the coupling parameter. The Δ term, now part of the synaptic currents, represents the diffusive interaction taking place between each node, while the first r.h.s. term stands for the inner dynamics between excitatory and inhibitory population within the same node. The dynamics of the system is still ruled by a master equation, where now $\boldsymbol{n} = (n_{X_1}, n_{Y_1}, n_{X_2}, n_{Y_2})$. In the limit $V \to \infty$, these quantities (normalized to V) converge to the mean field concentrations (x_1, y_1, x_2, y_2). The ODEs that govern the time evolution of the deterministic variables constitute the natural generalization of equations (3.3). They read

$$\begin{aligned} \dot{x_1} &= -x_1 + f\left(-r(y_1 - \tfrac{1}{2}) + D(x_2 - x_1) - D(y_2 - y_1)\right) \\ \dot{y_1} &= -y_1 + f\left(r(x_1 - \tfrac{1}{2}) + D(x_2 - x_1) - D(y_2 - y_1)\right) \\ \dot{x_2} &= -x_2 + f\left(-r(y_2 - \tfrac{1}{2}) + D(x_1 - x_2) - D(y_1 - y_2)\right) \\ \dot{y_2} &= -y_2 + f\left(r(x_2 - \tfrac{1}{2}) + D(x_1 - x_2) - D(y_1 - y_2)\right) \end{aligned} \tag{3.11}$$

The imposed coupling feels the gradient of concentrations, for both excitatory and inhibitory populations. One can realize that $x_1 = x_2 = x_f$ and $y_1 = y_2 = y_f$ is an equilibrium solution of the underlying deterministic model. To

assess the stability of the fixed point, we compute the eigenvalues of the 4×4 Jacobian matrix $\mathbf{J}$ given by

$$\mathbf{J} = \begin{bmatrix} -1 - D/4 & -(r-D)/4 & D/4 & -D/4 \\ (r-D)/4 & -1 + D/4 & D/4 & -D/4 \\ D/4 & -D/4 & -1 - D/4 & -(r-D)/4 \\ D/4 & -D/4 & (r-D)/4 & -1 + D/4 \end{bmatrix} \tag{3.12}$$

The Jacobian is a block matrix that may be partitioned by means of two distinct 2×2 matrix; one depending on both parameters r and D and standing along the diagonal, the other being in each corner and only dependent on parameter D. Two eigenvalues coincide with the ones calculated above for the isolated patch setting, $\lambda_{1,2} = -1 \pm i(r/4)$. The two additional eigenvalues read

$$\lambda_{3,4} = \pm\sqrt{\frac{r}{4}(D - \frac{r}{4})} - 1 \tag{3.13}$$

and depend on the coupling strength D [2]. For $D > D_c = r/4 + 4/r$, λ_3 is real and positive and the fixed point turns therefore unstable. For $D < D_c$, however the solution $x_1 = x_2 = x_f = 1/2$ and $y_1 = y_2 = y_f = 1/2$ is stable and the deterministic system displays a uniform level of activity, for both excitators and inhibitors, across the nodes. In other words, the system undergoes a pitchfork bifurcation at $D = D_c$ where two symmetric stable branches appear. This is illustrated in Figure 3.3.

To gain further insight into the dynamics of the system, we perform a linear expansion close to the bifurcation point, $D = D_c = r/4 + 4/r$. More specifically, we carry out a change of variables: $x_1 = x_f - \epsilon_x$, $y_1 = y_f - \epsilon_y$,

[2] Notice that for $D = 0$, $\lambda_{3,4}$ converges $\lambda_{1,2}$, as it should be

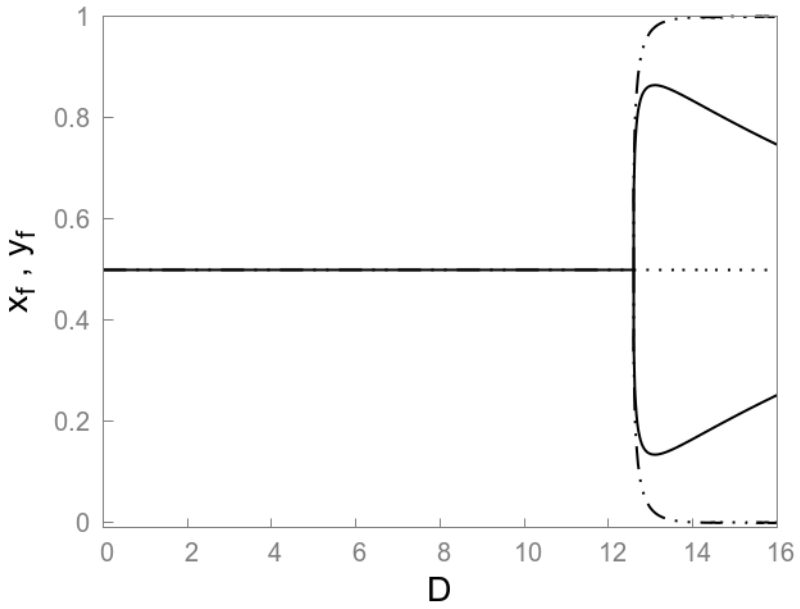

Figure 3.3: Diagram of bifurcation for a two nodes system. The solid black line refers to the fixed point for $x_{1,2}$ while the dashed-dotted refers to $y_{1,2}$. The dashed line refers to the unstable fixed points for both $x_{1,2}$ and $y_{1,2}$.

$x_2 = x_f + \epsilon_x$, $y_2 = y_f + \epsilon_y$. By inserting the above ansatz into the full non-linear equations (3.11) and performing a linear expansion in the perturbation parameters (ϵ_x, ϵ_y) eventually yields:

$$\epsilon_x = -\epsilon_y \frac{\frac{r}{8} - \frac{2}{r}}{1 + \frac{D_c}{2}}$$

a closed expression that allows to immediately appreciate the relative modulation of the fixed points above the instability threshold. In particular for $r > 4$, ϵ_x and ϵ_y have opposite signs. Imagine that the concentration of the excitators on node 1 displays a level of activity that is larger than 1/2. In other words x_1 belongs to the upper stable (solid) branch in Figure 3.3. Then,

x_2 is forcefully associated to the lower branch of the bifurcation diagram; y_1 and y_2 display in turn an opposite internal arrangement. In other words, above the bifurcation point, the deterministic system manifests a degree of spatial organization (across nodes) that, to some extent, preditcs the noise driven motifs for $D < D_c$ that we will discuss in the coming section.

3.2.2 Finite-size corrections

We consider now the full stochastic model and operate at finite V. The two nodes are formally decoupled when D is set to zero. Excitators (respectively inhibitors) on the first node will execute stable focus driven by noise oscillations about the trivial deterministic fixed point. Analogous considerations hold for the homologous quantities hosted on the second node. Stochastic trajectories referred to distinct nodes are however disentangled. Conversely, when $0 < D < D_c$ inter-nodes species are effectively coupled, the degree of reciprocal influence being more pronounced the closer D is to D_c. Can the imposed coupling enforce a synchronization of the emergent stochastic oscillations? This is the question that we are going to answer hereafter, building on the methodology we used to study the single node and computing the 4×4 PSDM associated to the system at hand

$$\boldsymbol{P}_{ij}(\omega) = \langle \tilde{\xi}_i(\omega) \tilde{\xi*}_j(\omega) \rangle \tag{3.14}$$

Since the two nodes share identical parameters, the PSDM can be completely characterized in terms of 6 different entries, namely $P_{11}(\omega) = P_{33}(\omega)$, $P_{22}(\omega) = P_{44}(\omega)$, $P_{12}(\omega) = P_{34}(\omega)$, $P_{13}(\omega) = P_{24}(\omega)$, $P_{14}(\omega) = P_{23}(\omega)$. Focus

first on the diagonal elements of the PSDM , i.e. the power spectra $P_{ii}(\omega)$, $i = 1, \ldots, 4$. The results of the analysis are plotted in the left panel of Figure 3.4, for $i = 1$. When $D = 0$, the power spectrum displays an isolated peak, located at $\omega \simeq r/4$ (rightmost vertical dashed line) in agreement with the analysis carried out for the single patch case study. When D increases, a second peak develops and progressively gains in magnitude. Its position is well captured by the (positive) imaginary component of the eigenvalues $\lambda_{3,4}$ (dashed lines). When D approaches the critical threshold D_c, the leftmost peak stands alone, and the other fades away. For intermediate parameter settings, the stochastic oscillators are forged by the simultaneous presence of two leading frequencies, whose relative importance can be controlled as wished. Gillespie bases simulations, performed for different values of D, shows good agreement with the theory. Similar observations apply to $i = 2, 3, 4$.

Consider now the off-diagonal entries of the PSDM and build the corresponding CCF. To shed light onto the inter-nodes correlation between excitators, we plot in the right panel of Figure (3.4) $|C_{13}|$, in the plane (ω, D), using an apt color code. For small D, the signals are, as expected, completely independent. By increasing D, two regions are found where $|C_{13}|$ takes values close to unit. Quasi-cycles displayed by the excitatory populations attached to distinct nodes do synchronize, for sufficiently large values of the coupling strength. Intriguingly enough, and at odds with the examples so far reported in the literature, the synchronization is established for two different characteristic frequencies. These are the indirect reflex of the two peaks identified in the power spectrum. Even more importantly, the two aforementioned regions are separated by a distinct frontier (white dashed line) where $|C_{13}|$ is found

to be identically equal to zero: in the left portion of the plan, with respect to the white dashed separatrix, the phase lag is *exactly* π. The stochastic trajectories are hence predicted to be in anti-phase, on short frequencies, or equivalently, long periods. In the complementary portion of the plane, i.e. on the right of the separatrix, ϕ is found to be zero, thus implying in phase synchrony at large frequencies or short periods. Direct simulations confirm the scenario depicted above; see trajectories annexed to the right panel of Figure (3.4). Stochastic trajectories referred to the same species attached to contiguous nodes are *entangled*. The result of a measurement at one node roughly determines the outcome of a measurement simultaneously performed at the other node. Leaving aside more fundamental reflections, we remark that such entangled states can be hierarchically assembled to yield macroscopic patterns, as we shall demonstrate herafter.

Complementary information can be drawn by inspecting the other off-diagonal elements of the PSDM. We know that, when $D = 0$, excitators and inhibitors belonging to the same node oscillate with a phase of $\frac{\pi}{2}$. This condition is perpetrated when D is made to increase inside the region of interest ($D < D_c$), with however the emergence of a frequency of anti phase synchrony. This can be observed on the left panel of Figure 3.5 where $|C_{12}|$, which quantifies the amount of synchrony between inhibitory and excitatory in the same node, is reported in the reference plane (D, ω). One can distinguish a new branch on which $|C_{12}|$ takes significant value. This new branch progessively converges towards low frequencies as D increases. The phase lag associated to this frequency of synchronization is progressively modulated and eventually approaches π, for large enough coupling. Also in this

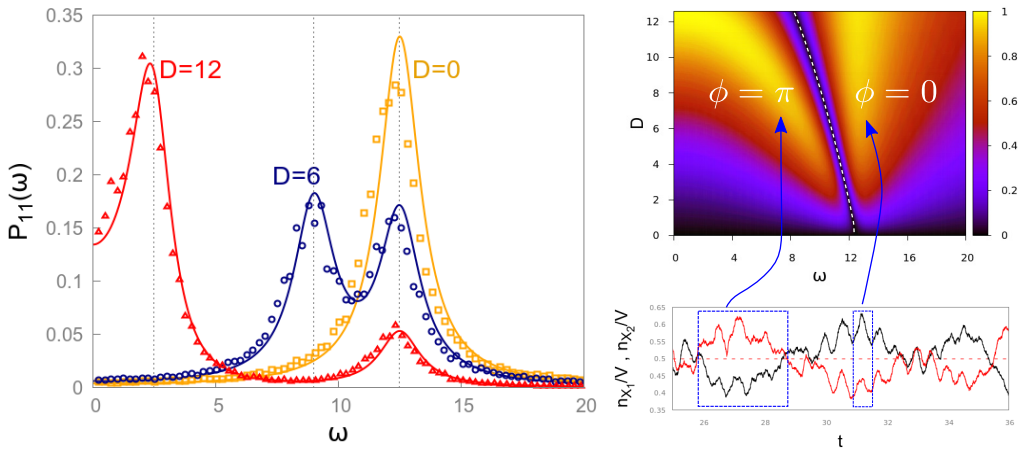

Figure 3.4: Left panel: the power spectrum P_{11} is plotted as function of ω, for different choices of D. Lines refer to the theoretical predictions. Symbols are obtained by averaging over many realizations of the stochastic simulations. Right panel: $|C_{13}|$ is plotted in the plane (ω, D). Two regions can be identified where the synchronization take place. These are separated by the dashed (white) line, obtained by setting $|C_{13}| = 0$. The synchronization at small frequencies occur in anti-phase ($\phi = \pi$), while at high frequencies the theory predicts $\phi = 0$. The stochastic trajectories (n_{X_1} and n_{X_3} vs. time t) confirm the adequacy of the LNA. In phase and anti-phase regimes of synchronization are highlighted in the boxes. Here, $r = 50$ and $V = 20000$.

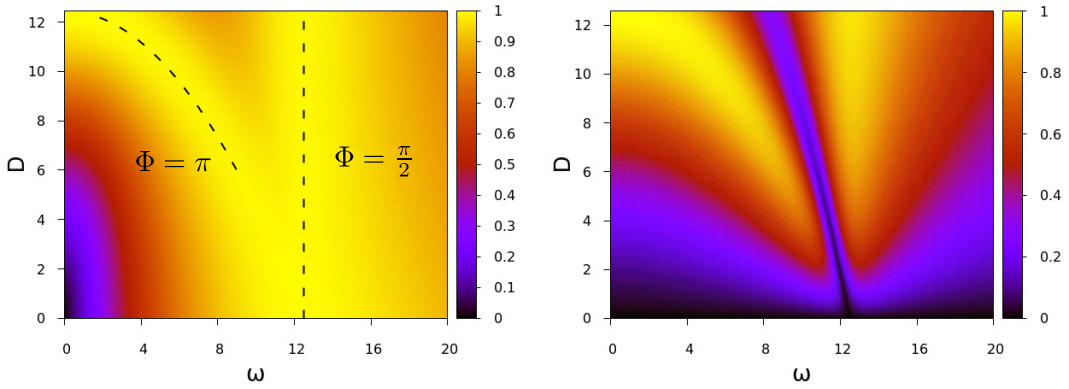

Figure 3.5: Left panel: map describing the magnitude of C_{12} in the reference plane (D, ω). This parameter allows to resolve the degree of synchronization between excitators and inhibitors in the same node. Right panel: $|C_{14}|$ is plotted in the plane (D, ω).

case, numerical experiments are found in excellent agreement with the theory predictions. Similar conclusions can be drawn by analyzing C_{24} and C_{34}. In the right panel of Figure 3.5 the magnitude of $|C_{14}|$ in plotted in the plane (D, ω).

3.3 Excitatory-inhibitory interactions on a complex network

3.4 Mean-field approximation

We are now in a position to extend the analysis to the relevant case where the interactions between excitators and inhibitors is mediated by a complex network. As outlined for the two nodes setting, the interactions is supposed

to be diffusive in that it senses the difference of concentrations between homologous species on distinct nodes. Furthermore, the coupling is embedded in the non-linear function $f(\cdot)$, here introduced to exemplify the activation process. Consider now an extended collection of Ω nodes and label with $\mathbf{A}$ the associated adjacency matrix: $A_{ij} = 1$ if nodes i and j are connected, $A_{ij} = 0$ otherwise.

In the following we will consider symmetric coupling $A_{ij} = A_{ji}$, in line with the above treatment. We however anticipate that our conclusions remain unchanged, when asymmetric couplings are accommodated for. The state of the system is photographed by the 2Ω components vector $\boldsymbol{n} = (n_{X_1}, n_{Y_1}, n_{X_2}, n_{Y_2}, \ldots, n_{X_\omega}, n_{Y_\Omega},)$. Correspondingly, in the limit $V \to \infty$, we deal with the mean field concentrations $\mathbf{z} = (x_1, y_1, x_2, y_2, \ldots, x_\Omega, y_\Omega)$. Generalizing the expression introduced above for the case of two nodes, we set

$$\begin{aligned} s_{x_i} &= -r\left(\tfrac{n_{y_i}}{V} - \tfrac{1}{2}\right) + D\sum_j^\Omega \Delta_{ij}\tfrac{n_{x_j}}{V} - D\sum_j^\Omega \Delta_{ij}\tfrac{n_{y_j}}{V} \\ s_{y_i} &= r\left(\tfrac{n_{x_i}}{V} - \tfrac{1}{2}\right) + D\sum_j^\Omega \Delta_{ij}\tfrac{n_{x_j}}{V} - D\sum_j^\Omega \Delta_{ij}\tfrac{n_{y_j}}{V} \end{aligned} \tag{3.15}$$

where this time $\Delta_{ij} = A_{ij} - \kappa_i\delta_{ij}$ is the standard discrete Laplacian operator and κ_i stands for the connectivity of node i. The deterministic equations read

$$\begin{aligned} \dot{x}_i &= -x_i + f\left(-r\left(y_i - \tfrac{1}{2}\right) + D\sum_j^\Omega \Delta_{ij}x_j - D\sum_j^\Omega \Delta_{ij}y_j\right) \\ \dot{y}_i &= -y_i + f\left(r\left(x_i - \tfrac{1}{2}\right) + D\sum_j^\Omega \Delta_{ij}x_j - D\sum_j^\Omega \Delta_{ij}y_j\right) \end{aligned} \tag{3.16}$$

3.4.1 Stability

We first want to determine a closed analytical expression for the critical value of the coupling constant D that sets the limit of stability of the homogeneous

fixed point. To do so, we start by inserting $x_i = x_f + \delta x_i$ and $y_i = y_f + \delta y_i$ in the above equations and linearize them by retaining the terms of the first order only in the imposed perturbation $(\delta x_i, \delta y_i)$. A straightforward calculation leads to

$$\begin{array}{rcl} \dot{\delta x_i} & = & -\delta x_i + \left(-r\delta y_i + D\sum_j^\Omega \Delta_{ij}\delta x_j - D\sum_j^\Omega \Delta_{ij}\delta y_j\right) f'(\mathbf{z_f}) \\ \dot{\delta y_i} & = & -\delta y_i + \left(r\delta x_i + D\sum_j^\Omega \Delta_{ij}\delta x_j - D\sum_j^\Omega \Delta_{ij}\delta y_j\right) f'(\mathbf{z_f}) \end{array} \tag{3.17}$$

where f' denotes the derivative of the sigmoid function f and $\mathbf{z_f}$ the homogenous fixed point vector. It is immediate to realize that $f'(\mathbf{z_f}) = f(\mathbf{z_f})(1 - f(\mathbf{z_f})) = 1/4$. We then set to expand the perturbations $(\delta x_i, \delta y_i)$ on the basis of the eigenvectors of the Laplacian Δ. To this end, we denote by $\Gamma^{(\alpha)}$ (with $\alpha = 1 \dots \Omega$) the eigenvalues of the Laplacian and by $\phi_i^{(\alpha)}$ the associated eigenvectors, namely

$$\sum_j \Delta_{ij}\phi_j^{(\alpha)} = \Gamma^{(\alpha)}\phi_i(\alpha) \tag{3.18}$$

In formulae, we require:

$$\begin{array}{rcl} \delta x_i & = & \sum_\alpha^\Omega c_\alpha exp(\lambda_\alpha)\Phi_i^{(\alpha)} \\ \delta y_i & = & \sum_\alpha^\Omega b_\alpha exp(\lambda_\alpha)\Phi_i^{(\alpha)} \end{array} \tag{3.19}$$

Inserting in the equations for the perturbation, carrying out the calculation and projecting on each independent eigendirection, one eventually ends up with

$$\left[\begin{array}{cc} -1 + \frac{D\Gamma^{(\alpha)}}{4} - \lambda_\alpha & -\frac{1}{4}(r + D\Gamma^{(\alpha)}) \\ \frac{1}{4}(r + D\Gamma^{(\alpha)}) & -1 - \frac{D\Gamma^{(\alpha)}}{4} - \lambda_\alpha \end{array}\right] \left[\begin{array}{c} c_\alpha \\ b_\alpha \end{array}\right] = 0 \tag{3.20}$$

The above homogeneous system admits a non trivial solution provided the matrix in square brackets has zero determinant. This latter condition yields a second order equation for λ_α as function of $\Gamma^{(\alpha)}$ and D. Consider then λ_α^+, the largest of the two roots. If the real part of λ_α^+ is positive, then the perturbation grows exponentially and the homogeneous fixed point is unstable. In our analysis we considered symmetric networks: in this case the eigenvalues $\Gamma^{(\alpha)}$ are real and semi-negative defined. After a straightforward manipulation it is immediate to conclude that $(\lambda_\alpha^+)_{Re} < 0$ provided D is smaller than the critical value:

$$D_c = \frac{\frac{16}{r} + r}{2 \max_\alpha |\Gamma^{(\alpha)}|} \tag{3.21}$$

This latter expression has been successfully validated against numerical inspection. For $D < D_c$ the homogeneous fixed point is stable.

3.4.2 Intertangled stochastic motifs

Turning on the stochasticity of our system, we will show that intertangled stochastic patterns will take place. As a first example we consider a linear ring made of $\Omega = 4$ nodes and calculate the $2\Omega \times 2\Omega$ elements of the PSDM. In left panel of Figure 3.6 we show $|C_{1,2i+1}|$, with $i = 1, 2, 3$ (plotted on the horizontal axis), for a choice $D < D_c$, and against ω (plotted on the vertical axis). The phase lag, as predicted by the theory, is also displayed in the Figure 3.6 the values reported exactly apply inside the boxes delimited by the (white) dashed lines. A sequential alternation of phase and anti-phase synchronization is hence expected for the stochastic excitatory signals,

registered across the ring. Similar conclusions are drawn when considering $|C_{1,2i}|$, for $i = 1, 2, 3$, i.e. the degree of synchronization between excitators and inhibitors on different nodes. Patterns of activation instigated by the noise assisted drive towards self-organization are hence expected to emerge. Stochastic simulations, as reported on the left panel of figure 3.7, confirm the correctness of this conclusion: nodes are termporarily active or inactive, depending on their position along the chain. The emerging pattern is dynamical and the system switches continuously one given configuration and its negative analogue, as time progresses.

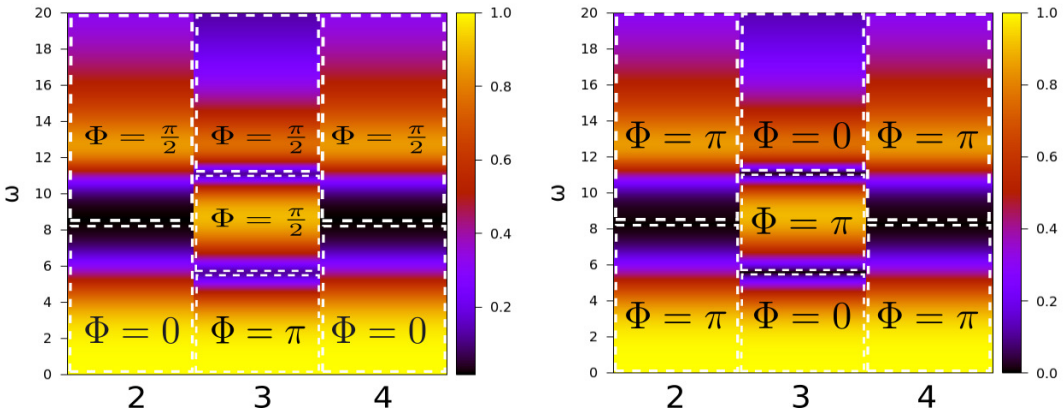

Figure 3.6: Left panel: $|C_{1,2i+1}|$ vs. ω (vertical axis) is plotted, for $i = 1, 2, 3$ (horizontal axis). The system is made up of 4 nodes organized in a closed linear ring. The synchronization occurs for roughly two values of ω, the modulus of the complex coherence function being more significant at low frequencies. The phase lag predicted by the theory is also displayed in the Figure. The values reported apply inside the regions delimi ted by the (white) dashed lines Right panel: same for $|C_{1,2i}|$

Excitators (upper circle, continuous arrow) and inhibitors (lower circle, dashed arrow) are in anti-phase on the node they happen to share: arrows point upward (resp. downward) if the measured activity is more (resp. less)

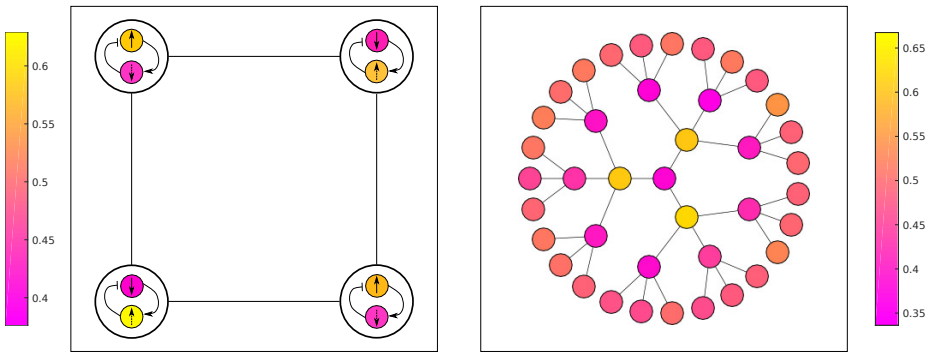

Figure 3.7: Snapshot of the stochastic dynamics for two networks topologies: the stochastic density of the excitators is plotted. Left panel: a chain of four nodes is considered - in each node the density displayed by excitators (upper circles) and inhibitors (lower circles) is depicted. Right panel: a snapshot of the stochastic pattern of activation of the excitators is shown.

pronounced as compared to the mean field uniform equilibrium. The architecture of the network plays indeed a crucial role. Robust patterns which exploit the phase/anti-phase dichotomy on a closed ring, necessarily require accommodating for an even number of nodes. When nodes are odd, frustration may occur. Recall that the formalism here developed apply to generic networks, not just to regular lattices. For demonstrative purposes, we show in the right panel of Figure 3.4 a snapshot of the (excitatory) activation pattern obtained when the system is placed on a tree with branching ratio equal to 4.

3.5 Conclusion

In a first place, we have shown that endogenous fluctuations can seed the emergence of regular oscillations when parameters are set so to drive deter-

ministic convergence towards a trivial equilibrium. Under the linear noise approximation (LNA), we were able to perform a Fourier analysis of our system first constitued by a single node. This allowed us to derive the power spectra associated to the stochastic signals for excitatory and inhibitory species and also to quantify their coherence and their phase shift by means of the Complex Coherence Function (CCF). We then considered a very simple network made of two identical nodes coupled diffusively. Adapting the tools we first employed on a single node, we found out that for intermediate parameter settings, the stochastic oscillators are forged by the simultaneous presence of two leading frequency, whose relative importance can be controlled by modulating the coupling. More interesting, stochastic trajectories of similar species from adjacent nodes are predicted to be in anti-phase on short frequencies and perfectly synchronized at large frequencies. Finally, we generalized our analysis to a complex network: proving that endogenous noise can promote a coordinated pattern, in a minimalistic model of excitatory and inhibitory interactions. This latter result encompasses, for its inherent simplicity, a large gallery of life science applications, ranging from neuroscience to the study of genetic circuits. Noise sustained intertangled motifs could indeed convey important tips on how living systems handle computational tasks and information processing.

This work led to the following publication: *Intertangled stochastic motifs in networks of excitatory-inhibitory units*, Zankoc C., Fanelli D., Ginelli F., and Livi R., Phys. Rev. E **96**, 022308 (2017)

Chapter 4

Noise driven neuromorphic tuned amplifier

In this chapter, the same reduced WC model is evolved on a directed lattice. We will show that such system behaves as a fully tunable amplifier: the endogenous component of noise, stemming from finite size effects, seeds a coherent (exponential) amplification without distorsion across the chain generating giant oscillations with tunable frequencies, a process that the brain could exploit to enhance, and eventually encode, different signals. On a wider perspective, the characterized amplification process could provide a reliable pacemaking mechanism for biological systems. We conclude this chapter by investigating the thermodynamics of our system, finding that the system extracts energy from the an external thermal bath and operates as an out of equilibrium thermal machine, under stationary conditions.

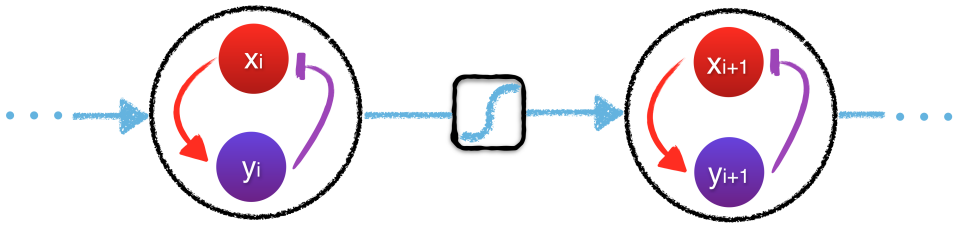

Figure 4.1: Schematic layout of the neuromorphic circuit.

4.1 The model

We continue working with the reduced WC model, with the only difference that now the patches are organized in a one dimensional lattice, as depicted in Figure 4.1, with unidirectional coupling. Consequently the synaptic currents read

$$\begin{aligned} s_{x_i} &= r\left(y_i - \tfrac{1}{2}\right) + D\left(x_{i-1} - x_i\right) - D\left(y_{i-1} - y_i\right) \\ s_{y_i} &= r\left(x_i - \tfrac{1}{2}\right) + D\left(x_{i-1} - x_i\right) - D\left(y_{i-1} - y_i\right) \end{aligned} \tag{4.1}$$

To provide additional degrees of freedom we assign to the patches a specific volume V_i. The governing Langevin equations take therefore the form

$$\begin{aligned} \tfrac{d}{d\tau}x_i &= \tfrac{1}{\gamma_i}\left[f(s_{x_i}) - x_i\right] + \tfrac{1}{\gamma_i\sqrt{V_1}}\sqrt{x_i + f(s_{x_i})}\lambda_i^{(1)} \\ \tfrac{d}{d\tau}y_i &= \tfrac{1}{\gamma_i}\left[f(s_{y_i}) - y_i\right] + \tfrac{1}{\gamma_i\sqrt{V_1}}\sqrt{y_i + f(s_{y_i})}\lambda_i^{(2)} \end{aligned} \tag{4.2}$$

where $\boldsymbol{\lambda} = (\lambda_1^{(1)}, \lambda_1^{(2)}, \ldots, \lambda_\Omega^{(1)}, \lambda_\Omega^{(2)})$ is a Gaussian stochastic variable with zero mean and correlator $\langle \lambda_i^{(l)} \lambda_j^{(m)} \rangle = \delta_{ij}\delta_{lm}\delta(\tau - \tau')$. Here γ_i stands for the ratio between the volume V_i of node i and the volume V_1 of node 1, $\gamma_i = \frac{V_i}{V_1}$, whereas, in the second chapter, γ was standing for the ratio between the total number of inhibitory neurons M and the total number N of excitatory neurons within the same node. As usual, we start by studying the system in its

thermodynamic limit $V_1 \to \infty$ to assess its stability. The inherent simplicity of our model which comes from the unidirectionality of the coupling makes very simple the computation of the eigenvalues of the Jacobian. Indeed, the Jacobian of the system evaluated at its homogenous fixed point, $x_f^i = y_f^i = \frac{1}{2}$ for all $1 \leq i \leq \Omega$, is a block tridiagonal matrix

$$\boldsymbol{J} = \begin{pmatrix} \boldsymbol{E}_1 & 0 & 0 & 0 & 0 \\ \boldsymbol{S}_2 & \boldsymbol{E}_2 & 0 & 0 & 0 \\ 0 & \boldsymbol{S}_3 & \boldsymbol{E}_3 & 0 & 0 \\ 0 & 0 & \ddots & \ddots & 0 \\ 0 & 0 & 0 & \boldsymbol{S}_\Omega & \boldsymbol{E}_\Omega \end{pmatrix} \tag{4.3}$$

where

$$\boldsymbol{E}_1 = \begin{pmatrix} -1 & -\frac{r}{4} \\ \frac{r}{4} & -1 \end{pmatrix}, \boldsymbol{E}_i = \begin{pmatrix} -\frac{1+D/4}{\gamma_i} & -\frac{r-D}{4\gamma_i} \\ \frac{r-D}{4\gamma_i} & -\frac{1-D/4}{\gamma_i} \end{pmatrix}, \boldsymbol{S}_i = \frac{D}{4\sqrt{\gamma_i \gamma_{i-1}}} \begin{pmatrix} 1 & -1 \\ 1 & -1 \end{pmatrix} \tag{4.4}$$

The characteristic polynomial of $\boldsymbol{J}$ writes

$$0 = det(\boldsymbol{J} - \lambda \boldsymbol{I}) = det(\boldsymbol{E}_1 - \lambda \boldsymbol{I}) \prod_{i=2}^{\Omega} det(\boldsymbol{E}_i - \lambda \boldsymbol{I}) \tag{4.5}$$

The first term in the preceding expression gives a quadratic equation for λ,

$$(\lambda + 1)^2 + \frac{r^2}{16} = 0 \tag{4.6}$$

This latter yields $\lambda_{1,2} = -1 \pm i\frac{r}{4} \equiv -1 \pm i\omega_0$. The remaining eigenvalues are

obtained by solving the following Ω equations:

$$\left(\frac{1+D/4}{\gamma_i}+\lambda\right)\left(\frac{1-D/4}{\gamma_i}+\lambda\right)+\frac{(r-D)^2}{16\gamma_i^2}=0 \tag{4.7}$$

allowing one to immediately obtain:

$$(\lambda_i)_{3,4}=\frac{1}{\gamma_i}\left[-1\pm\sqrt{-\frac{r}{8}\left(\frac{r}{2}-D\right)}\right] \tag{4.8}$$

We begin by assuming nodes of identical capacity $V_i = V$, which entails $\gamma_i = 1$. The spectrum of $\boldsymbol{J}$ is hence degenerate with eigenvalues $\lambda_{1,2}$ with mulitiplicity 1 and $(\lambda_i)_{3,4}$ with mulitiplicity $\Omega-1$. As expected, $\lambda_{3,4}$ converge to $\lambda_{1,2}$, when $D \to 0$. Based on equation 4.8, we can immediately conclude that the homogeneous fixed point is linearly stable provided $D < D_c \equiv \frac{r}{2}+\frac{8}{r}$. Importantly, the eigenvalues are complex for $D < r/2 < D_c$, an observation that plays a crucial role because, in the finite volume limit, this will give birth to the so-called quasi-cycles we presented in the previous chapter.

The technique employed in the previous chapter to assess the stability of the homogeneous fixed point, based on the expansion of the perturbations into the eigenbasis of the Laplacian, achieves the same result for D_c. We decided to opt for this method for one main reason. If we had used equation (3.21), we would have not obtained any information on the imaginary part of the Jacobian eigenvalues. However, it is of paramount importance to know about the imaginary part, since it gives the frequency of the modulation and allows to derive the condition for the emergence of quasi-cycles $D < r/2$.

4.2 Amplification and modulation mechanism

We now specialize on the stochastic, finite size dynamics, and hence assume V_1 to be finite. When $D = 0$ the stochastic trajectories on each node are formally disentangled. Excitators (reps. inhibitors) execute quasi-cycles. The amplitude of the oscillations scales as $1/\sqrt{V_1}$ and the associated frequency approximately reads $\omega_0 = r/4$, the imaginary part of the Jacobian eigenvalues in the uncoupled, $D = 0$, setting. A remarkably different scenario is faced when turning the coupling active. We will in particular operate for $D < r/2$, the homogeneous fixed point being therefore stable. The degenerate component of the Jacobian spectrum returns an additional frequency $\omega_1 = \sqrt{\frac{r}{8}\left(\frac{r}{2} - D\right)}$ which can be continuously modulated, in the range $[0, \omega_0]$, as function of D. This observation is central to understand the emerging stochastic dynamics: the internal noise seeds in fact giant quasi-cycles, with tunable frequency and growing amplitude across the lattice. The system spontaneously behaves as an effective, stochastic driven pacemaker.

4.2.1 Spectral analysis

The first thing we should do to investigate this problem is to compute the power spectrum $\boldsymbol{P}_{ii}(\omega) = \langle \tilde{\zeta}_i(\omega)\tilde{\zeta}_i^*(\omega)\rangle$ of fluctuations on node i. In Figure 4.2 the (normalized) power spectrum of excitators fluctuations on different nodes is plotted. Symbols refer to the numerical integration of equations (4.2) [42], while the solid lines follows the theoretical estimate (3.14). The power spectrum on the first node (circles, black online) is centered in ω_0 (rightmost vertical dashed line). The power spectrum on the second node

(squares, red online) displays a bimodal profile. A second peak emerges in correspondence of ω_1, leftmost vertical dashed line. Moving along the chain (pluses and diamonds), the bump in ω_0 fades away, while the peak in ω_1 becomes higher and gets progressively more localized. Individual trajectories as obtained on different nodes are superposed in Figure 4.3: the amplification can be clearly appreciated by eye inspection. Under the linear noise approximation, the maximum of the power spectrum diverges exponentially (not shown) along the chain. At the same time the width of the bell in ω_1 becomes narrower and the profile converges asymptotically to a delta like distribution. Beatings and other spurious modulations are therefore progressively filtered, as moving along the chain and building on the idealized linear approach: the system is hence predicted to eventually behave as a veritable pacemaker. However, non-linear terms do matter and eventually balance the growth, as predicted within linear scenario. Indeed, the process of amplification is expected to come to an halt when the oscillations get large enough so as to feel the boundary at $x_i \simeq 0$ (resp. $y_i \simeq 0$).

4.2.2 Characterization of the amplification mechanism

In this section, we denote by ζ the fluctuations around the fixed point. To shed light on to this mechanism and quantify the amplification grade under the linear noise approximation, we consider the distribution of fluctuations $\Pi(\boldsymbol{\zeta}, t)$ around the deterministic equilibrium. As it is shown in Appendix C, $\Pi(\boldsymbol{\zeta}, t)$ obeys to a Fokker-Planck equation which can be derived via LNA. The solution of the Fokker-Planck equation is a multivariate Gaussian that we can univocally characterize in terms of the associated first and second

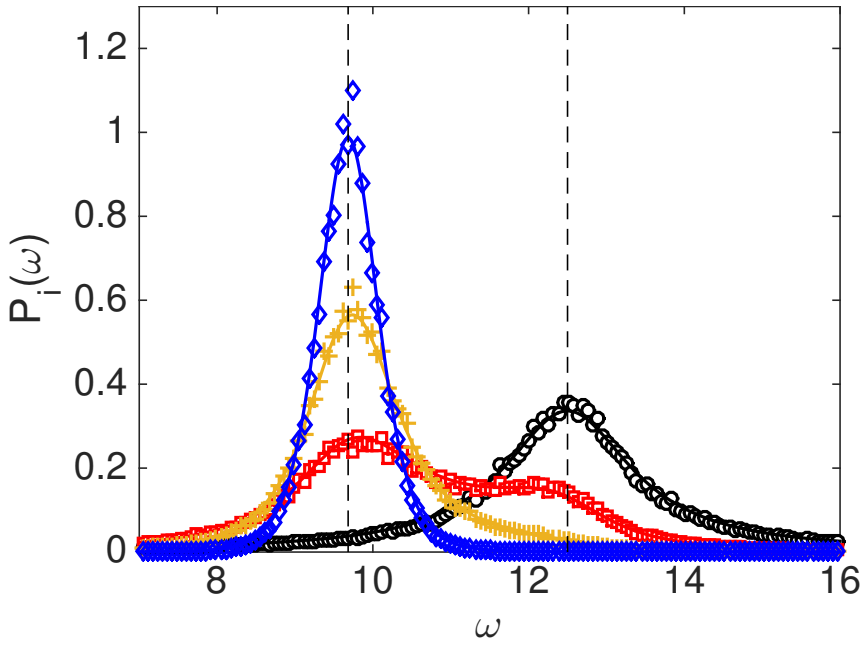

Figure 4.2: The theoretical power spectrum $P_i(\omega)$ for excitators (X), for $i = 1, .., 4$ is plotted with a solid line. Symbols refer to the power spectra computed from averaging independent realizations of the stochastic dynamics. The rightmost vertical dashed line is traced at ω_0, the leftmost at ω_1. Here $r = 50$, $D = 10$ and $V = 10^6$.

moments. It is immediate to show that the first moments are equal to zero. We focus instead on the the $2\Omega \times 2\Omega$ family of second moments, defined as $\langle \zeta_l \zeta_m \rangle = \int \zeta_l \zeta_m \Pi d\boldsymbol{\zeta}$. A straightforward calculation (see Appendix C) yields:

$$\begin{aligned} \frac{d}{d\tau} \langle \zeta_l^2 \rangle &= 2 \langle \zeta_l (J\boldsymbol{\zeta})_l \rangle + \mathcal{B}_{ll} \\ \frac{d}{d\tau} \langle \zeta_l \zeta_m \rangle &= \langle \zeta_l (J\boldsymbol{\zeta})_m \rangle + \langle \zeta_m (J\boldsymbol{\zeta})_l \rangle \end{aligned} \tag{4.9}$$

for respectively the diagonal and off-diagonal $(l \neq m)$ moments. Here $\mathcal{B}$ stands for the diffusion matrix of the Fokker-Planck equation for the perturbations ζ, it is diagonal and constant, its entries being equal to $\frac{1}{V}$. The

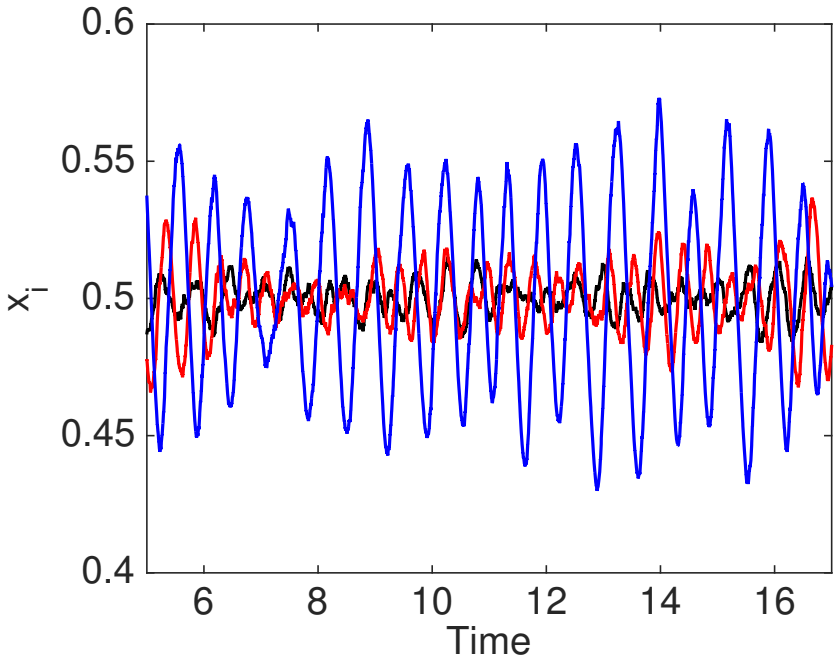

Figure 4.3: Stochastic trajectories on different nodes. Noisy self-sustained oscillation of modest amplitude are displayed on the first node of the lattice (black line). The amplitude of the oscillations grows steadily across the chain (red line on node 2 and blue line on node 8) and become progressively more regular.

stationary values of the moments can be analytically computed by setting to zero the time derivatives on the left hand side of equations (4.9) and solving the linear system that is consequently obtained. We are in particular interested in accessing $\sigma_i = \sqrt{\langle \zeta_i^2 \rangle}$, the standard deviation of the fluctuations around the deterministic equilibrium, on node i. The value of σ_i, normalized to σ_1 and expressed in decibel [dB], is plotted against the node index along the lattice in Figure 4.4. The data refer to the excitatory species. The solid line stands for the analytical estimate, that implements the above strategy. We notice that the standard deviation of the fluctuations grows exponentially

along the chain. As we will explain later this was expected since our system is prone to convective instability (see Section 4.2.4). Symbols refer instead to direct integration of equations (4.2), for different choices of the volume V_1. The agreement with the theory prediction based on the linear ansatz is excellent over a finite portion of the chain. When $\sigma_i \simeq 1/2$ (horizontal dashed line) the system senses the boundary, non-linearities come into play and induce the observed saturation. By increasing V_1, one reduces the amplitude of the endogenous fluctuations: the signal has therefore to travel through a larger set of contiguous nodes before the amplitude of the oscillation can hit the extinction edge. As a consequence, the linear approximation holds over a larger portion of the scrutinized chain.

The rate of exponential growth (relative to the excitators species), as predicted from the computation of the standard deviation σ_i, is plotted with an appropriate color code, in the reference parameters plane (r, D), see Figure 4.5. The amplification takes place within a bounded region in (r, D), as delimited by the two solid (white) lines. The straight line that sets the rightmost frontier of the amplification domain is obtained as $r = D/2$, namely the condition of existence of a complex imaginary part in the degenerate eigenvalues $\lambda_{3,4}$ (which in turn select the frequency ω_1 to be amplified). The boundary that delimits the region of interest on the left follows a closed analytical estimate that can be obtained by truncating long range correlations in the estimate of the multivariate moments to nearest neighbors (see Appendix E). The dashed (white) line refers to D_c vs. r and it is depicted for the sake of completeness. Similar results (not shown) apply to the inhibitors.

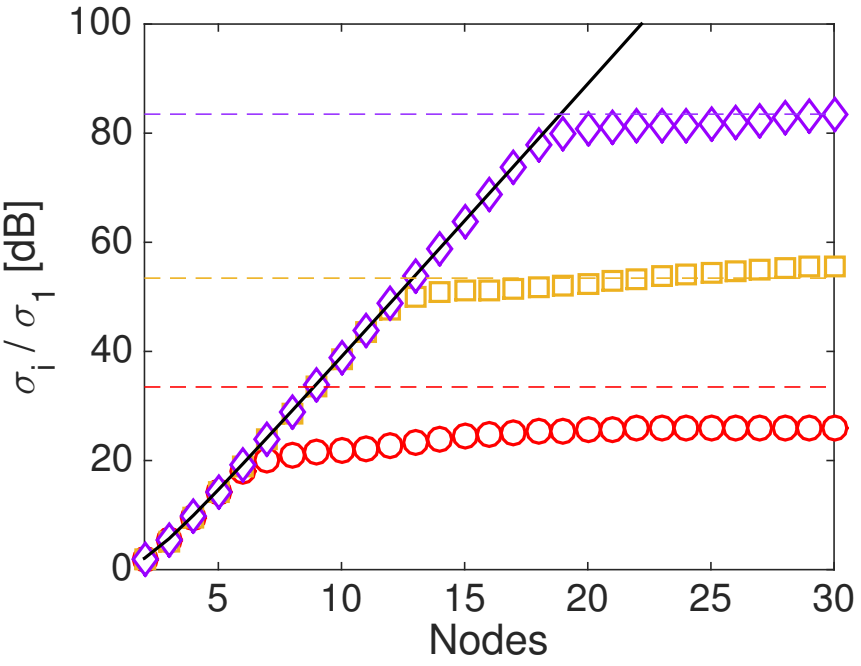

Figure 4.4: σ_i/σ_1 (in decibel [dB] logarithmic scale) is plotted against the index which identified the ordering of the nodes along the lattice. Data refer to the exicitatory species. The solid line stands for the analytical estimate obtained under linear noise approximation. The amplification process is clearly exponential. Symbols refer to direct integration of equations (4.2), for different choices of the volume V_1 (10^6, circles; 10^{12}, squares; 10^{18}, diamonds). The horizontal dashed lines show where the linear estimate predicts $\sigma_i \simeq 1/2$, namely when saturation is theoretically expected to occur. Here $D = 10$, $r = 50$.

4.2.3 Non-Normality

Now that we have entirely characterized the amplification process we still have to answer the following question; where does this amplification come from? This is all due to the specific structure of our Jacobian which is said to be *non-normal*. Indeed, the fact that non-normality amplifies transient dynamics was already well known, it has been observed in many different

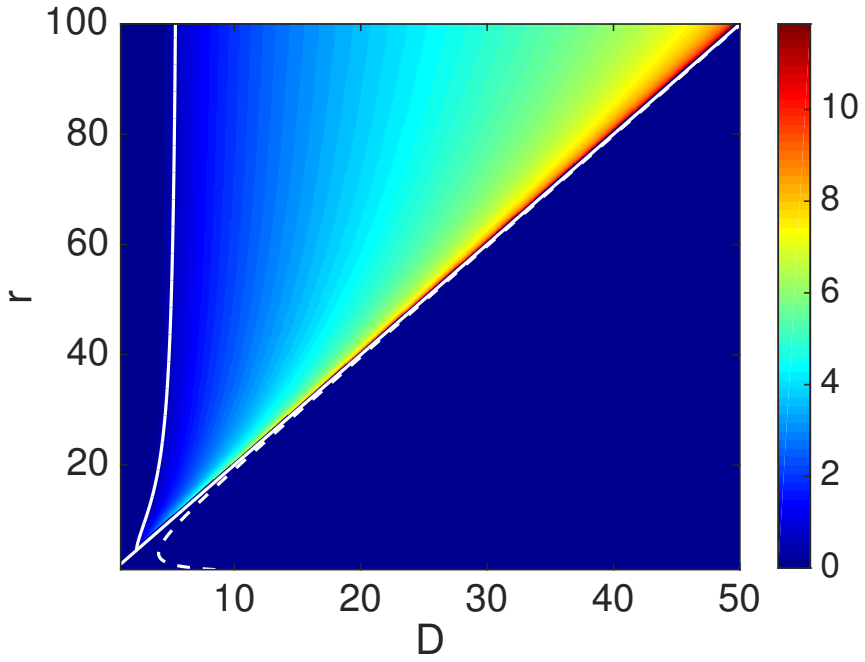

Figure 4.5: The rate of exponential amplifications (for the excitators) is depicted in the plane (r, D). The domain where the amplification is expected to take place are delimited by the two solid curves. The dashed line refers to D_c vs. r.

fields from fluid mechanics [61] to ecological systems [62].

A matrix $\boldsymbol{A}$ is said to be *non-normal* if it does not commute with its conjugate, that is

$$\boldsymbol{A}\boldsymbol{A}^* \neq \boldsymbol{A}^*\boldsymbol{A} \tag{4.10}$$

This also means that its eigenvectors do not necessarily form an orthogonal basis of $\mathbb{C}^n$ with n the dimension of the matrix. A possible measurement to quantify the non-normality of a matrix is the *numerical abscissa*. For a given

matrix $\boldsymbol{A}$ it is defined by

$$\kappa(\boldsymbol{A}) = \sup \sigma \left(\frac{\boldsymbol{A} + \boldsymbol{A}^*}{2} \right) \tag{4.11}$$

where $\sigma(\boldsymbol{A})$ denotes the spectrum of the matrix $\boldsymbol{A}$ and $\boldsymbol{A}^*$ its conjugate transpose. Now let's assume that the matrix $\boldsymbol{A}$ is the Jacobian of a stable dynamical system, in other words, $\sup \operatorname{Re} \boldsymbol{\sigma}(A) < 0$. If the numerical abscissa $\kappa(\boldsymbol{A})$ is negative, then the orbits will exponentially converge to the fixed point. On the other hand, if $\kappa(\boldsymbol{A})$ is positive, a transient growth of size proportional to $\kappa(\boldsymbol{A})$ will occur. [1] Let's take our system, where have set $D = 10$, $r = 50$ and $\gamma_i = 1$, to exemplify what we just described. First, we consider a single node which Jacobian $\boldsymbol{J}_1$ is the matrix $\boldsymbol{E}_1$ given in (4.4), we find that $\kappa(\boldsymbol{J}_1) = -1$ meaning that no transient will occur and that the oscillations will exponentially approach the fixed point. If we now focus on respectively 2 and 3 nodes chain, we find that the degree of non-normality of the Jacobian becomes positive and grows with the chain length. We have respectively $\kappa(\boldsymbol{J}_2) = 2.5355$ and $\kappa(\boldsymbol{J}_3) = 3.3301$ for the 2-nodes and the 3-nodes chain. On Figure 4.6 are displayed the signals of the perturbation on node i, $x_i(t)$, for the linearized system and their respective envelopes (thicker lines). It shows that the perturbation on node 1 (red line) undergoes no transient and exponentially approach the fixed point contrary to nodes 2 (blue line) and 3 (green line). Accordingly to what we expect from their numerical abscissa, the perturbation on node 3 goes through a more amplifying transient as compared to the perturbation on node 2. If each node is getting more amplified than its precursor, this is obviously because of the unidirec-

[1] It is immediate that in cases in which matrix $\boldsymbol{A}$ is symmetric (and stable) $\kappa(\boldsymbol{A}) < 0$.

tionality of our network. Adding a node to our system, and therefore a block to its Jacobian, will enhance the degree of non-normality and consequently reinforce the amplification.

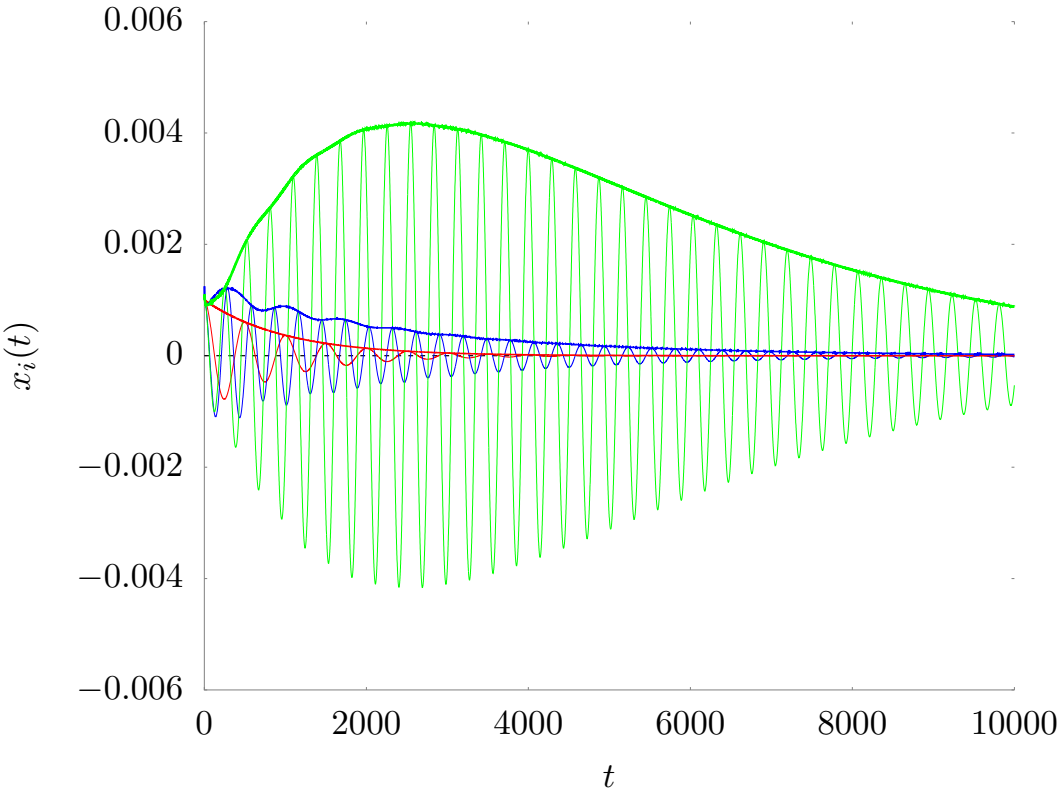

Figure 4.6: Time evolution for the pertubations $x_i(t)$. Each color stands for a specific node. In red is depicted the trajectory of the pertubation on node 1, in blue the trajectory on node 2 and in green the trajectory on node 3. The parameters here are $D = 10$, $r = 50$ and $\gamma_i = 1$.

The situation is even more intriguing for stochastic systems. Indeed, noise constantly injects dynamics into the system making the transient regime perpetual. This notably explains the persistence of the amplification observed in our present model. A roughly similar situation will be discussed in the

next chapter: we will in particular show that, once again, the combination of quasi-cycles and non-normality results in a class of (convective) instabilities.

4.2.4 Convective instability

Previously, we have mentioned that the exponential nature of the amplification was not a surprise but merely the manifestation of convective instability. In the first place, let's distinguish 3 possible situations:

- Absolute stability: a system is absolutely stable when any perturbation will be damped, and this in any frame of reference.
- Absolute instability: a system is absolutely unstable when the edges of the perturbations move in opposite direction, propagating and amplifying the instabilities at any stationary point of the system. We'll never face such a situation since we focus our study in a region of parameter where our system is absolutely stable ($D < D_c$).
- Convective instability: contrary to absolute instability, in this case, the edges of the perturbation move in the same direction and consequently the perturbation will grow exponentially in a moving frame of reference.

In Figure 4.7 are depicted the 3 different situations that we have described above. In blue is drawn a system which is absolutely unstable, the edges of the perturbations, centered in x_0 at $t = 0$, move in opposite directions. It will, therefore, propagate over all the x-axis. In red is depicted an absolutely stable system, over time the perturbation decreases until the system is back to its state before the perturbation. In the lower panel is shown a convectively

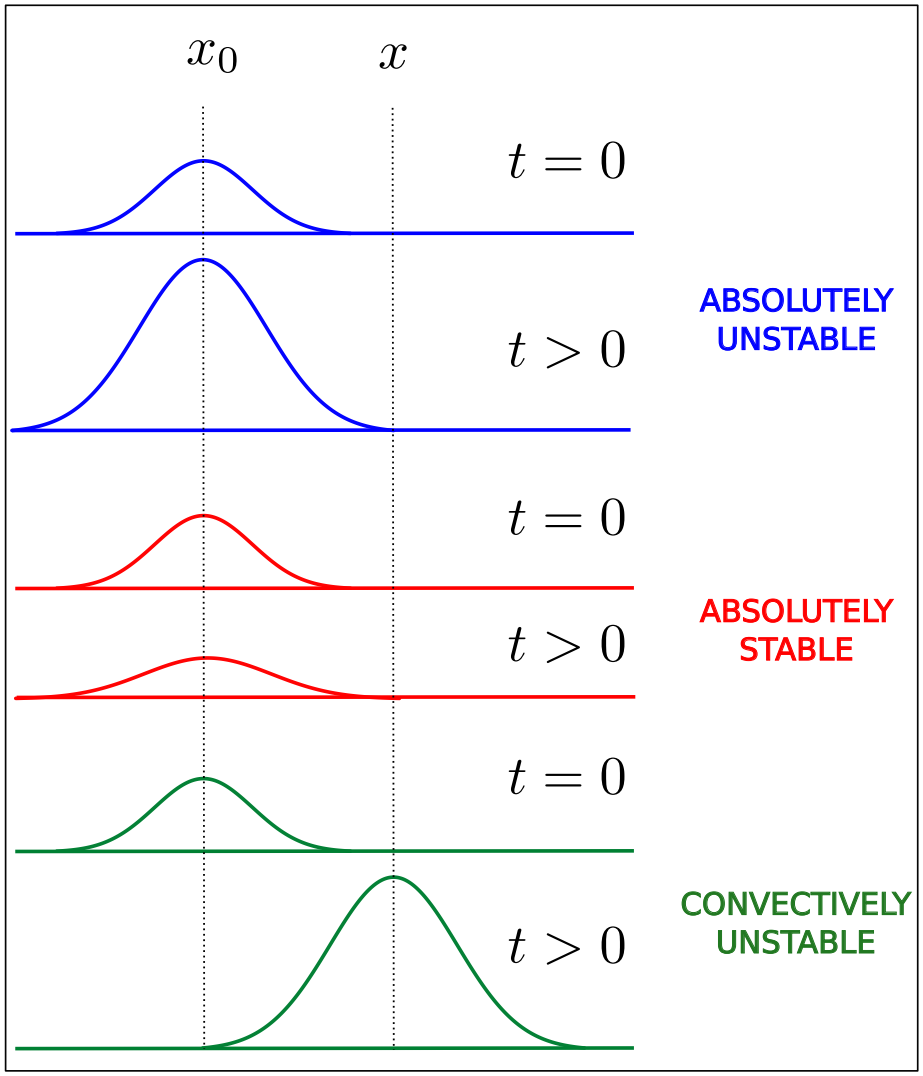

Figure 4.7: Illustration of the 3 possible situations that we may encounter for our system [63].

unstable system. The edges of the perturbations are moving in same the direction along the x-axis which is the frame of reference here. It exists a set of velocities v such that, at time t, the perturbations in $x = vt + x_0$ will have increased exponentially compared to what it was initially. However,

if we fix our attention on one particular point of space, say x_0, we will see the perturbation decreasing exponentially in time as for the absolutely stable case.

In order to show that convective instability occurs in our system, let us introduce at $t = 0$ a tiny pertubation on the first node and then observe at different time the spatial composition along the chain. The results are shown on Figure 4.8. The perturbation inserted on the first node at $t = 0$ has been propagating and amplifying with node index. This confirms that our system undergoes convective unstability. Most of the time, the prediction of

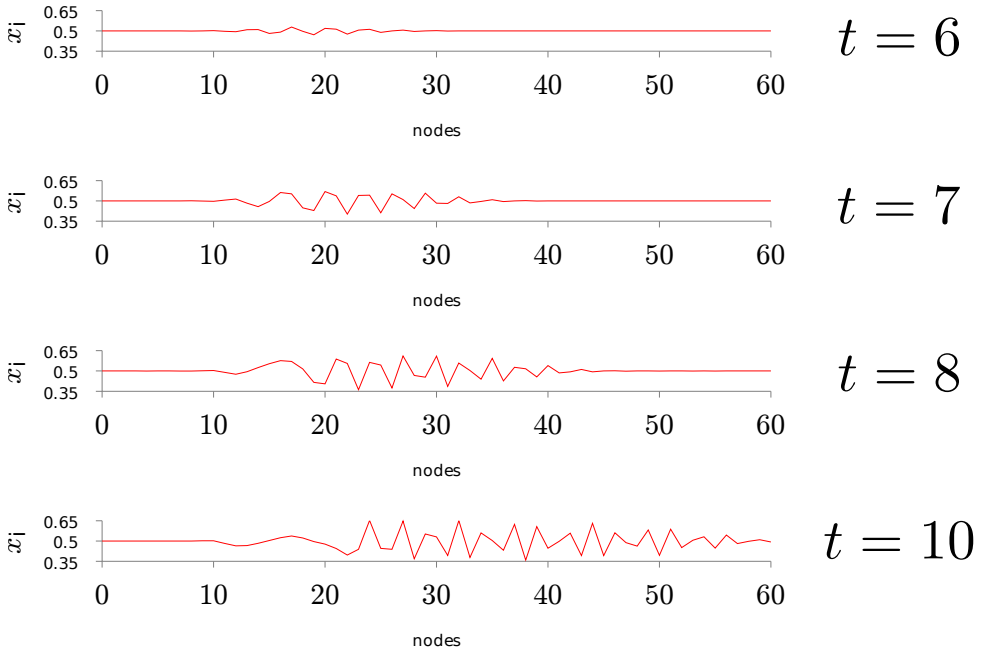

Figure 4.8: Illustration of the manifestation convective instability in our system. A perturbation inserted on the first node at time $t = 0$ propagates and amplify along the chain.

convective instability might not be carried out by means of a standard linear analysis. However, more sophisticated techniques based on the chronotypic

Lyapunov analysis [64, 65, 66] have been developed to tackle such problems.

4.3 Other configurations and possible applications

The noise assisted amplification process that we have here characterized is very flexible and can be configured in different schemes. We are about to present two possible configurations, one to amplify a frequency harmonic of ω_0, and a second to amplify on a frequency comb.

4.3.1 Amplifying the harmonics of ω_0.

To amplify the harmonics of ω_0 for any given D, within the domain deputed to the amplification, we can modulate the volumes of the nodes, following the strategy discussed below. Label V_1 the volume of the first node. Recall that $\omega_1 = \sqrt{\frac{r}{8}\left(\frac{r}{2} - D\right)}$ identifies the frequency that gets amplified when the volumes are identical, or, equivalently, when $\gamma_i = 1\ \forall i$. To force the emergence of a second peak in $\omega_0/2$, on the second node of the lattice, one needs to impose the condition

$$\frac{\omega_1}{\gamma_2} \equiv \frac{\omega_0}{2} \tag{4.12}$$

which readily translates in

$$V_2 = 2V_1\frac{\omega_1}{\omega_0} \tag{4.13}$$

To enforce the amplification of a train of successive harmonics one can expand on the above recipe and eventually obtain the following condition for the relative modulation of the volumes:

$$V_i = 2^{i-1}\frac{\omega_1}{\omega_0}V_1 \qquad i \geq 2 \tag{4.14}$$

In practice, to allow for the amplification to produce significant intensities of the signal at each frequency, one could keep the volumes constant over a few consecutive nodes, before increasing the size of the volumes of the successive set of nodes, as prescribed by formula (4.14). In Figure 4.9 we assumed a sequence of nodes with volumes $(V_1, V_2, V_2, V_3, V_3, V_3)$. The power spectra depicted in Figure 4.9 refer to the first, third and sixth nodes of the chain, respectively.

4.3.2 Amplifying on a frequency "comb"

We shall here demonstrate that the amplification can take place on a frequency comb. We shall in particular amplify a set of frequencies $\omega_k = \omega_0 - k\Delta\omega$ with $k = 0, 1, 2, ..;$ $\Delta\omega$ is positive and represents the relative distance between two consecutive frequency peaks. Reasoning as in the preceding section, we want to assign the volume of the second node so as to meet the condition

$$\frac{\omega_1}{\gamma_2} - \omega_0 \equiv -\Delta\omega \tag{4.15}$$

which translates into:

$$V_2 = \hat{V}\frac{1}{\omega_0/\Delta\omega - 1} \tag{4.16}$$

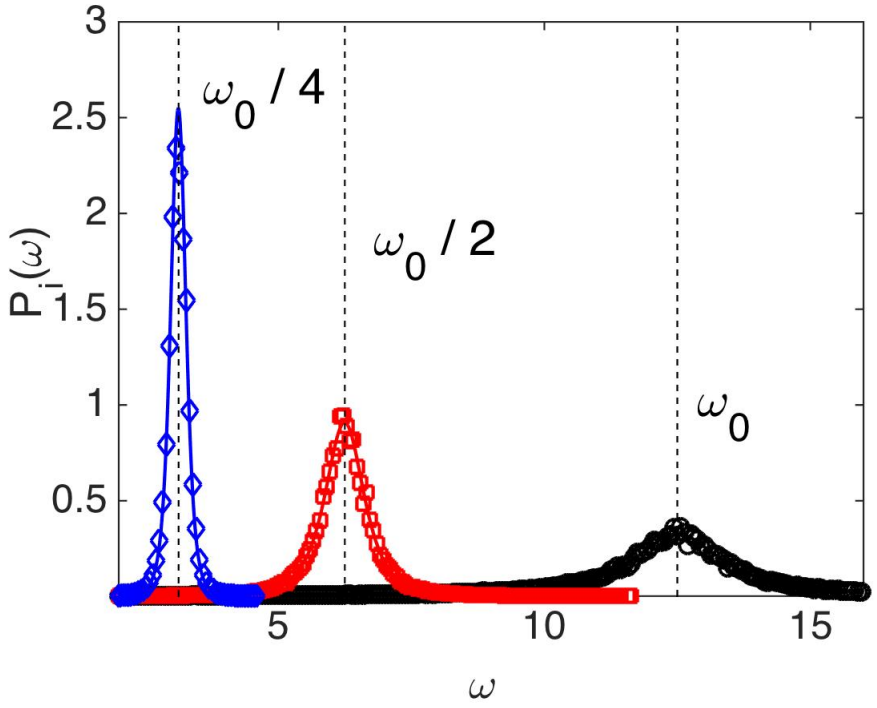

Figure 4.9: Amplifying the harmonics of ω_0, following the scheme that yields to equation (4.14). The power spectra of fluctuations on different nodes (see text) are displayed. Symbols refer to direct simulations and the solid lines to the theory prediction.

where $\hat{V} = \frac{\omega_1}{\Delta\omega} V_1$. Based on the same reasoning, we get for the other nodes the following recursive relation:

$$V_i = \frac{V_{i-1}}{1 - \frac{V_{i-1}}{\hat{V}}} \tag{4.17}$$

As discussed in the preceding section, one can keep the volumes unchanged over a few consecutive nodes, before modulating their size as prescribed by formulae (4.16) and (4.17), so to enhance the amplification power of the device. In Figure 4.10 we exposed a chain that implements the sequence of

volumes $(V_1, V_2, V_2, V_3, V_3, V_3)$. The power spectra displayed in Figure 4.10 refer to the first, third and sixth nodes, respectively. In both cases, the

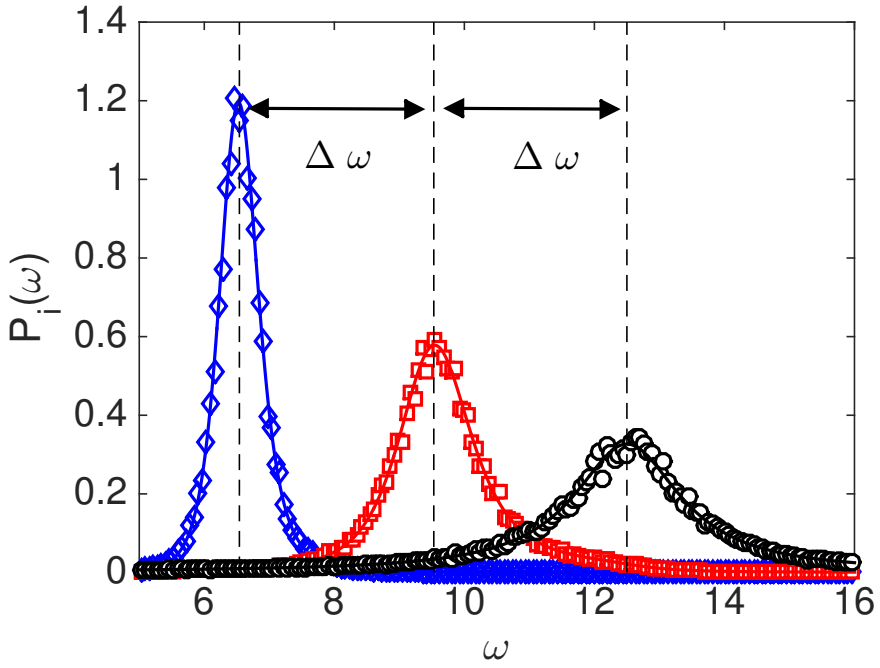

Figure 4.10: Amplifying a frequency comb. Here, $\omega_k = \omega_0 - k\Delta\omega$ with $k = 0, 1, 2, ...$ The positive quantity $\Delta\omega$ denotes the separation between two consecutive frequencies. The size of the volumes of the nodes are set as prescribed by equations (4.16) and (4.17). The power spectra of fluctuations on different nodes (see text) are displayed. Symbols refer to direct simulations and the solid lines to the theory prediction.

self-sustained amplification is fueled by the inherent component of noise, stemming from finite size corrections. At variance, one could imagine to assemble a device that operates in the deterministic $V_i \to \infty$ limit. If $D < D_c$, the system is frozen in its homogeneous equilibrium, the concentration of both x_i and y_i being identical to $1/2$ on each node. Assume now that a perturbation, limited in time and modest in amplitude, hit on the first node.

The disturbance propagates along the chain and gets magnified, following the scheme that we outlined above, exciting on site oscillations at a given frequency ω_1, that could be freely tuned by acting e.g. on D. Such an apparatus could efficaciously act as a signal detector. Even more interesting, one could foresee the possibility of assembling a detector that exploits parallel lines of detection. On each line a different value of the coupling D could be enforced. In doing so, from the trace of the amplified signal at the end of the chain (processed with a standard frequency analyzer), it could be possible to identify the node (hence the chain) where the perturbation hit. This observation opens up the perspective to define a novel class of detectors that could spatially resolve low intensity alerts. This is exemplified in Figure 4.11.

4.4 A thermodynamical interpretation

Finally, we will derive a consistent thermodynamic interpretation of the process that underlies the spontaneous generation of giant quasi-oscillations. Our analysis follows the approach pioneered by [67, 68, 69, 70] to study the thermodynamics of far-from-equilibrium systems, which are microscopically amenable to stochastic continuous time Markovian processes. Given the probability density $P(\boldsymbol{v}, \tau)$ that satisfies a Fokker-Planck equation equivalent to the Langevin equations (4.2), we define the entropy

$$S(\tau) = -\int P(\boldsymbol{v}, \tau) \ln P(\boldsymbol{v}, \tau) d\boldsymbol{v} \tag{4.18}$$

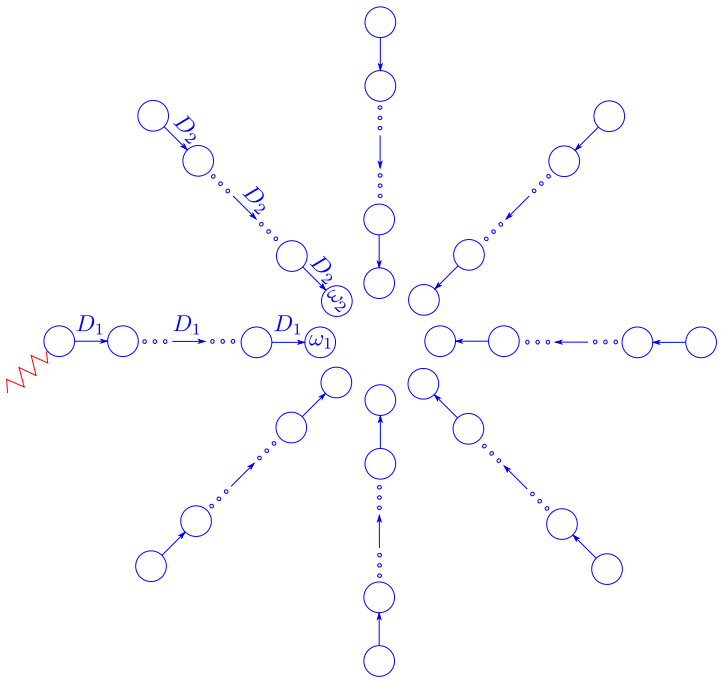

Figure 4.11: Here is depicted a schematic view of a signal detector. Each branch differs from the successive by its coupling value D. Doing so, the output main frequency will be different for every branch, this would allow us to detect and spatially locate arbitrary small signals.

A straightforward manipulation yields $dS/dt = \Pi_S - \Phi_S$, where

(i) Π_S is positive defined and represents the rate of entropy production due to the non-conservative forces at play

(ii) Φ_S stands for the entropy flux, which is positive if the entropy flows from the system to the environment.

Their explicit expressions read (more details on their derivation are given in Appendix E)

$$\Pi_S = \sum_i \frac{2}{B_{ii}} \int \frac{I_i^2(\boldsymbol{v}, \tau)}{P(\boldsymbol{v}, \tau)} d\boldsymbol{v} \tag{4.19}$$

$$\Phi_S = \sum_i \frac{2}{B_{ii}} \int A_i(\boldsymbol{v}) I_i(\boldsymbol{v}, \tau) d\boldsymbol{v} \tag{4.20}$$

where

$$I_i = A_i P - \frac{1}{2} B_{ii} \frac{\partial}{\partial v_i} P \tag{4.21}$$

is the probability density current associated to the same Fokker-Planck equation as for equation (4.18). A stationary balance is attained when $\Phi_S = \Pi_S$, a condition that proves equivalent to imposing

$$\sum \frac{\partial}{\partial v_i} I_i = 0 \tag{4.22}$$

The condition of solenoidal current, $\boldsymbol{\nabla} \cdot \boldsymbol{I} = 0$ is indeed met when the Fokker-Planck equation attains its non trivial dynamical equilibrium ($I_i \neq 0$). In other words, the observed amplification stems from a genuine noise driven out-of-equilibrium process, the neuromorphic device working under stationary operating conditions. The rate of entropy production as computed analytically under a linear prescription grows exponentially, see Appendix E. A cross-over towards a non exponential regime is eventually observed when non-linearities become prominent, in complete agreement with the insight gained under a purely dynamical angle.

4.5 Conclusion

In conclusion, we have shown how a minimal model of neuronal population dynamics can be assembled to behave as a fully tunable amplifier. We have performed a complete characterization of the amplification mechanism, in the

first place by means of its spectral study. In the second place, we derived the equations for the moments of the probability distribution of the perturbations around the deterministic equilibrium. While the first moment converged to zero, it is the standard deviation that grows exponentially along the chain. We also briefly discussed the origin of this amplification which arises from the non-normality of the Jacobian. We took advantage from the flexibility of this system to design two possible schemes which bear some general interest. First we showed how to amplify the harmonics of a specific frequency and then we considered a frequency comb amplification. Such amplification feature could be employed in a vast gallery of concrete application such as a spatially distributed detector of low-intensity noisy signals. To conclude, we demonstrated that our system extracts energy from a finite size bath operating as an out-of-equilibrium thermal machine under stationary conditions. It is worth noting that this amplification process could also provide a reliable pacemaking mechanism for biological systems.

This work led to the following publication: *Noise driven neuromorphic tuned amplifier*, Fanelli D., Ginelli F., Livi R., and Zankoc C., Phys. Rev. E **96**, 062313 (2018)

Chapter 5

Desynchronization and pattern formation in a noisy feedforward oscillator network

In this chapter, we consider a one-dimensional directional array of diffusively coupled oscillators. They are perturbed by the injection of small additive external noise, typically orders of magnitude smaller than the oscillation amplitude, and the system is studied in a region of the parameters that would yield deterministic synchronization. Non-normal directed couplings seed a coherent amplification of the perturbation: this latter manifests as a modulation, transversal to the limit cycle, which gains in potency node after node. If the lattice extends long enough, the initial synchrony gets eventually lost, and the system moves toward a non-trivial attractor, which can be characterized as an asymptotic splay state. The noise assisted instability, ultimately carried and amplified by the non-normal nature of the imposed couplings,

eventually destabilizes also this second attractor. This phenomenon yields spatiotemporal patterns, which cannot be anticipated by a conventional linear stability analysis.

5.1 Deterministic Ginzburg-Landau oscillators: synchronized and splay states

Our model consists of Ω diffusively and unidirectionally coupled Ginzburg-Landau oscillators. Each oscillator is described by the complex variable W_j $(1 \leq j \leq \Omega)$. The oscillators in this directionally coupled chain (see Fig. 5.1) obey the following ordinary differential equations

$$\frac{\mathrm{d}W_1}{\mathrm{d}t} = W_1 - (1 + ic_2)|W_1|^2 W_1 \tag{5.1a}$$

and, for $j > 1$

$$\frac{\mathrm{d}W_j}{\mathrm{d}t} = W_j - (1 + ic_2)|W_j|^2 W_j + (1 + ic_1)K(W_{j-1} - W_j) \tag{5.1b}$$

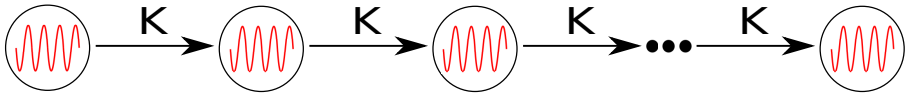

Figure 5.1: Schematic representation of our system. Each node carries an oscillator and is unidirectionally coupled to its successive neighbour. Parameter K modulates the coupling.

where c_1, c_2 are real parameters and K denotes the coupling strength. It is obvious that changing the sign of K and at the same time inverting the boundary conditions is equivalent to reversing the information flow along the chain: therefore in the rest of this paper K is assumed to be positive. The system is also symmetric under the following transformation: $W_j \to W_j^*$, $(c_1, c_2) \to -(c_1, c_2)$ which allows us to restrict our focus on half of the (c_1, c_2) parameter plane. Two types of solution are of interest, the *synchronized* and the *splay* ones. The synchronized state (usually denoted as *homogeneous state*, in the vast literature of spatially coupled oscillators) corresponds to the solution

$$W_j = \exp(-ic_2 t) \quad , \quad j = 1, \cdots, \Omega. \tag{5.2}$$

By direct inspection of Eq. (5.1a) and (5.1b) one can check that any dependence on the spatial coupling K and on the parameter c_1 disappears, and that this solution exists for any value of c_2.

The splay states are a family of uniformly rotating solutions with finite constant-in-time phase differences between consecutive nodes. These states can be characterized making use of the general polar representation $W_j = \rho_j \exp(i\theta_j)$ and first imposing the stationarity condition $\dot{\rho}_j = 0$ for $j > 1$. Moreover, by introducing the constant-in-time phase differences $\phi_j = \theta_j - \theta_{j-1}$, the stationary conditions applied to Eq. (5.1b) yield the recurrence equations

$$\rho_j = \sqrt{\left(1 + K\left[\frac{\rho_{j-1}}{\rho_j} f(\phi_j) - 1\right]\right)} \tag{5.3a}$$

$$0 = c_2(1 - \rho_j^2) + K\left[\frac{\rho_{j-1}}{\rho_j} g(\phi_j) - c_1\right] \tag{5.3b}$$

where

$$f(\phi_j) = \cos\phi_j + c_1 \sin\phi_j \tag{5.4a}$$

$$g(\phi_j) = c_1 \cos\phi_j - \sin\phi_j. \tag{5.4b}$$

The initial condition for this recurrence equations stems from Eq. (5.1a), i.e. $\rho_1 = 1$ and $\theta_1 = -c_2 t$. Notice that the stationary solution on the first node coincides with the synchronized state. We avoid reporting explicit calculations, but it can be easily shown that for the set of parameters considered in this paper (e.g., see the caption of Fig. 5.2) the recurrence equations equipped with this initial condition admit a unique stable nonhomogeneous solution, which spatially converges to the splay state

$$\rho_\infty = \sqrt{1 + K\left(f(\phi_\infty) - 1\right)} \tag{5.5a}$$

$$\phi_\infty = 2\tan^{-1}\left[\frac{1 + c_1 c_2}{c_2 - c_1}\right] \tag{5.5b}$$

The special case $\phi_\infty = \pm\pi$ occurs in the limit $c_2 \to c_1$. In practice, one finds that the spatially asymptotic splay state is rapidly approached along the chain (see Fig. 5.2)

The rate of convergence depends on the parameters K, c_1 and c_2, however, for the sake of space, we do not report any detailed investigation on this point.

It is important to point out that the existence condition for the splay state is that ρ_∞ is real, i.e. that the argument of the square root in Eq. (5.5a) is

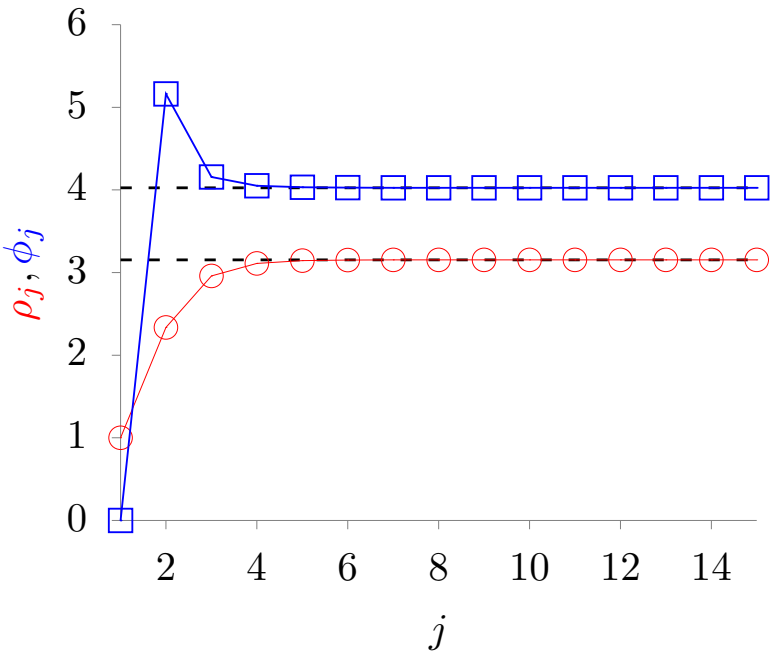

Figure 5.2: SPLAY STATE REPRESENTATION The radius of the limit cycles over the chain ρ_j is depicted by the red solid line (circles), while the blue line (squares) stands for the phase difference $(\mathrm{mod}\, 2\pi)$ between two successive nodes. As expected, they converge to the asymptotic values ρ_∞, ϕ_∞ (dashed black lines). The parameters here are $c_1 = -5$, $c_2 = 4$ and $K = 4$.

non-negative. As an example, in Fig. 5.3 we show the region in the (c_1, c_2)-plane where the splay state exists for $K = 4$: the colour code corresponds to different positive values of ρ_∞, while the black region indicates where the splay state does not exist.

As a final remark, we want to point out that there exists an entire family of solutions asymptotically approaching along the chain the splay state (see Eq. (5.3)). In these solutions the synchronous state extends to an arbitrary

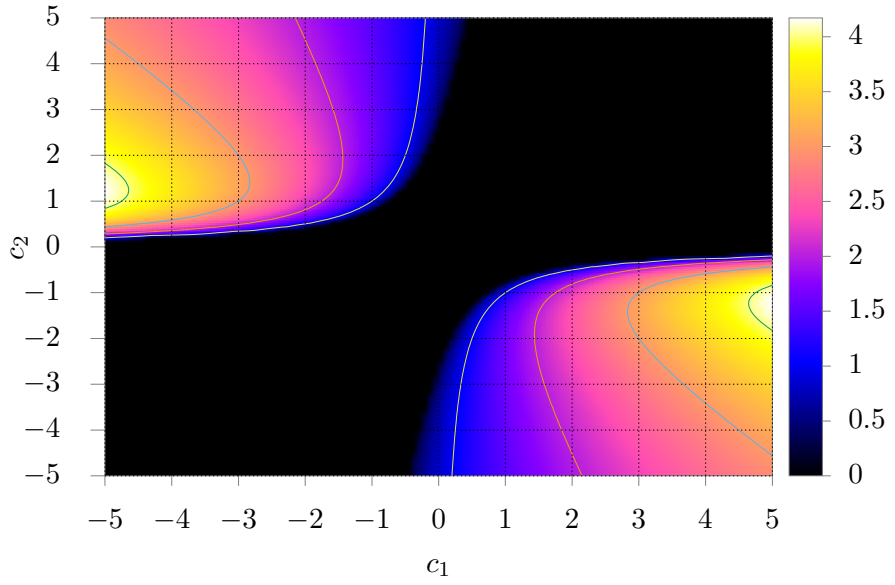

Figure 5.3: SPLAY STATE EXISTENCE: the color represents the value of ρ_∞ (see Eq.(5.5a)), while the black zone refers to the region where the splay state does not exist. The solid lines correspond to the isocurves of ρ_∞. Here $K = 4$.

large initial portion of the chain, namely $\rho_j = 1$ and $\phi_j = 0$ for $j = 2, \cdots, \bar{j}$. For $j > \bar{j}$ constant-in-time phase differences become finite and the solution converges to the asymptotic splay state (5) for large j. As we shall discuss later, the existence of this entire family of splay states impacts on the way noise destabilizes the homogeneous synchronized state determining a typical spatio-temporal pattern organization for the stochastic system.

5.1.1 Stability of synchronized and splay states

In order to investigate the stability of the synchronous and of the splay states we can perform a standard linear stability analysis. We first introduce small perturbations $\delta\rho_j, \delta\theta_j$ of the limit cycles, $W_j = (\rho_j + \delta\rho_j)\exp(i(\theta_j + \delta\theta_j))$ for $1 \leq j \leq \Omega$. Linearizing and retaining the first order in the pertubations leads to an equation that can be put in the general matrix form $\delta\dot{\mathbf{v}} = \mathbf{J}(\rho, \theta)\delta\mathbf{v}$ (we adopt the shorthand notation $(\rho, \phi) = (\rho_1, \phi_1, \rho_2, \phi_2, \cdots, \rho_\Omega, \phi_\Omega)$), where $\delta\mathbf{v} = \delta(\rho, \phi)$ is the vector of perturbations and $\mathbf{J}$ is the Jacobian matrix associated to dynamics (5.1). Due to the unidirectional nature of the coupling K, $\mathbf{J}$ exhibits a lower tridiagonal block structure. Hence, to assess the stability of any state it is enough to compute the eigenvalues λ_{ρ_j} and λ_{θ_j} for $1 \leq j \leq \Omega$ of the diagonal 2×2 blocks constituting $\boldsymbol{J}$

$$\mathbf{A}_1 = \begin{pmatrix} -2 & 0 \\ -2c_2 & 0 \end{pmatrix} \tag{5.6a}$$

and

$$\mathbf{A}_j = \begin{pmatrix} (1 - 3\rho_j^2 - K) & K\rho_{j-1}g(\phi_j) \\ -\left(2c_2\rho_j + K\frac{\rho_{j-1}}{\rho_j}g(\phi_j)\right) & -K\frac{\rho_{j-1}}{\rho_j}f(\phi_j) \end{pmatrix} \tag{5.6b}$$

for $2 \leq j \leq \Omega$.

The eigenvalues of the first block A_1 are $\lambda_{\rho_1}{=}{-}2$ and $\lambda_{\theta_1}{=}0$, the latter reflecting marginal stability towards global phase rotations. A given limit cycle solution is stable only if the complex eigenvalues of all the other blocks have a negative real part, i.e. $\Re(\lambda_{\rho_j}) < 0$ and $\Re(\lambda_{\theta_j}) < 0$ for $2 \leq j \leq \Omega$.

The synchronized state, where $\rho_j = 1$, $\phi_j = 0 \quad \forall j > 1$, is stable independently of K for $1 + c_1 c_2 \geq 0$, while for $1 + c_1 c_2 < 0$ only if the following condition holds:

$$K > K^H_{min} = -\frac{2(1 + c_1 c_2)}{1 + c_1^2} \,. \tag{5.7}$$

Therefore, for each couple (c_1, c_2) we can find a minimum coupling value K^H_{min} such that the synchronized state is stable. The resulting stability map is shown in Fig. 5.4. Notice that the condition $1+c_1 c_2 < 0$ is sufficient for the onset of the instability, when the CGLE is defined on a continuous spatial support [71]. In fact, this is known as the condition of the Benjamin-Feir instability for the CGLE [72, 71].

Stability analysis is more complicated for the splay state. Making use of the recurrence relations (5.3) we can first compute ρ_j and θ_j to evaluate the Jacobian blocks $\mathbf{A}_j$ (see Eq. (5.6b)). Then we can assess the stability of the splay state in the plane (c_1, c_2) by computing the Jacobian matrix eigenvalues. An example of the outcome of this procedure is shown in Fig. 5.5, where the parameters have been set to the values $c_1 = -5$, $c_2 = 4$ and $K = 4$. Here all eigenvalues for $j > 1$ have a negative real part so that the splay state is linearly stable. Notice the fast convergence of the eigenvalues to their asymptotic state values.

The analysis of the synchronized and splay states of the directed chain of coupled CGL oscillators is summarized in Fig. 5.6 for the case $K = 4$. The different regions of this diagram are described in the caption; the red cross locates the point in the diagram which defines our working condition as selected in the forthcoming sections when investigating the stochastic version

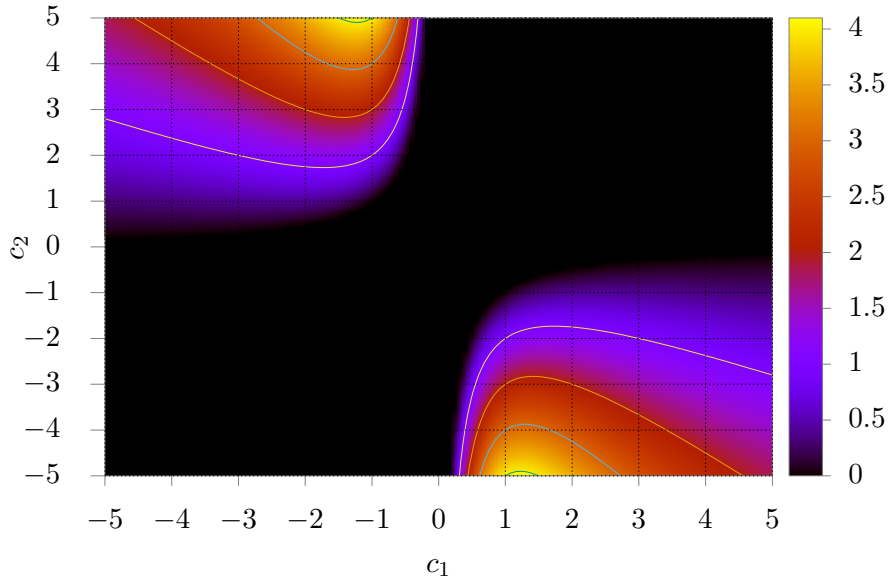

Figure 5.4: SYNCHRONIZED STATE STABILITY: On this panel we display the value of K^H_{min} (see Eq. (5.7)) beyond which the synchronized state is stable. In the black region $1 + c_1c_2 \geq 0$ and the synchronized state is always stable. The solid lines correspond to the isocurves of the heat map.

of the directed chain of coupled CGL oscillators. More details on linear stability analysis are given in Appendix F.

5.2 Effects of noise

5.2.1 Linear amplification mechanism

The stochastic version of the deterministic model (5.1) reads

$$\frac{\mathrm{d}W_j}{\mathrm{d}t} = W_j - (1 + ic_2)|W_j|^2 W_j + (1 + ic_1)K(W_{j-1} - W_j) + \sigma\eta_j(t) \qquad (5.8)$$

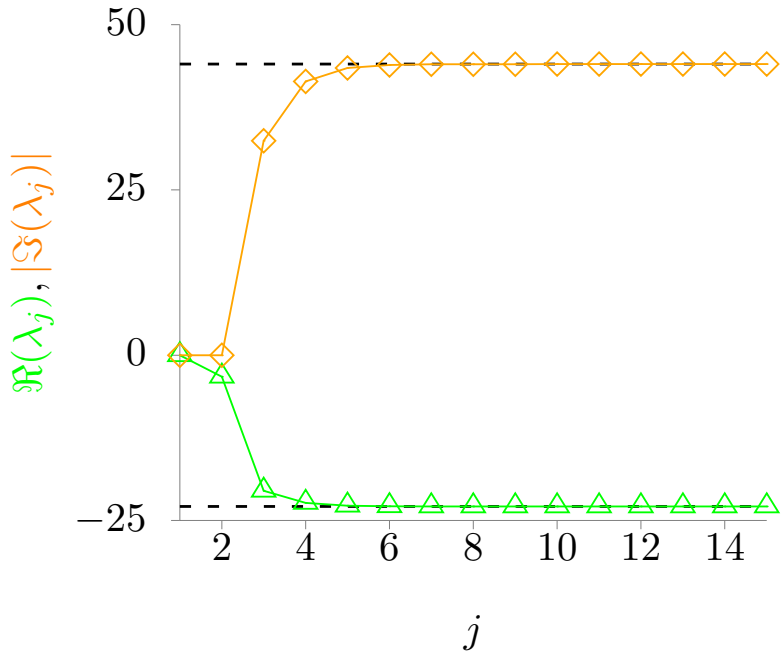

Figure 5.5: SPLAY STATE LINEAR STABILITY ANALYSIS The green curve (triangles) represents the real part of the largest eigenvalue for each node j while the yellow line (diamonds) the corresponding imaginary part. The parameters here are $c_1 = -5$, $c_2 = 4$ and $K = 4$. In this example, the splay state is characterized by $\bar{j} = 1$.

where σ is the noise amplitude, $\eta_j = \Re(\eta_j) + i\Im(\eta_j)$ is a complex additive noise with zero mean and correlators $\langle \Re(\eta_j)(t)\Re(\eta_l)(t')\rangle = \langle \Im(\eta_j)(t)\Im(\eta_l)(t')\rangle = \delta_{jl}\delta(t-t')$. In what follows the numerical investigations of the stochastic dynamics (5.8) has been performed for the parameter values $(c_1, c_2, K) = (-5, 4, 4)$ (see the red cross in Fig. (5.6)), where both the synchronized and the splay state of the deterministic dynamics are linearly stable. We want to investigate the effects of a small additive noise on the deterministic evolution (5.1) [12, 73, 74, 75]. In practice, we have always taken $\sigma = 10^{-5}$, a value which is five orders of magnitude smaller than the oscillations amplitude

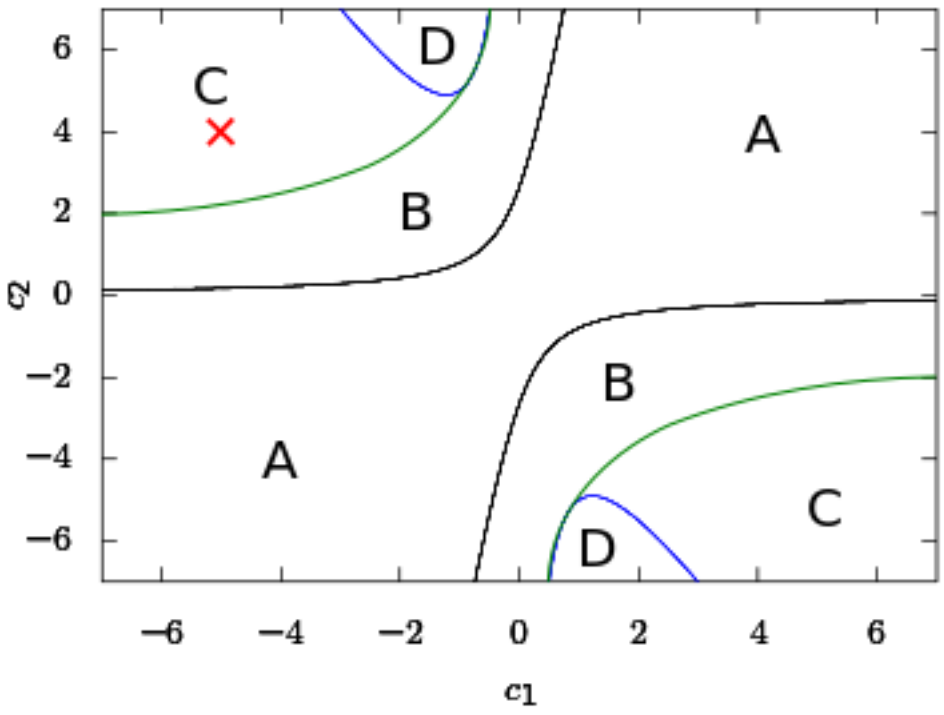

Figure 5.6: Diagram of the existence and stability of the synchronized and of the splay states for $K = 4$: in region A, whose boudaries are fixed by the condition $\rho_\infty = 0$, only the synchronized state exists and is stable; in region B both states exist, but only the synchronized one is stable; in region C both states are stable, while in region D the splay state only is stable.

of the synchronized state. As shown in Appendix G, Equation (5.8) can be rewritten for the polar components of the complex variable W_j, while the corresponding noise components remain delta-correlated and – at least near the limit cycle solutions – additive. In practice, we have studied the effects of the noise–induced fluctuations around these states. We know from the previous section that both deterministic states are indeed stable limit

cycles with a complex eigenvalues Jacobian. This guarantees the presence of stochastic oscillations, also called quasi-cycles [13, 14], on the top of the deterministic stable states. Then, we can proceed to the Fourier analysis of our system linearized around each limit cycle. We denote by $\delta\tilde{\mathbf{v}}$ and $\tilde{\xi}$ the Fourier transforms of the perturbations vector $\delta\mathbf{v}$ and of the polar white noise $\xi \equiv (\xi_\rho, \xi_\theta)$, respectively. We can readily obtain $\delta\tilde{\mathbf{v}}_j = \sum_{l=1}^{2\Omega} \mathbf{\Phi}^{-1}_{jl}(\omega)\tilde{\xi}_l$, where $\mathbf{\Phi}_{jl} = -\boldsymbol{J}_{jl} - i\omega\boldsymbol{\delta}_{jl}$. To pursue the analysis of the oscillations we compute the power spectrum density matrix of the fluctuations in the vicinity of the attractor [60]

$$\langle \delta\tilde{\mathbf{v}}_l(\omega)\delta\tilde{\mathbf{v}}_j(\omega)\rangle = \boldsymbol{P}_{lj}(\omega) = \sum_{k=1}^{2\Omega} \mathbf{\Phi}^{-1}_{lk}(\omega)\left(\mathbf{\Phi}^{\dagger}{}_{kj}\right)^{-1}(\omega). \tag{5.9}$$

Its diagonal entries are the power spectrum of transversal (j odd) and longitudinal (j even) oscillations around both solutions. We first focus on the transversal, radial, fluctuations around the synchronized state. In Fig. 5.7(a) we depict the power spectrum of several nodes. The solid line stands for the analytical power spectrum computed from equation (5.9) while symbols correspond to direct numerical simulations of equation (5.8), using the Euler-Maruyama algorithm ($\mathrm{d}t = 0.001$). The power spectrum of the first node, peaked at zero frequency (circle, black line) is the one of white noise. As we proceed along the chain, the peak of the power spectrum progrssively shifts towards higher frequencies. The profiles around the peak become narrower (thus singling out a well defined oscillation frequency), while fluctuations are amplified along the chain. This amplification can be well appreciated by direct inspection of Fig. 5.7(b). Such amplification and modulation proceeds

along the chain as long as the linear approximations holds. Out of this approximation, non-linear effects should take over and stop the amplification process. In fact the situation we are facing right now is equivalent to the one discussed in the previous chapter, the only difference being that we are now considering a collection of oscillators displaying splay state or synchrony and not a homogenous fixed point. Since the structure of the Jacobian remains essentially the same for the splay state, here we face a qualitatively identical situation. A similar amplification mechanism takes place for longitudinal fluctuations around both stable states, as exemplified in the inset of Fig. 5.7(a). However, longitudinal oscillations are typically characterized by a broader spectrum, possibly due to the softer nature of the phase direction with respect to the radial one for Ginzburg-Landau potentials. To summarize our findings, noisy fluctuations around both attractors are amplified and modulated as one proceeds along the chain to yield sharper and stronger oscillations. While non-linear effects would eventually arrest this amplification process, the linear mechanism is typically enough to overcome the attractor linear stability itself. As we already know from the previous chapter, these features are mainly due to the unidirectional structure of the Jacobian, which is highly non-normal. Non-normality amplifies transient dynamics [61, 62, 76] and may lead to convective instability [63]. Here the presence of noise makes this amplification perpetual [77].

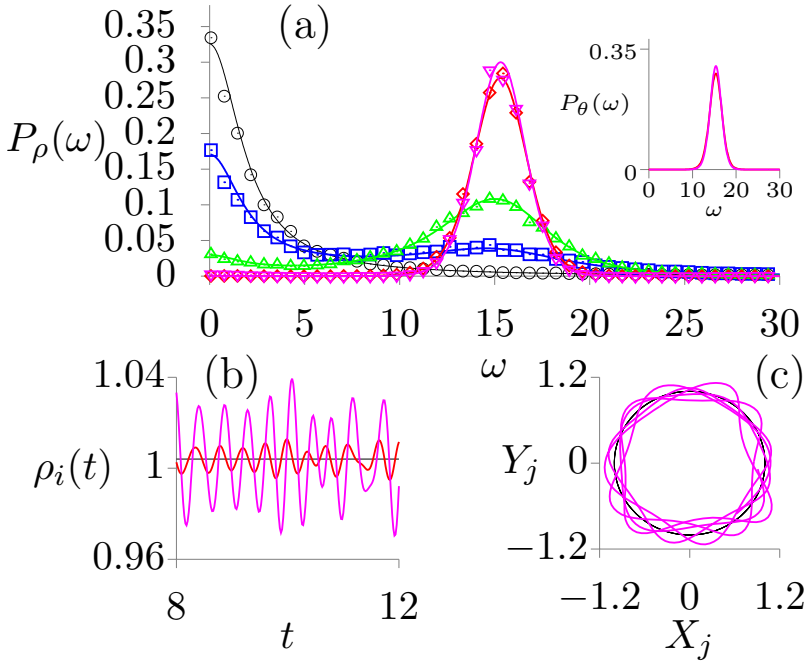

Figure 5.7: (a) Normalized power spectra of different nodes along the chain: the solid lines stands for the theoretical calculation while the symbols correspond to numerically computed power spectra using the Euler-Maruyama algorithm. The displayed agreement confirms the validity of the analytic calculations. In the inset: normalized power spectra for longitudinal fluctuations. (b) Trajectories of ρ_j. The amplification phenomenon can be clearly appreciated. (c) Phase portrait of $(X_j(t), Y_j(t))$ where X_j and Y_j respectively stand for the real and the imaginary part of the complex variable W_j. Oscillations extend along the radial direction, and progressively alter the unperturbed limit cycle profile. The parameters here are $c_1 = -5$, $c_2 = 4$, $\sigma = 10^{-5}$ and $K = 4$. Each color designs a specfic node: 1 black, 2 blue, 3 green, 8 red, 9 violet.

5.2.2 Pattern formation

Why is this so important? Let's immagine the following scenario where both solutions exist and are stable. We then seed the following initial conditions $\rho_j(t = 0) = 1$, $\phi_j(t = 0) = 0$ all over the chain. What we expect from a

naive linear stability analysis is that, for small noise amplitudes, the system will remain in the vicinity of the synchronized state, with fluctuations of the order the noise amplitude σ. On the contrary, our analysis reveals that the amplification mechanism here discussed will drive the system to progressively explore larger portions of the available phase space, until it eventually reaches the splay state. This is illustrated in Fig. 5.8, where we show the radial time series of successive nodes. The time series of the first nodes are plotted in red: they remain settled on the synchronized state, the amplification on these first nodes not being strong enough to escape from its basin of attraction. After the 10^{th} node (blue line) fluctuations are now strong enough to escape, and reach the second attractor, settling on the splay state radius $\rho_{\bar{j}+1}$. Nodes to the right converge to successive radii ρ_j with $j > \bar{j}$. The attractor values ρ_j, each represented by a dashed line, is found thanks to the recurence relations (5.3). They are in good agreement with the time series simulations performed by an Euler-Maruyama algorithm. Obviously, this could not be expected from a traditional linear stability analysis.

By direct inspection of Fig. 5.8 one can realize that the transition for the splay to the synchronized state takes place as a sort of zipping mechanism backward in time. The rightmost nodes display larger oscillations and are the first to escape the synchronized state (e.g, violet line in Fig. 5.8). Moreover, it is worth stressing that this process, forward in time, can be viewed as a series of synchronous jumps to consecutive values of ρ_j (e.g., see the green and blue lines in Fig. 5.8). This zipping process continues backward in time up to node $\bar{j}$. A direct consequence of this mechanism is the formation of spatiotemporal

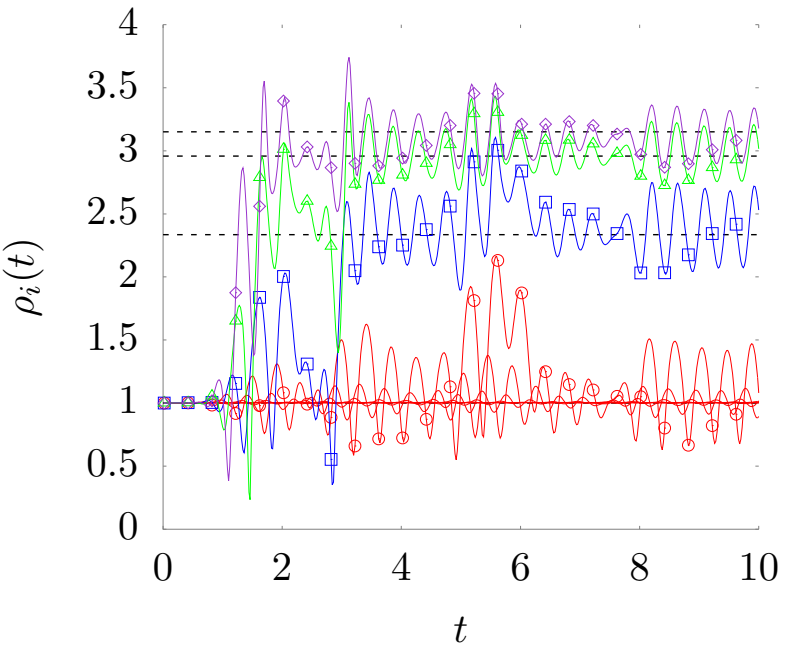

Figure 5.8: Time evolution for selected amplitude $\rho_j(t)$. Each solid line refers to the time series of $\rho_j(t)$. Each color defines a specific group, in red are depicted all the nodes that remain on the synchronized attractor (from the first to the 9^{th} node). The 10^{th} node (blue line) is the first able to escape from the homogenous attractor. The successive nodes (11^{th} green and 12^{th} violet) converge progessively to the asymptotic value ρ_∞ of the splay state. The parameters here are $c_1 = -5$, $c_2 = 4$, $\sigma = 10^{-5}$ and $K = 4$.

patterns [74, 30, 78, 79, 80] as shown in Fig. 5.9. Our system is initially prepared on the synchronized state and exposed to a noise of amplitude $\sigma = 10^{-5}$. After some time we see that the rightmost nodes easily reach the second attractor. However, as we already discussed, the same amplification and modulation mechanism holds on the splay state. The fluctuations therefore keep on being amplified along the chain allowing the rightmost nodes of our system to travel erratically in phase space. This is exemplified by the blurred

part of Fig. 5.9. Here the mechanism of desynchronization is quite obvious, being the combination of two ingredients: noise and non-normality. While noise is needed to inject some dynamics in the otherwise stable limit cycle, the non-normality is essential to amplify these fluctuations. This is what makes the system deviate from the synchronized to the splay state and then enter an erratic dynamics.

5.3 Conclusion

Noise is often unavoidable and, as such, it should be accommodated for in realistic models of complex natural phenomena. A particularly interesting setting is faced when the stochastic perturbation, being it of endogenous or exogenous origin, resonates with the degree of inherent non-normality. This situation, as displayed by the examined system, yields a self-consistent amplification of the noise component at short times. The resulting growth of the perturbation can in fact drive a symmetry breaking instability, for a choice of the parameters that would instead result in a stable deterministic evolution. In order to dig into this question, we have here examined a directed chain of diffusively coupled, Ginzburg-Landau oscillators. Oscillators are shaked by an external fluctuating drive, of arbitrarily small strength. The system is initiated in a region of parameters where the synchronous solution proves stable, under the deterministic scenario. Working in this setting, we provided analytical and numerical evidence for a noise induced instability which follows the self-consistent amplification of the imposed disturbance across

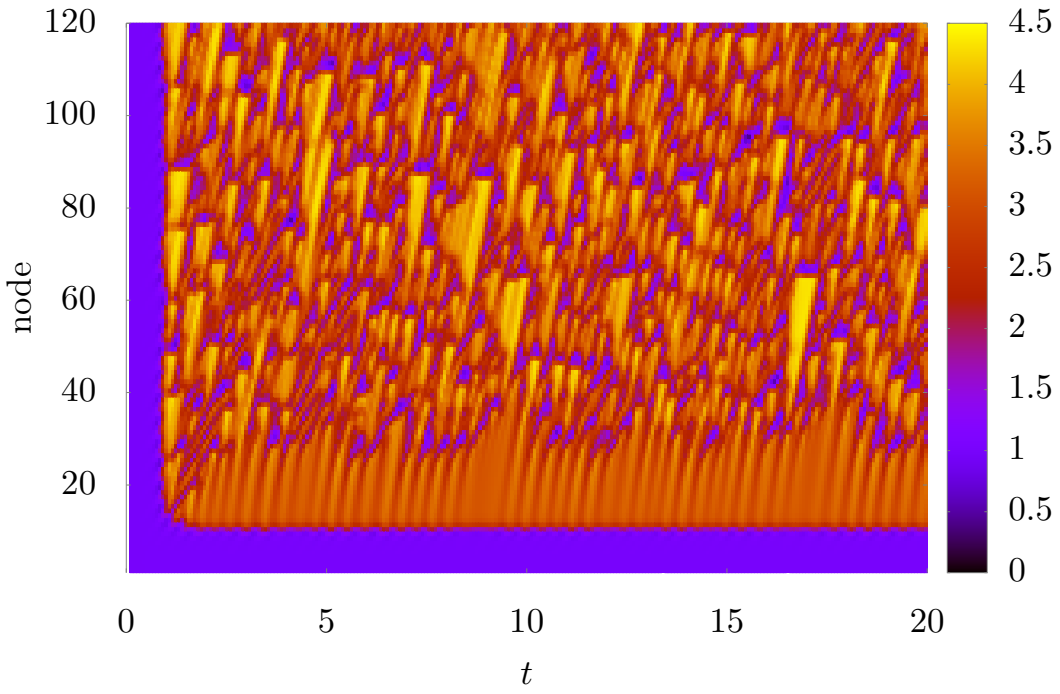

Figure 5.9: Typical spatiotemporal pattern of our system, the 'space' (nodes) is the $y-$axis while time is in abscissa. One can easily recognize the transient in which all the nodes are int the synchronized state. The orange plateau stands for the splay sta e (node $10 \rightarrow 30$) and precedes the blurred region, where system erratically jumps from one state to another. The parameters here are $c_1 = -5$, $c_2 = 4$, $\sigma = 10^{-5}$ and $K = 4$.

the chain. The limit cycles get modulated along the transversal direction: almost regular, radial oscillations are displayed, which gain in potency node after node. When the transversal modulation gets large enough, oscillators escape the basin of attraction of the synchronized solution, visiting a non trivial attractor, that we have characterized. The interaction between the two attractors yield complex emerging patterns reminiscent of the determin-

istic Benjamin-Feir instability. The combination of noise and asymmetric couplings can radically alter the limit cycle dynamics: bistability and associated patterns rise, as the noisy signal is dynamically processed, along the unidirectionally coupled chain. It is worth mentioning that an analogous behavior, due to the forward amplification mechanism, is also expected when the (arbitrarely small) noise is only injected in the leftmost node and not on all degrees of freedom as in our current setup. Indeed the exponential nature of the amplification phenomenon ensures that the leftmost source of perturbation becomes largely predominant. Shifting to the right the leftmost injection point along the chain only changes the pattern layout, thus extending the synchronized region at the expense of the splay state. Throughout this chapter, our system was only subject to unbounded perturbations (Gaussian white noise). However, there is every reason to believe that we would face a significantly similar scenario if we were in the presence of bounded noise. As a matter of fact, the bounded nature of the noise should very quickly fade before the exponential amplification that takes place. Traditional (deterministic) linear stability analysis is unable to grasp the essence of the phenomenon, an observation which we find particularly relevant given the recent reports on the ubiquity of non-normality in real systems, from communication networks to foodwebs [81]. More refined approaches, such as convective Lyapunov exponents [82, 64, 65, 66] should however be able to predict a convective instability at the purely deterministic level. Resilience to synchronization might prove a valuable asset, exploited to oppose the onset of pathological states, as e.g. epileptic seizures in brain dynamics. Future investigations are planned to shed light onto these families of noise–instigated

instabilities, assisted by the non-normal topology of the underlying support, beyond the simplistic case study here considered.

At the conclusion of this work, a draft of an article was recently submitted: *Desynchronization and pattern formation in a noisy feedforward oscillators network*, Zankoc C., Ginelli F., Fanelli D., and Livi R., arXiv:1810.01933

Chapter 6

Conclusion

I would first like to recall what motivated it. First and foremost, noise is ubiquitous. Most of physical systems are subject to fluctuations stemming either from interactions with the outside world or being intrinsic to the system itself. These fluctuations can play very different roles depending on the system under study. In many situations they are key ingredient if we want to understand properly the dynamics. Throughout this thesis, I provided new examples for the role of noise. I systematically started my studies by determining the dynamics of systems in absence of noise. This enabled me to compare with the situation where noise is present. Subsequently, I used all the tools at my disposal to get a better understanding of the noise's modus operandi. In parallel to rigorous analytical calculations, I relied on numerical simulations to verify my results. The main findings of this work are the following.

In the second chapter, I used the Wilson-Cowan model, which describes

the minimal dynamics of two interacting populations of excitatory and inhibitory neurons. I put it in a region where it displays bistability because this is a regime of particular interest for neurophysicists since it has been experimentally observed that cerebral cortex displays similar behavior during deep sleep, seemingly alternating between high and low level of neural activity. Fluctuations are mandatory to generate such alternation in the WC model. If absent the system would lock itself in one of the basins of attraction.

My first objective was to derive a mesoscopic representation of the dynamics to expound the contribution of endogenous fluctuations. This yielded two coupled non-linear Langevin equations with mulitplicative noise. Regions of low and high activity could be determined by computation of the stationary probability distributions of the species at stake. While this can always be achieved by numerical simulations via the well-known Gillespie algorithm, it is more challenging to obtain analytical solutions due to the non-potential nature of the system. I developed a new procedure which starts from a master-slave approximation, where the action of the excitatory population over the inhibitory one is neglected. This limits the bistable behavior to only a single species and therefore allows for an analytical access to the stationary probability distribution. Using a recursive pertubative scheme, I could progressively restore the retroaction of inhibitors over excitators without ceasing to keep track of the statistics of the system. In parallel to this technical result, I observed that this endogeneous noise can shift the bifurcation point beyond which the system exhibits stability. This induces an extension of the bistable behavior region as compared to the purely thermodynamic limit dynamics [83].

Synchronization has been a topic of growing interest. Synchronization is the backbone of most of collective dynamics phenomena which are omnipresent in nature. Coupled phase oscillators models can be employed to investigate on such feature, and, although they can be perturbed by the injection of noise.

I introduced a reduced version of the Wilson-Cowan exhibiting quasi-cycles. When two of these oscillators are diffusively and symmetrically coupled two of these oscillators one can study the coherence of their signals with the help of the power spectral distribution matrix. Interestingly, I found that they organized themselves: their low frequency oscillations coordinated in anti-phase, while the high frequency ones were in-phase. I repeated the same analysis on larger and more complex structures. More, I observed the formation of time-varying patterns sustained by noise. These patterns respect the anti-phase locking for contiguous node that we observed previously: This leads to frustration problems when the symmetries and the topology of the network come into conflict with this prerequisite. These *noise sustained patterns* illustrate very well the very intringuing interplay between noise and the network topology [84].

I kept on examining how the mix between noise and topology may lead to unexpected effects. To this end, I devised a set-up where the same stochastic oscillators were set on an feedforward network. Numerical and analytical analysis showed that the signal got modulated and amplified along the chain, becoming quickly more and more similar to limit cycle oscillations as the node number increased. As expected from its convective nature, the amplification is exponential. Any perturbation appeared able to drive the system out of its

fixed point dynamics in the deterministic limit to macroscopic oscillations. The network acted as a pacemaker and could be employed for a large gallery of applications [85].

An analogous investigation took place in the fifth chapter where the stochastic oscillators were replaced by Ginzburg-Landau oscillators perturbed with external noise. I found the same phenomenon of amplification and modulation for the perturbations normal to the limit cycle, leading to desynchronization and pattern formation. Again, noise inserted in the system leads to dramatic and unexpected effects of macroscopic magnitude irrespective of its amplitude.

Taken together, these studies demonstrated an important underlying idea, namely that *endogeneous* noise can have a qualitative effect on the macroscopic dynamics of systems composed by a large but finite number of elements. In fact, many of my results also apply to the effect of a (arbitrarily small) *exogeneous* noise.

The qualitative effects that I demonstrated show that the deterministic dynamics of typical mean-field level descriptions may be qualitatively different from the "real" behavior of the system when the (unavoidable) effects of noise are considered.

These observations may indeed prove to be crucial in many different contexts, mainly (but not exclusively) of biological relevance, ranging from neuroscences to population dynamics and system biology.

Appendices

Appendix A

Gillespie algorithm

Chemical kinetics has traditionally been analyzed using a mathematical formalism in which continuous variables evolve deterministically. For systems of test-tube size or larger, this seems reasonable. But, as we already know, if some reactants of the system have a population which is not too many order of magnitude larger than one, which is often the case for biological systems, discreteness and stochasticity can play a crucial role. The Gillespie algorithm, which belongs to the Monte-Carlo algorithm class aims at taking into account these features. It has been designed by the mathematician J.L. Doob [86] but popularized by D. Gillespie in 1977 in an article [11] where he used it to simulate chemical systems. It is indeed a very effective tool to generate a statistically correct trajectory of a stochastic system formulated in terms of rate equations. Imagine we have N chemical species denoted $S_1, \ldots, S_N$ interacting through M distinct reaction channels $R_1, \ldots, R_M$. We want to estimate the state vector $\mathbf{X}(t) = (X_1(t), \ldots, X_N(t))$ where each X_i stands for the number of molecules for the species S_i. Each chemical R_j channel is

characterized by two quantities :

- the state change vector $\nu_j = (\nu_{1j}, \ldots, \nu_{Nj})$ where ν_{ij} denotes the change in the S_i population when reaction R_j occur, $S_i \to S_i + \nu_{ij}$.
- its propensity function $a_j(x)$ where $a_j(x)\mathrm{d}t$ is the probability, given $X(t) = x$, that reaction R_j will occur in the next infinetesimal time $[t; t + \mathrm{d}t]$.

We know that such systems obey a Master equation

$$\frac{\partial P(x,t|x_0,t_0)}{\partial t} = \sum_{j=1}^{M} \left[a_j(x-\nu_j)P(x-\nu_j,t|x_0,t_0) - a_j(x,t)P(x,t|x_0,t_0)\right] \tag{A.1}$$

where $P(x,t|x_0,t_0)$ is a conditional probability of finding our system in state x at time t given $X(t_0) = x_0$. The main idea behind the Gillespie algorithm is to rather consider the *reaction probability function* $p(\tau, j|x,t)$ such that; $p(\tau, j|x,t)\mathrm{d}\tau$ is the probability, given $X(t) = x$, that the next reaction in the system will occur in the infinitesimal time interval $[t+\tau; t+\tau+\mathrm{d}\tau]$ and will be a R_j reaction. This is equal to

$$p(\tau, j|x,t) = P_0(\tau)a_j(x)\mathrm{d}\tau \tag{A.2}$$

where $P_0(\tau)$ is the probability that no reaction will occur in the time interval $[t; t+\tau]$ and $a_j(x)$ the probability that the reaction R_j will occur in the time interval $[t+\tau; t+\tau+\mathrm{d}\tau]$. P_0 can be easily computed using the propensity

functions $a_j(x)$ since

$$P_0(\tau' + \mathrm{d}\tau') = P_0(\tau') \left[1 - \sum_{j=1}^{M} a_j(x)\mathrm{d}\tau' \right] \tag{A.3}$$

we can conclude that

$$P_0(\tau) = \exp \left[- \sum_{j=1}^{M} a_j(x)\tau \right] \tag{A.4}$$

and therefore

$$p(\tau, j|x, t) = \begin{cases} a_j(x) \exp(-a_0(x)\tau) & 0 \leq \tau < \infty \\ 0 & \text{otherwise} \end{cases} \tag{A.5}$$

where : $a_0(x) = \sum_{j=1}^{N} a_j(x)$. We now need to generate a random pair (τ, j) from the set of random pairs whose probability density function is $p(\tau, j)$.

$$\begin{pmatrix} r_1 \\ r_2 \end{pmatrix} \rightarrow \begin{pmatrix} \tau \\ j \end{pmatrix}$$

where $r_1, r_2 \in [0; 1]$ are random number. This can be achieved this way :

- first generating the time $\tau = \frac{1}{a_0} \ln \left(\frac{1}{r_1} \right)$
- selecting an integer j such that

$$\sum_{k=1}^{j-1} a_k < r_2 a_0 \leq \sum_{k=1}^{j} a_k$$

The first equation generates a time τ according to the probability distribution $P_1(\tau) = a_0 \exp(-a_0\tau)$, the second generates j which obeys to $P_2(j) = a_j/a_0$. We can now compute $p(\tau, j)$ since

$$p(\tau, j) = P_1(\tau)P_2(j) \tag{A.6}$$

The implementation of the algorithm is rather simple:

0 - Initialize the time $t = 0$ and the system's state $X(0) = x_0$

1 - We evalute all the propensity functions $a_j(x)$ and their sum $a_0(x)$

2 - We generate τ and j using previous equations

3 - Effect the next reaction by setting $t \to t + \tau$ and by updating the state vector $X \to X + \nu$

4 - Return to step 1 or end the simulation.

As an example, for the CW model obeying the chemical rate equations (3.1) we would have

$$\begin{array}{lcccl} R_1: & \emptyset & \xrightarrow{f[s_x]} & X & a_1 = f[s_X] \\ R_2: & X & \xrightarrow{1} & \emptyset & a_2 = x \\ R_3: & \emptyset & \xrightarrow{f[s_y]} & Y & a_3 = f[s_Y] \\ R_4: & Y & \xrightarrow{1} & \emptyset & a_4 = y \end{array}$$

We can then access to single realizations of our stochastic process $\{X(t)\}$, compute the average quantities by repeating the algorithm for different random number chains, etc... Contrary to many other algorithms made to simulate stochastic systems which approximate the time increment τ, the Gillespie

algorithm does not. Therefore, it provides an *exact* solution of the problem. Nevertheless, it suffers from its slowness especially when the number of reactants start being important.

Appendix B

Itô and Stratonovich prescriptions

This appendix is here to present a proper treatment of stochastic differential equations. Let's imagine we have the following non-linear Langevin equation

$$\frac{\mathrm{d}x}{\mathrm{d}t} = f(x) + g(x)\eta(t) \tag{B.1}$$

where $\eta(t)$ is a Gaussian white noise with zero mean and correlator $\langle \eta(t)\eta(t')\rangle = \delta(t-t')$, f and g two given functions. The first problem arising is that $\eta(t)$ is ill-defined [87], it is a singular object just as much as the δ-distribution which enters in its definition. To circumvent this first obstacle we often rewrite equation (B.1)

$$\mathrm{d}x = f(x)\mathrm{d}t + g(x)\mathrm{d}W(t) \tag{B.2}$$

where $W(t)$ is called a *Wiener process* and read $W(t) = \int_0^t \eta(t')\mathrm{d}t'$. With W we now deal with a new stochastic process continuous in time (but not differentiable). But the main issue remains, when the function g depends on x, then equation (B.2) together with an initial condition $x(0) = x_0$ does not define a unique stochastic process. Indeed, if we decide to integrate (B.2), we still need to chose a definition for the integration of $\int_0^t g(x)\mathrm{d}W(t')$ because it is not uniquely defined when averaged over the stochastic process. The easiest way to do this is through a Taylor expansion. In the simplest non trivial case where $f(x) = 0$ and $g(x) \neq 0$, we have

$$x(t) - x_0 = \int_0^t g(x(t'))\mathrm{d}W(t') \approx \int_0^t \mathrm{d}W(t') \left[g(x_0) + g'(x_0)(x(t') - x_0)\right] \tag{B.3}$$

The lowest order reads $x(t) - x(0) = g(x(t_0))W(t)$ while, if $g'(x) \neq 0$ an integral of the form $\int W\mathrm{d}W$ appears at the next order. We can use a Riemanian approach to estimate the average (over stochastic process) of this integral, it leads to

$$\langle \int_0^t W\mathrm{d}W \rangle = \langle \lim_{n\to\infty} \sum_{i=1}^{n} W(t_i*) \left[W(t_{i+1}) - W(t_i)\right] \rangle \tag{B.4}$$

where the support of t has been subdivided into an ordered sequence $t_0 = 0 < t_i < t_N = t$ and where $t_i* = t_i + \alpha(t_{i+1} - t_i)$ with $\alpha \in [0:1]$ so that $t_i < t_i* < t_{i+1}$. Knowing that $\langle W(s)W(u) \rangle = \min(t, u)$, we easily end up with

$$\langle \lim_{n\to\infty} \sum_{i=1}^{n} W(t_i*) \left[W(t_{i+1}) - W(t_i)\right] \rangle = \alpha t \tag{B.5}$$

Although the choice of α is completely arbitrary (as long as $\alpha \in [0:1]$), only two values are commonly found: $\alpha = 0$ for the Itô prescription, and $\alpha = \frac{1}{2}$

for the Stratonovich prescription.

More important, we can convert the Langevin equation (B.1) into a Fokker-Planck equation of the form

$$\frac{\partial P(x,t)}{\partial t} = \frac{\partial}{\partial x}\left[-f(x) - \alpha g'(x)g(x) + \frac{1}{2}\frac{\partial}{\partial x}g^2(x)\right]P(x,t) \tag{B.6}$$

which depends explicitly on α, meaning that if the noise is multiplicative, $g'(x) \neq 0$, Itô and Stratonovich prescriptions lead to different probability distribution for x and therefore describe different stochastic process. But since everything here is a matter of definition, it would be grotesque to argue about their being right or wrong [88]. The Kramers-Moyal expansion that we have employed in first chapter, illustrates perfectly this point because it drives to a Fokker-Planck equation for the fluctuations where this controversy never enters. This also raises a very intriguing question about Langevin interpretation in which we assume that the drift function f would be a sort of macroscopic force independent of system's internal fluctuations even when there is no good reason to assume that [35, 89].

From a technical point of view, both interpretations have their advantages. For example, one of the merit of Itô prescription is that it simplifies considerably the computation of average quantities since $\langle \int_0^t g(x)\mathrm{d}W(t')\rangle = 0$. We then say that the function g is *non-anticipative* because it depends on nothing that occurs after time t [90]. However, the inconvenient of the Itô prescription is that, if we wish to apply non-linear transformation to our Langevin equation, we'll need to respect rules of calculus that differ from the traditional ones. On the contrary, with the Stratonovich prescription the traditional rules of calculus remain valid. They are not employed in the

same context. If we are dealing with a system where white noise is used to approximate a continuously fluctuating noise with finite memory (much shorter than dynamical timescales) then the appropriate representation is the Stratonovich one. At the contrary, if the white noise plays the role of a set of discrete pulses with finite separation to which system responds, or if we try to employ a continuous representation for a discrete system by means of SDEs, then the Itó representation is more suitable. The Stratonovitch prescription is mostly used in physics to describe physical processes continuous in time while the Itô convention is more suitable for discrete time processes (finance, economics, ...). Therefore, the Itó prescription goes hand in hand with the Gillespie algorithm which is a discrete time algorithm. This constitutes the main reason behind our utilization of this convention throughout this thesis.

We conclude by saying that expression (B.1) is the pre-equation that needs intepretation rule to be turned into a real equation. After having chosed which prescription we wish to employ, we need to respect its specific rules of calculus and intepretate our final equation according to this interpretation.

Appendix C

Computing the moments of the Gaussian multivariate distribution Π

Once again we are going to employ the linear noise approximation in order to study the dynamics of the probability distribution $\Pi(\boldsymbol{\zeta}, \tau)$ of fluctuations. It can be easily showen that $\Pi(\boldsymbol{\zeta}, \tau)$ obeys the following Fokker-Planck equation

$$\frac{\partial}{\partial \tau}\Pi = -\sum_{i=1}^{2\Omega} \frac{\partial}{\partial \zeta_i}\left[(J\zeta)_i \Pi\right] + \frac{1}{2}\sum_{i,j=1}^{2\Omega} \frac{\partial^2}{\partial \zeta_i \partial \zeta_j}\mathcal{B}_{ij}\Pi \tag{C.1}$$

where J stands for the Jacobian of the system and $\mathcal{B}$ for its diffusion matrix. We shall here derive the dynamical equations that control the evolution of the moments of the distribution Π. Focus on the first moment, by multiplying equation (C.1) by ζ_k and integrating over $\boldsymbol{\zeta}$. The left hand side of equation

yields:

$$\int d\boldsymbol{\zeta}\zeta_k \frac{\partial}{\partial\tau}\Pi = \int d\boldsymbol{\zeta}\frac{\partial}{\partial\tau}\Pi\zeta_k = \frac{d}{d\tau}\int d\boldsymbol{\zeta}\zeta_k\Pi = \frac{d}{d\tau} < \zeta_k > \tag{C.2}$$

The right hand side can be split into two parts. Under mild assumptions for Π, the drift term returns:

$$-\sum_{i=1}^{2\Omega}\int d\boldsymbol{\zeta}\zeta_k \frac{\partial}{\partial\zeta_i}\left[(J\boldsymbol{\zeta})_i\Pi\right] \tag{C.3}$$

The contribution $i = k$ amounts to:

$$\begin{aligned}\int \mathrm{d}\boldsymbol{\zeta}\zeta_k \tfrac{\partial}{\partial\zeta_k}\left[(J\boldsymbol{\zeta})_k\Pi\right] &= \int\prod_{j\neq k} d\zeta_j \int d\zeta_k\zeta_k \tfrac{\partial}{\partial\zeta_k}\left[(J\boldsymbol{\zeta})_k\Pi\right] \\ &= -\int\prod_{j\neq k} d\zeta_j \int d\zeta_k\left[(J\boldsymbol{\zeta})_k\Pi\right] \\ &= -\int d\boldsymbol{\zeta}\left[(J\boldsymbol{\zeta})_k\Pi\right] \\ &= -\langle(J\boldsymbol{\zeta})_k\rangle\end{aligned} \tag{C.4}$$

while the terms with $i \neq k$ give no contributions. In fact:

$$\int\prod_{j\neq k,i} d\zeta_j \int d\zeta_k\zeta_k \int d\zeta_i \frac{\partial}{\partial\zeta_i}\left[(J\boldsymbol{\zeta})_i\Pi\right] = 0 \tag{C.5}$$

It is then straightforward to conclude that the diffusion terms returns no contributions, because Π decays fast enough at the boundaries. Summing up, we therefore obtain the linear equations:

$$\frac{d}{d\tau}\langle\zeta_k\rangle = <(J\boldsymbol{\zeta})_k\rangle = \sum_{j=1}^{2\Omega} J_{kj}\langle\zeta_j\rangle \tag{C.6}$$

The unique stationary (stable) solution is therefore $\langle\zeta_k\rangle = 0 \quad \forall k$.

An identical procedure can be followed to evaluate the second moments of the distribution, namely $< \zeta_l \zeta_m >$. To this end we multiply equation (C.1) by $\zeta_l \zeta_m$ and integrate over $\boldsymbol{\zeta}$. In analogy with the above, the left hand side of the equation returns:

$$\int \mathrm{d}\boldsymbol{\zeta} \zeta_l \zeta_m \frac{\partial}{\partial \tau} \Pi = \frac{d}{d\tau} \langle \zeta_l \zeta_m \rangle \tag{C.7}$$

When it comes to the drift term, we shall focus first on the diagonal, $l = m$, contributions:

$$-\sum_{i=1}^{2\Omega} \int d\boldsymbol{\zeta} \zeta_l^2 \frac{\partial}{\partial \zeta_i} \left[(J\boldsymbol{\zeta})_i \Pi \right] \tag{C.8}$$

For $i = l$, we get:

$$\begin{aligned} \int \mathrm{d}\boldsymbol{\zeta} \zeta_l^2 \tfrac{\partial}{\partial \zeta_l} \left[(J\boldsymbol{\zeta})_l \Pi \right] &= \int \textstyle\prod_{j \neq l} d\zeta_j \int d\zeta_l \zeta_l^2 \tfrac{\partial}{\partial \zeta_l} \left[(J\boldsymbol{\zeta})_l \Pi \right] \\ &= -2 \int \textstyle\prod_{j \neq l} d\zeta_j \int d\zeta_l \zeta_l (J\boldsymbol{\zeta})_l \Pi \\ &= -2 \langle \zeta_l (J\boldsymbol{\zeta})_l \rangle \end{aligned} \tag{C.9}$$

while for $i \neq l$ one finds:

$$\begin{aligned} \int \mathrm{d}\boldsymbol{\zeta} \zeta_l^2 \tfrac{\partial}{\partial \zeta_i} \left[(J\boldsymbol{\zeta})_i \Pi \right] &= \int \textstyle\prod_{j \neq l,i} d\zeta_j \int d\zeta_l \zeta_l^2 \int d\zeta_i \tfrac{\partial}{\partial \zeta_i} \left[(J\boldsymbol{\zeta})_i \Pi \right] \\ &= 0 \end{aligned} \tag{C.10}$$

Consider now the contribution of the drift to the off diagonal elements ($l \neq m$), namely:

$$-\sum_{i=1}^{2\Omega} \int d\boldsymbol{\zeta} \zeta_l \zeta_m \frac{\partial}{\partial \zeta_i} \left[(J\boldsymbol{\zeta})_i \Pi \right] \tag{C.11}$$

For $i = l$, one gets:

$$\begin{aligned}
&\int \prod_{j\neq l,m} d\zeta_j \int d\zeta_m \zeta_m \int d\zeta_l \zeta_l \frac{\partial}{\partial \zeta_l}\big[(J\boldsymbol{\zeta})_l \Pi\big] \\
&\quad = -\int \prod_{j\neq l,m} d\zeta_j \int d\zeta_m \zeta_m \int d\zeta_l \big[(J\boldsymbol{\zeta})_l \Pi\big] \\
&\quad = -\langle \zeta_m (J\boldsymbol{\zeta})_l \rangle
\end{aligned} \tag{C.12}$$

The other case of interest, $i = m$, is easy to treat, as it amounts to swapping l and m. Finally, for $i \neq l, m$ the drift term returns a null contribution:

$$\int \prod_{j\neq m,l,i} d\zeta_j \int d\zeta_m \zeta_m \int d\zeta_l \zeta_l \int d\zeta_i \frac{\partial}{\partial \zeta_i}\big[(J\boldsymbol{\zeta})_i \Pi\big] = 0 \tag{C.13}$$

Let us now turn to considering the contribution of the diffusion terms in the Fokker-Planck equation. Since $\boldsymbol{\mathcal{B}}$ is diagonal, a non trivial contribution is solely found for $l = m$:

$$\frac{1}{2}\sum_{i=1}^{2\Omega} \int d\boldsymbol{\zeta} \zeta_l^2 \frac{\partial^2}{\partial \zeta_i^2} \mathcal{B}_{ii} \Pi \tag{C.14}$$

For $i = l$, we have:

$$\begin{aligned}
\tfrac{1}{2}\textstyle\int \prod_{j\neq l} d\zeta_j \int d\zeta_l \zeta_l^2 \frac{\partial^2}{\partial \zeta_l^2} \mathcal{B}_{ll} \Pi &= -2\tfrac{1}{2} \textstyle\int \prod_{j\neq l} d\zeta_j \int d\zeta_l \zeta_l \frac{\partial}{\partial \zeta_l} \mathcal{B}_{ll} \Pi \\
&= \textstyle\int \prod_{j\neq l} d\zeta_j \int d\zeta_l \mathcal{B}_{ll} \Pi \\
&= \mathcal{B}_{ll}
\end{aligned} \tag{C.15}$$

where use has been made of the condition of normalization for the distribution

Π. The case $i \neq l$ yields no contribution as:

$$\frac{1}{2}\int \prod_{j\neq l,i} d\zeta_j \int d\zeta_l \zeta_l^2 \int d\zeta_i \frac{\partial^2}{\partial \zeta_i^2} \mathcal{B}_{ii}\Pi = 0 \tag{C.16}$$

Collecting all terms together we end up with the equations for the second moments reported in the main body of the thesis.

Appendix D

Analytical estimate for the leftmost boundary of the amplification domain

Computing the moments of the multivariate Gaussian that characterizes the stationary distribution of fluctuations under the linear noise approximation, imply solving a $2\Omega \times 2\Omega$ problem. To gain analytical insight into the problem (with reference to the setting $\gamma_i = 1$), one can operate a drastic simplification by solely accounting for nearest neighbors correlations. In doing so, one obtains a 7×7 linear system, which we do not write here explicitly because it involves lengthy expressions. Due to the structure of the problem, the 7×7 system rigorously reduces to an effective map, from a given node to the next one, for the reference quantities $\boldsymbol{w}_i = (< \xi_i^2 >, < \eta_i^2 >, < \xi_i \eta_i >)$. More

concretely, one can recast the problem in the form:

$$\boldsymbol{w}_{i+1} = \boldsymbol{A}\boldsymbol{w}_i + \boldsymbol{r} \tag{D.1}$$

where $\boldsymbol{A}$ (not given here explicitly) is non diagonalizable, it has rank 2 and eigenvalues $0, \lambda$, with:

$$\lambda = \frac{-2\,D^3\,r^3 + D^2\,r^4 + 80\,D^2\,r^2}{128\,D^2\,r^2 - 128\,D\,r^3 - 2048\,D\,r + 32\,r^4 + 1024\,r^2 + 8192} \tag{D.2}$$

To solve the problem one can reduce $\boldsymbol{A}$ to a Jordan normal form $\boldsymbol{\mathcal{A}}$. It can be in fact shown that a matrix $\boldsymbol{P}$ exists such that $\boldsymbol{\mathcal{A}} = \boldsymbol{P}^{-1}\boldsymbol{A}\boldsymbol{P}$

By operating the change of variables $\boldsymbol{q}_i = \boldsymbol{P}^{-1}\boldsymbol{w}_i$ and defining $\boldsymbol{R} = \boldsymbol{P}^{-1}\boldsymbol{r}$ one gets:

$$\boldsymbol{q}_{i+1} = \boldsymbol{\mathcal{A}}\boldsymbol{q}_i + \boldsymbol{R} \tag{D.3}$$

that it can be shown to yield:

$$\begin{cases} q_{i+1}^{(1)} = q_i^{(2)} + R^{(1)} \\ q_{i+1}^{(2)} = R^{(2)} \\ q_{i+1}^{(3)} = \lambda q_i^{(3)} + R^{(3)} \end{cases} \tag{D.4}$$

where $\boldsymbol{q}_i \equiv (q_i^{(1)}, q_i^{(2)}, q_i^{(3)})$ and $\boldsymbol{R} \equiv (R^{(1)}, R^{(2)}, R^{(3)})$. Solving the above

system and going back to the original variables, one eventually gets:

$$\begin{aligned}
\langle \xi_i^2 \rangle &= P_{13}\big(q_3(0) + \tfrac{R^{(3)}}{\lambda-1}\big)\lambda^i + \\
&\quad P_{11}(R^{(1)} + R^{(2)}) + P_{12}R^{(2)} - P_{13}\tfrac{R^{(3)}}{\lambda-1} \\
\langle \eta_i^2 \rangle &= P_{23}\big(q_3(0) + \tfrac{R^{(3)}}{\lambda-1}\big)\lambda^i + \\
&\quad + P_{21}(R^{(1)} + R^{(2)}) + P_{22}R^{(2)} - P_{23}\tfrac{R^{(3)}}{\lambda-1} \\
\langle \eta_n \xi_i \rangle &= P_{33}\big(q_3(0) + \tfrac{R^{(3)}}{\lambda-1}\big)\lambda^i + \\
&\quad P_{31}(R^{(1)} + R^{(2)}) + P_{32}R^{(2)} - P_{33}\tfrac{R^{(3)}}{\lambda-1}
\end{aligned} \tag{D.5}$$

The amplification is hence lost if $|\lambda| \leq 1$. The leftmost solid (white) line in Figure 4.5 in the main body of the thesis corresponds to the limiting condition $\lambda = 1$. The boundary of the domain where the amplification takes place is adequately reproduced, an observation that supports a posteriori the validity of the approximations involved in the analysis.

Appendix E

A consistent thermodynamic interpretation.

Given the probability density $P(\boldsymbol{v}, \tau)$ that obeys to the Fokker-Planck equation associated to Langevin equations (4.2) we define the entropy $S(\tau)$ as

$$S(\tau) = -\int P(\boldsymbol{v}, \tau) \ln P(\boldsymbol{v}, \tau) d\boldsymbol{v} \tag{E.1}$$

By deriving with respect to time τ the previous equation, one gets:

$$\frac{dS}{d\tau} = -\int \frac{\partial P}{\partial \tau} \big(\ln P + 1 \big) d\boldsymbol{v} = \int \sum_i \frac{\partial I_i}{\partial v_i} \big(\ln P + 1 \big) d\boldsymbol{v} \tag{E.2}$$

and, integrating by parts:

$$\frac{dS}{d\tau} = -\sum_i \int I_i \frac{\partial}{\partial v_i} \ln P d\boldsymbol{v} \tag{E.3}$$

By making use of the definition of the current $\boldsymbol{I}$, see main body of the paper, we write:

$$\frac{\partial}{\partial v_i}\ln P = \frac{2}{B_{ii}}A_i - \frac{2}{B_{ii}}\frac{I_i}{P} \tag{E.4}$$

and finally:

$$\frac{dS}{d\tau} = \Pi_S - \Phi_S \tag{E.5}$$

where

$$\begin{aligned} \Pi_S &= \textstyle\sum_i \frac{2}{B_{ii}} \int \frac{I_i^2(\boldsymbol{v},\tau)}{P(\boldsymbol{v},\tau)} \\ \Phi_S &= \textstyle\sum_i \frac{2}{B_{ii}} \int A_i(\boldsymbol{v}) I_i(\boldsymbol{v},\tau) d\boldsymbol{v} \end{aligned} \tag{E.6}$$

Π_S is positive definite and can be interpreted as the production rate of entropy due to the non-conservative forces A_i. Φ_S can take in principle any sign. When $\Phi_S > 0$, the entropy flows from the system to the environment. At equilibrium $I_i = 0$, which implies $\Pi_S = \Phi_S = 0$. A non trivial stationary solution exists which corresponds to setting $\Pi_S = \Phi_S \neq 0$. This is equivalent to imposing $\sum \frac{\partial}{\partial v_i} I_i = 0$, the condition of Fokker-Planck stationarity. The solution of the Fokker-Planck equation is hence interpreted as a dynamical balance between two opposing entropy fluxes. To quantify the entropy production Π_S, we can therefore estimate the antagonist contribution Φ_S.

By making use of the definition of the current, an performing an integration by parts, one gets:

$$\begin{aligned} \Phi_S &= \sum_i \frac{2}{B_{ii}} \int A_i I_i d\boldsymbol{v} = \sum_i \frac{2}{B_{ii}} \int \big(A_i^2 P - \frac{B_{ii}}{2} A_i \frac{\partial}{\partial v_i} P\big) \\ &= \sum_i \frac{2}{B_{ii}} \int \big(A_i^2 P + \frac{B_{ii}}{2} P \frac{\partial}{\partial v_i} A_i\big) \\ &= \sum_i \big(\frac{2}{B_{ii}} < A_i^2 > + < \frac{\partial}{\partial v_i} A_i > \big) \end{aligned} \tag{E.7}$$

The above formula con be employed to determine the (non-linear) entropy production rate Π_S $(= \Phi_S)$, displayed by the system in stationary conditions. To gain analytical insight we can proceed with a direct estimate of Π_S (and hence Φ_S) that builds on the linear noise approximation. In this case we can write:

$$\Phi_S = \sum_i \left(\frac{2}{\mathcal{B}_{ii}} < f_i^2 > + < \frac{\partial}{\partial \zeta_i} f_i > \right) \tag{E.8}$$

where the non conservative force is now $f_i = (J\zeta)_i$. Recalling that:

$$\sum_i < \frac{\partial}{\partial \zeta_i} f_i > = \sum_i < \sum_j J_{ij} \frac{\partial \zeta_j}{\partial \zeta_i} > = \sum_i < J_{ii} > = Tr(J) \tag{E.9}$$

we can write:

$$\Phi_S = \sum_{i,j,k} \frac{2}{\mathcal{B}_{ii}} J_{ij} J_{ik} < \zeta_j \zeta_k > + Tr(J) \tag{E.10}$$

Define then the correlation matrix $C_{ij} =< \zeta_i \zeta_j >$ and write

$$\begin{aligned} \Phi_S &= 2 \sum_{i,j,k} \frac{1}{\mathcal{B}_{ii}} J_{ij} J_{ik} C_{jk} + Tr(J) = \\ &= 2 \sum_i \frac{1}{\mathcal{B}_{ii}} (JCJ^t)_{ii} + Tr(J) \end{aligned} \tag{E.11}$$

In Figure 3.7 the entropy production rate Π_S $(= \Phi_S$, as given by formula (E.11)) is plotted (solid line) versus the lattice node, an indirect measure of the lattice length. As expected, Π_S grows exponentially. Symbols refer instead to the a direct numerical characterization of Π_S, based on relation (E.7). Non-linear effects induce a cross-over towards a non exponential growth for the measured entropy production rate. A cross-over towards a non exponential regime is eventually observed when non-linearities become prominent, in

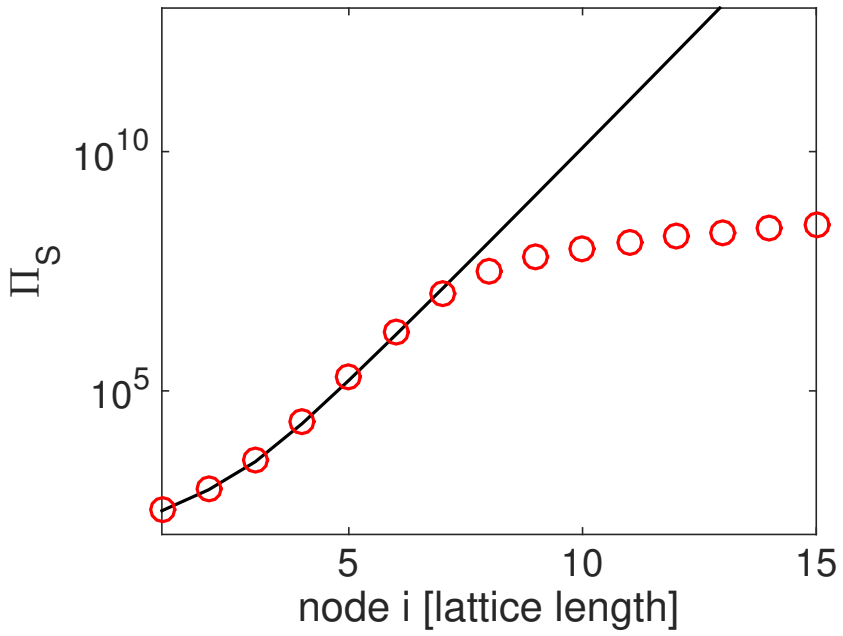

Figure E.1: Π_S is plotted (solid line) versus the lattice node. The solid line refers to the analytical estimate based on linear noise approximation, see equation (E.11)). Symbols refer instead to the numerical estimate based on the fully non-linear relation (E.7).

complete agreement with the insight gained under a purely dynamical angle.

Appendix F

Linear stability analysis

In this appendix we provide details on the stability analysis for synchronous and splay states carried out in Chapter 5.Consider small perturbations $\delta\rho_j(t) \ll 1$ and $\delta\theta_j(t) \ll 1$ of the limit cycle solutions, $W_j = (\rho_j + \delta\rho_j)e^{i(\theta_j+\delta\theta_j)}$. Linearizing we obtain to first order in the perturbations

$$\delta\dot{\rho}_1 = -2\delta\rho_1 \tag{F.1}$$

$$\delta\dot{\theta}_1 = -2c_2\delta\rho_1 \tag{F.2}$$

and for $j > 1$

$$\begin{aligned}
\delta\dot{\rho}_j &= \delta\rho_j\left[1-3\rho_j^2-K\right]+\delta\rho_{j-1}Kf(\phi_j) \\
&\quad +\left(\delta\theta_j-\delta\theta_{j-1}\right)K\rho_{j-1}g(\phi_j) \qquad \text{(F.3)} \\
\delta\dot{\theta}_j &= \delta\rho_j\left[-2c_2\rho_j+K\frac{\rho_{j-1}}{\rho_j}g(\phi_j)\right]+\delta\rho_{j-1}\frac{K}{\rho_j}g(\phi_j) \\
&\quad -\left(\delta\theta_j-\delta\theta_{j-1}\right)K\frac{\rho_{j-1}}{\rho_j}f(\phi_j) \qquad \text{(F.4)}
\end{aligned}$$

where the ρ_j and ϕ_j need to be evaluated on either the synchronized or the splay state attractor. Obviously zeroth order terms stemming from the linearization procedure vanish by construction when evaluated on these two attractors.

Rewriting the linearized equations in a matrix form highlights their simple block structure, due to the unidirectional input from one node to the next. We introduce the 2Ω dimensional perturbation vector $\delta\mathbf{v} \equiv (\delta\rho_1, \delta\theta_1, \delta\rho_2, \delta\theta_2, \ldots, \delta\rho_\Omega, \delta\theta_\Omega)^T$ and write

$$\delta\dot{\mathbf{v}} = \mathbf{J}\,\delta\mathbf{v} \qquad \text{(F.5)}$$

where the Jacobian $\mathbf{J}$ is a $2\Omega \times 2\Omega$ lower tridiagonal block matrix, composed of 2×2 blocks that describe the in-node linearized dynamics ($\mathbf{A}$ matrices in the following) or the (linearized) interaction with the previous node ($\mathbf{B}$ matrices).

For instance, in the case of the synchronized state one has

$$\mathbf{J}_H = \begin{pmatrix} \mathbf{A}_1 & \mathbf{0} & \mathbf{0} & \mathbf{0} & \dots \\ \mathbf{B}_2 & \mathbf{A}_2 & \mathbf{0} & \mathbf{0} & \dots \\ \mathbf{0} & \mathbf{B}_H & \mathbf{A}_H & \mathbf{0} & \dots \\ \mathbf{0} & \mathbf{0} & \mathbf{B}_H & \mathbf{A}_H & \dots \\ \vdots & \vdots & \vdots & \vdots & \ddots \end{pmatrix} \tag{F.6}$$

where

$$\mathbf{A}_1 = \begin{pmatrix} -2 & 0 \\ \\ -2c_2 & 0 \end{pmatrix} \tag{F.7}$$

describes the stability of the first uncoupled Landau-Stuart node, while

$$\mathbf{A}_H = \begin{pmatrix} -(2+K) & Kc_1 \\ \\ -(2c_2 + Kc_1) & -K \end{pmatrix}, \ \mathbf{B}_H = \begin{pmatrix} K & -Kc_1 \\ \\ Kc_1 & K \end{pmatrix} \tag{F.8}$$

originate from the other nodes ($j > 1$).

Using simple block matrices results one can show that

$$\det\left(\mathbf{J}_H - \lambda \mathbf{I}_{2\Omega}\right) = \det\left(\mathbf{A}_1 - \lambda \mathbf{I}_2\right) \left[\det\left(\mathbf{A}_H - \lambda \mathbf{I}_2\right)\right]^{\Omega - 1} \tag{F.9}$$

(where $\mathbf{I}_h$ is the $h \times h$ identity matrix) so that the eigenvalues of $\mathbf{J}_H$ are given by the ones of $\mathbf{A}_1$ and the ones of $\mathbf{A}_H$ (with multiplicity $\Omega - 1$).
We easily verifiy that $\mathbf{A}_1$ has eigenvalues $\lambda_\rho = -2$ and $\lambda_\theta = 0$ and consequently is stable. We are therefore interested in the eigenvalues λ_H of $\mathbf{A}_H$

that give

$$\lambda_H^{\pm} = -1 - K \pm \sqrt{1 - 2Kc_1c_2 - K^2c_1^2} \tag{F.10}$$

The real part of the largest eigenvalue λ_H^+ has two zeros for $K = 0$ and $K = K_{min}^H$ with

$$K_{min}^H = -\frac{2(1 + c_2c_1)}{1 + c_1^2} \tag{F.11}$$

We can determine the stability condition $\mathcal{R}\left[\lambda_H^+\right] < 0$ by the sign of K_{min}^H and of the small K expansion of equation (F.10),

$$\lambda_H^+ \approx -K(1 + c_1c_2) < 0 \tag{F.12}$$

, which gives the sign of the K derivative of $\mathcal{R}\left[\lambda_H^+\right]$ near $K = 0$. Note that they are both controlled by the sign of $1 + c_1c_2$, so that one immediatly obtains the homogeneous state stability condition given in the main text.

The splay states give rise to a slightly more complicated Jacobian matrices $\mathbf{J}_S^{(\bar{j})}$. The first $\bar{j}$ rows are identical to the ones of $\mathbf{J}_H$, while the following ones are obtained evaluating the linearized equation along the splay state part of the attractor. For instance, for $\bar{j} = 2$ we have

$$\mathbf{J}_S^{(2)} = \begin{pmatrix} \mathbf{A}_1 & \mathbf{0} & \mathbf{0} & \mathbf{0} & \dots \\ \mathbf{B}_H & \mathbf{A}_H & \mathbf{0} & \mathbf{0} & \dots \\ \mathbf{0} & \mathbf{B}_3 & \mathbf{A}_3 & \mathbf{0} & \dots \\ \mathbf{0} & \mathbf{0} & \mathbf{B}_4 & \mathbf{A}_4 & \dots \\ \vdots & \vdots & \vdots & \vdots & \ddots \end{pmatrix} \tag{F.13}$$

with

$$\mathbf{A}_j = \begin{pmatrix} (1-3\rho_j^2-K) & K\rho_{j-1}g(\phi_j) \\ \\ -\left(2c_2\rho_j + K\frac{\rho_{j-1}}{\rho_j}g(\phi_j)\right) & -K\frac{\rho_{j-1}}{\rho_j}f(\phi_j) \end{pmatrix} \tag{F.14}$$

and

$$\mathbf{B}_j = \begin{pmatrix} Kf(\phi_j) & -K\rho_j g(\phi_j) \\ \\ \frac{K}{\rho_j}g(\phi_j) & K\frac{\rho_{j-1}}{\rho_j}f(\phi_j) \end{pmatrix} \tag{F.15}$$

where functions g and f are defined in the main text in equations (5.4). Obviously, for $j \gg \bar{j}$ we have

$$\mathbf{A}_j \approx \mathbf{A}_\infty = \begin{pmatrix} (1-3\rho_\infty^2-K) & K\rho_\infty g(\phi_\infty) \\ \\ -\left(2c_2\rho_\infty + Kg(\phi_\infty)\right) & -Kf(\phi_\infty) \end{pmatrix} \tag{F.16}$$

and

$$\mathbf{B}_j \approx \mathbf{B}_\infty = \begin{pmatrix} Kf(\phi_\infty) & -K\rho_\infty g(\phi_\infty) \\ \\ \frac{K}{\rho_\infty}g(\phi_\infty) & Kf(\phi_\infty) \end{pmatrix} \tag{F.17}$$

Once again we have

$$\begin{aligned} \det\left(\mathbf{J}_S^{(\bar{j})} - \lambda\mathbf{I}_{2\Omega}\right) \;=\; & \det\left(\mathbf{A}_1 - \lambda\mathbf{I}_2\right)\left[\det\left(\mathbf{A}_H - \lambda\mathbf{I}_2\right)\right]^{\bar{j}-1} \\ & \prod_{j=\bar{j}+1}^{N}\left[\det\left(\mathbf{A}_j - \lambda\mathbf{I}_2\right)\right] \end{aligned} \tag{F.18}$$

so that to estimate the eigenvalues of $\mathbf{J}_S^{(\bar{j})}$ we also need to compute the eigenvalues of the matrices $\mathbf{A}_j$, evaluated on the splay attractor values ρ_j and ϕ_j obtained from the recurrence equations (5.3).

Appendix G

Nature of the noise

This appendix covers the nature of the stochastic correction for the system investigated in chapter 5. We shall demonstrate that the additive stochastic corrections we introduced in our system (see equation (5.8)) remains of the same kind in polar form. We first write the ordinary differential equations for the real and imaginary part of $W_j = X_j + iY_j$. After few lines of algebra we end up with

$$\begin{aligned}
\frac{\mathrm{d}X_j}{\mathrm{d}t} &= X_j + \left(X_j^2 + Y_j^2\right)\left(-X_j + c_2 Y_j\right) \\
&\quad + K\left(X_{j-1} - X_j + c_1\left(Y_j - Y_{j-1}\right)\right) \\
&\quad + \sigma\eta_j^X \qquad \text{(G.1)} \\
\frac{\mathrm{d}Y_j}{\mathrm{d}t} &= Y_j + \left(X_j^2 + Y_j^2\right)\left(-c_2 X_j - Y_j\right) \\
&\quad + K\left(Y_{j-1} - Y_j + c_1\left(X_{j-1} - X_j\right)\right) \\
&\quad + \sigma\eta_j^Y \qquad \text{(G.2)}
\end{aligned}$$

Writing in polar form $W_j{=}\rho_j \exp(i\theta_j)$ implies that $\rho_j{=}\sqrt{X_j^2+Y_j^2}$ and $\theta_j{=}$ Atan $\left(\frac{Y_j}{X_j}\right)$. In terms of O.D.E.s it means that

$$\rho_j \frac{\mathrm{d}\rho_j}{\mathrm{d}t} = X_j \frac{\mathrm{d}X_j}{\mathrm{d}t} + Y_j \frac{\mathrm{d}Y_j}{\mathrm{d}t} \tag{G.3a}$$

$$\rho_j^2 \frac{\mathrm{d}\theta_j}{\mathrm{d}t} = X_j \frac{\mathrm{d}Y_j}{\mathrm{d}t} - Y_j \frac{\mathrm{d}X_j}{\mathrm{d}t} \tag{G.3b}$$

We now want to obtain the Langevin equation for ρ_j and θ_j, this leads to

$$\begin{aligned} \rho_j \frac{\mathrm{d}\rho_j}{\mathrm{d}t} &= \rho_j^2 - \rho_j^4 + K\left(-\rho_j^2 + \rho_j\rho_{j-1} f(\phi_j)\right) \\ &\quad +\sigma\left(X_j \eta_j^X + Y_j \eta_j^Y\right) \end{aligned} \tag{G.4}$$

$$\begin{aligned} \rho_j^2 \frac{\mathrm{d}\theta_j}{\mathrm{d}t} &= -c_2\rho_j^4 + K\left(-c_1\rho_j^2 + \rho_j\rho_{j-1} g(\phi_j)\right) \\ &\quad +\sigma\left(X_j \eta_j^Y - Y_j \eta_j^X\right) \end{aligned} \tag{G.5}$$

where the auxiliary functions f and g have been introduced in equations (5.4). The sum of two Gaussian variable is itself a Gaussian variable, whose average value is the sum of the two previous average value while its variance is the quadratic sum of the variances. Therefore we can introduce two new Gaussian delta correlated and zero mean white noise variables ξ_j^ρ and ξ_j^θ such that their standard deviations are

$$\Sigma_{\rho,\theta} = \sqrt{X_j^2 + Y_j^2} = \rho_j \tag{G.6}$$

This leads to the final Langevin equations in polar form

$$\frac{\mathrm{d}\rho_j}{\mathrm{d}t} = \rho_j - \rho_j^3 + K\left(-\rho_j + \rho_{j-1} f(\phi_j)\right) + \sigma\xi_j^{\rho} \tag{G.7}$$

$$\frac{\mathrm{d}\theta_j}{\mathrm{d}t} = -c_2\rho_j^2 + K\left(-c_1 + \frac{\rho_{j-1}}{\rho_j} g(\phi_j)\right) + \frac{\sigma}{\rho_j}\xi_j^{\theta} \tag{G.8}$$

which display a multiplicative but delta correlated zero-average noisy term. In our power spectrum analysis, conducted expanding near the limit cycle solutions, this multiplicative component can be safely approximated by its limit cycle value, making the dominant noise component additive.

References

[1] A. Einstein. Investigations on the theory of the brownian motion, dover publications. *Dover Publications*, 1926. URL http://www.maths.usyd.edu.au/u/UG/SM/MATH3075/r/Einstein_1905.pdf.

[2] M. von Smoluchowski. *Annal of Physics*, 17(549), 1905.

[3] P. Langevin. *Comptes rendus*, 146(530), 1908.

[4] H. A. Kramers. Brownian motion in a field of force and the diffusion model of chemical reactions. *Physica*, 7(4):284 – 304, 1940. ISSN 0031-8914. doi: https://doi.org/10.1016/S0031-8914(40)90098-2. URL http://www.sciencedirect.com/science/article/pii/S0031891440900982.

[5] J. E. Moyal. Stochastic processes and statistical physics. *Journal of the Royal Statistical Society. Series B (Methodological)*, 11(2):150–210, 1949. ISSN 00359246. URL http://www.jstor.org/stable/2984076.

[6] A. A. Faisal, L. P. J. Selen, and D. M. Wolpert. Noise in the nervous system. *Nature Reviews Neuroscience*, 9:292, Apr 2008. URL https://doi.org/10.1038/nrn2258.

[7] L. M. Ward and P. E. Greenwood. Stochastic facilitation in the brain? *Journal of Statistical Mechanics: Theory and Experiment*, 2016(5):054033, 2016. URL http://stacks.iop.org/1742-5468/2016/i=5/a=054033.

[8] M. D. McDonnell and L. M. Ward. The benefits of noise in neural systems: bridging theory and experiment. *Nature Reviews Neuroscience*, 12:415, Jun 2011. URL https://doi.org/10.1038/nrn3061. Perspective.

[9] H. R. Wilson and J. D. Cowan. Excitatory and inhibitory interactions in localized populations of model neurons. *Biophys J*, 12(1):1–24, Jan 1972. ISSN 0006-3495. doi: 10.1016/S0006-3495(72)86068-5. URL https://www.ncbi.nlm.nih.gov/pubmed/4332108. 4332108[pmid].

[10] H. R. Wilson and J. D. Cowan. A mathematical theory of the functional dynamics of cortical and thalamic nervous tissue. *Kybernetik*, 13(2): 55–80, Sep 1973. ISSN 1432-0770. doi: 10.1007/BF00288786. URL https://doi.org/10.1007/BF00288786.

[11] D. T. Gillespie. Exact stochastic simulation of coupled chemical reactions. *The Journal of Physical Chemistry*, 81(25):2340–2361, 1977. doi: 10.1021/j100540a008. URL https://doi.org/10.1021/j100540a008.

[12] R. P. Boland, T. Galla, and A. J. McKane. How limit cycles and quasi-cycles are related in systems with intrinsic noise. *Journal of Statistical Mechanics: Theory and Experiment*, 2008(09):P09001, 2008. URL http://stacks.iop.org/1742-5468/2008/i=09/a=P09001.

[13] C. A. Lugo and A. J. McKane. Quasicycles in a spatial predator-prey model. *Phys. Rev. E*, 78:051911, Nov 2008. doi: 10.1103/PhysRevE.78.051911. URL https://link.aps.org/doi/10.1103/PhysRevE.78.051911.

[14] A. J. McKane and T. J. Newman. Predator-prey cycles from resonant amplification of demographic stochasticity. *Phys. Rev. Lett.*, 94:218102, Jun 2005. doi: 10.1103/PhysRevLett.94.218102. URL https://link.aps.org/doi/10.1103/PhysRevLett.94.218102.

[15] J. H. Schwartz Kandel, E. R. and T. M. Jessell. Principles of neural science. 2000. URL https://neurology.mhmedical.com/book.aspx?bookID=1049.

[16] C. R. Laing. Chimeras in networks with purely local coupling. *Phys. Rev. E*, 92:050904, Nov 2015. doi: 10.1103/PhysRevE.92.050904. URL https://link.aps.org/doi/10.1103/PhysRevE.92.050904.

[17] C. Laing. Spiral waves in nonlocal equations. *SIAM Journal on Applied Dynamical Systems*, 4(3):588–606, 2005. doi: 10.1137/040612890. URL https://doi.org/10.1137/040612890.

[18] D. Pazó and E. Montbrió. Low-dimensional dynamics of populations of pulse-coupled oscillators. *Phys. Rev. X*, 4:011009, Jan 2014. doi: 10.1103/PhysRevX.4.011009. URL https://link.aps.org/doi/10.1103/PhysRevX.4.011009.

[19] E. Montbrió, D. Pazó, and A. Roxin. Macroscopic description for networks of spiking neurons. *Phys. Rev. X*, 5:021028, Jun 2015. doi: 10.1103/PhysRevX.5.021028. URL https://link.aps.org/doi/10.1103/PhysRevX.5.021028.

[20] I. Ratas and K. Pyragas. Macroscopic self-oscillations and aging transition in a network of synaptically coupled quadratic integrate-and-fire neurons. *Phys. Rev. E*, 94:032215, Sep 2016. doi: 10.1103/PhysRevE.94.032215. URL https://link.aps.org/doi/10.1103/PhysRevE.94.032215.

[21] A. Destexhe and T. J. Sejnowski. The wilson–cowan model, 36 years later. *Biological Cybernetics*, 101(1):1–2, Jul 2009. ISSN 1432-0770. doi: 10.1007/s00422-009-0328-3. URL https://doi.org/10.1007/s00422-009-0328-3.

[22] V. Shusterman and W. C. Troy. From baseline to epileptiform activity: A path to synchronized rhythmicity in large-scale neural networks. *Phys. Rev. E*, 77:061911, Jun 2008. doi: 10.1103/PhysRevE.77.061911. URL https://link.aps.org/doi/10.1103/PhysRevE.77.061911.

[23] Z. P. Kilpatrick. *Wilson-Cowan Model*, pages 1–5. Springer New York, New York, NY, 2013. ISBN 978-1-4614-7320-6. doi: 10.1007/978-1-4614-7320-6_80-1. URL https://doi.org/10.1007/978-1-4614-7320-6_80-1.

[24] M. S. Bartlett. Measles periodicity and community size. *Journal of the Royal Statistical Society. Series A (General)*, 120(1):48–70, 1957. ISSN 00359238. URL http://www.jstor.org/stable/2342553.

[25] A. J. McKane and T. J. Newman. Predator-prey cycles from resonant amplification of demographic stochasticity. *Phys. Rev. Lett.*, 94:218102, Jun 2005. doi: 10.1103/PhysRevLett.94.218102. URL https://link.aps.org/doi/10.1103/PhysRevLett.94.218102.

[26] T. Dauxois, F. Di Patti, D. Fanelli, and A. J. McKane. Enhanced stochastic oscillations in autocatalytic reactions. *Phys. Rev. E*, 79: 036112, Mar 2009. doi: 10.1103/PhysRevE.79.036112. URL https://link.aps.org/doi/10.1103/PhysRevE.79.036112.

[27] C. A. Lugo and A. J. McKane. Quasicycles in a spatial predator-prey model. *Phys. Rev. E*, 78:051911, Nov 2008. doi: 10.1103/PhysRevE.78.051911. URL https://link.aps.org/doi/10.1103/PhysRevE.78.051911.

[28] T. Butler and N. Goldenfeld. Robust ecological pattern formation induced by demographic noise. *Phys. Rev. E*, 80:030902, Sep 2009. doi: 10.1103/PhysRevE.80.030902. URL https://link.aps.org/doi/10.1103/PhysRevE.80.030902.

[29] P. de Anna, F. Di Patti, D. Fanelli, A. J. McKane, and T. Dauxois. Spatial model of autocatalytic reactions. *Phys. Rev. E*, 81:056110, May 2010. doi: 10.1103/PhysRevE.81.056110. URL https://link.aps.org/doi/10.1103/PhysRevE.81.056110.

[30] T. Biancalani, D. Fanelli, and F. Di Patti. Stochastic turing patterns in the brusselator model. *Phys. Rev. E*, 81:046215, Apr 2010. doi: 10.1103/PhysRevE.81.046215. URL https://link.aps.org/doi/10.1103/PhysRevE.81.046215.

[31] T. E. Woolley, R. E. Baker, E. A. Gaffney, P. K. Maini, and S. Seirin-Lee. Effects of intrinsic stochasticity on delayed reaction-diffusion patterning systems. *Phys. Rev. E*, 85:051914, May 2012. doi: 10.1103/PhysRevE.85.051914. URL https://link.aps.org/doi/10.1103/PhysRevE.85.051914.

[32] T. C. Butler, M. Benayoun, E. Wallace, W. van Drongelen, N. Goldenfeld, and J. Cowan. Evolutionary constraints on visual cortex architecture from the dynamics of hallucinations. *Proceedings of the National Academy of Sciences*, 109(2):606–609, 2012. ISSN 0027-8424. doi: 10.1073/pnas.1118672109. URL http://www.pnas.org/content/109/2/606.

[33] P. C. Bressloff. Metastable states and quasicycles in a stochastic wilson-cowan model of neuronal population dynamics. *Phys. Rev. E*, 82:051903,

Nov 2010. doi: 10.1103/PhysRevE.82.051903. URL https://link.aps.org/doi/10.1103/PhysRevE.82.051903.

[34] I. Goychuk and A. Goychuk. Stochastic wilsoncowan models of neuronal network dynamics with memory and delay. *New Journal of Physics*, 17 (4):045029, 2015. URL http://stacks.iop.org/1367-2630/17/i=4/a=045029.

[35] N. G. Van Kampen. Stochastic processes in physics and chemistry (third edition). North-Holland Personal Library, pages 193 – 218. Elsevier, Amsterdam, third edition edition, 2007. doi: https://doi.org/10.1016/B978-044452965-7/50011-8. URL http://www.sciencedirect.com/science/article/pii/B9780444529657500118.

[36] Stochastic pattern formation and spontaneous polarisation: The linear noise approximation and beyond. *Bulletin of Mathematical Biology*, 76 (4):895–921, 4 2014. ISSN 0092-8240. doi: 10.1007/s11538-013-9827-4.

[37] T. Biancalani, L. Dyson, and A. J. McKane. Noise-induced bistable states and their mean switching time in foraging colonies. *Phys. Rev. Lett.*, 112:038101, Jan 2014. doi: 10.1103/PhysRevLett.112.038101. URL https://link.aps.org/doi/10.1103/PhysRevLett.112.038101.

[38] F. Jafarpour, T. Biancalani, and N. Goldenfeld. Noise-induced mechanism for biological homochirality of early life self-replicators. *Phys. Rev. Lett.*, 115:158101, Oct 2015. doi: 10.1103/PhysRevLett.115.158101. URL https://link.aps.org/doi/10.1103/PhysRevLett.115.158101.

[39] T. Biancalani and M. Assaf. Genetic toggle switch in the absence of cooperative binding: Exact results. *Phys. Rev. Lett.*, 115:208101, Nov 2015. doi: 10.1103/PhysRevLett.115.208101. URL https://link.aps.org/doi/10.1103/PhysRevLett.115.208101.

[40] H. Risken. *The Fokker-Planck Equation: Methods of Solution and Applications*. Springer Berlin Heidelberg, Berlin, Heidelberg, 1984. ISBN 978-3-642-96807-5. doi: 10.1007/978-3-642-96807-5_4. URL https://doi.org/10.1007/978-3-642-96807-5_4.

[41] C. W. Gardiner. *Handbook of stochastic methods for physics, chemistry and the natural sciences*, volume 13 of *Springer Series in Synergetics*. Springer-Verlag, Berlin, third edition, 2004. ISBN 3-540-20882-8.

[42] P. E. Kloeden and E Platen. Numerical solution of stochastic differential equations. *ZAMM - Journal of Applied Mathematics and Mechanics / Zeitschrift fr Angewandte Mathematik und Mechanik*, 74(8):332–332. doi: 10.1002/zamm.19940740806. URL https://onlinelibrary.wiley.com/doi/abs/10.1002/zamm.19940740806.

[43] G.A. Pavliotis and A. Stuart. *Multiscale Methods: Averaging and Homogenization*. Texts in Applied Mathematics. Springer New York, 2008. ISBN 9780387738284. URL https://books.google.fr/books?id=qIaD19q7Tl8C.

[44] Johnson A. Lewis J. Raff M. Roberts K. Alberts, B. and P. Walter. Molecular biology of the cell. 4th edition. *Annals of Botany*, 91(3):401–401, Feb 2003. ISSN 0305-7364. doi: 10.1093/aob/mcg023. URL https://www.ncbi.nlm.nih.gov/pmc/articles/PMC4244961/. PMC4244961[pmcid].

[45] A. Pikovsky, M. G. Rosenblum, and J. Kurths. *Synchronization, A Universal Concept in Nonlinear Sciences*. Cambridge University Press, 2001.

[46] L. L. Gollo and M. Breakspear. The frustrated brain: from dynamics on motifs to communities and networks. *Philosophical Transactions of the Royal Society of London B: Biological Sciences*, 369(1653), 2014. ISSN 0962-8436. doi: 10.1098/rstb.2013.0532. URL http://rstb.royalsocietypublishing.org/content/369/1653/20130532.

[47] V. Nicosia, M. Valencia, M. Chavez, A. Díaz-Guilera, and V. Latora. Remote synchronization reveals network symmetries and functional modules. *Phys. Rev. Lett.*, 110:174102, Apr 2013. doi: 10.1103/PhysRevLett.110.174102. URL https://link.aps.org/doi/10.1103/PhysRevLett.110.174102.

[48] J. Albert and M. Rooman. Dynamic modeling of gene expression in prokaryotes: application to glucose-lactose diauxie in escherichia coli.

Systems and Synthetic Biology, 5(1):33–43, Jun 2011. ISSN 1872-5333. doi: 10.1007/s11693-011-9079-2. URL https://doi.org/10.1007/s11693-011-9079-2.

[49] J. Hasty, D. McMillen, F. Isaacs, and J. J. Collins. Computational studies of gene regulatory networks: in numero molecular biology. *Nature Reviews Genetics*, 2:268, Apr 2001. URL https://doi.org/10.1038/35066056. Review Article.

[50] M. B. Elowitz and S. Leibler. A synthetic oscillatory network of transcriptional regulators. *Nature*, 403:335, Jan 2000. URL https://doi.org/10.1038/35002125.

[51] F. J. Isaacs, J. Hasty, C. R. Cantor, and J. J. Collins. Prediction and measurement of an autoregulatory genetic module. *Proceedings of the National Academy of Sciences*, 100(13):7714–7719, 2003. ISSN 0027-8424. doi: 10.1073/pnas.1332628100. URL http://www.pnas.org/content/100/13/7714.

[52] G. Caldarelli and A. Chessa. *Data Science and Complex Networks: Real Case Studies with Python*. Oxford University Press, Oxford, 2016. ISBN 9780199639601. URL http://www.oxfordscholarship.com/10.1093/acprof:oso/9780199639601.001.0001/acprof-9780199639601.

[53] S. Boccaletti, G. Bianconi, R. Criado, C. I. Del Genio, Jesús Gómez-Gardeñes, M. Romance, I. Sendiña-Nadal, Z. Wang, and M. Zanin. The structure and dynamics of multilayer networks. *CoRR*, abs/1407.0742, 2014.

[54] S. Boccaletti, V. Latora, Y. Moreno, M. Chavez, and D. U. Hwang. Complex networks: Structure and dynamics. *Physics Reports*, 424 (4):175 – 308, 2006. ISSN 0370-1573. doi: https://doi.org/10.1016/j.physrep.2005.10.009. URL http://www.sciencedirect.com/science/article/pii/S037015730500462X.

[55] P. Fernández and R. V. Solé. *The Role of Computation in Complex Regulatory Networks*, pages 206–225. Springer US, Boston, MA, 2006. doi: 10.1007/0-387-33916-7_12. URL https://doi.org/10.1007/0-387-33916-7_12.

[56] R. V. Sol and S. Valverde. Are network motifs the spandrels of cellular complexity? *Trends in Ecology & Evolution*, 21(8):419 – 422, 2006. ISSN 0169-5347. doi: https://doi.org/10.1016/j.tree.2006.05.013. URL http://www.sciencedirect.com/science/article/pii/S0169534706001674.

[57] J. Maca, F. Posas, and R. V. Sol. Distributed computation: the new wave of synthetic biology devices. *Trends in Biotechnology*, 30 (6):342 – 349, 2012. ISSN 0167-7799. doi: https://doi.org/10.1016/j.tibtech.2012.03.006. URL http://www.sciencedirect.com/science/article/pii/S0167779912000388.

[58] T. Biancalani, D. Fanelli, and F. Di Patti. Stochastic turing patterns in the brusselator model. *Phys. Rev. E*, 81:046215, Apr 2010. doi: 10.1103/PhysRevE.81.046215. URL https://link.aps.org/doi/10.1103/PhysRevE.81.046215.

[59] Norbert Wiener. Coherency matrices and quantum. *Journal of Mathematics and Physics*, 7(1-4):109–125, 1928. doi: 10.1002/sapm192871109. URL https://onlinelibrary.wiley.com/doi/abs/10.1002/sapm192871109.

[60] J. D. Challenger and A. J. McKane. Synchronization of stochastic oscillators in biochemical systems. *Phys. Rev. E*, 88:012107, Jul 2013. doi: 10.1103/PhysRevE.88.012107. URL https://link.aps.org/doi/10.1103/PhysRevE.88.012107.

[61] L. N. Trefethen, A. E. Trefethen, S. C. Reddy, and T. A. Driscoll. Hydrodynamic stability without eigenvalues. *Science*, 261(5121):578–584, 1993. ISSN 0036-8075. doi: 10.1126/science.261.5121.578. URL http://science.sciencemag.org/content/261/5121/578.

[62] M. A. Lewis and P. Kareiva. Allee dynamics and the spread of invading organisms. *Theoretical Population Biology*, 43(2):141 – 158, 1993. ISSN 0040-5809. doi: https://doi.org/10.1006/tpbi.1993.1007. URL http://www.sciencedirect.com/science/article/pii/S0040580983710075.

[63] R. J. Deissler. External noise and the origin and dynamics of structure in convectively unstable systems. *Journal of Statistical Physics*, 54(5):

1459–1488, Mar 1989. ISSN 1572-9613. doi: 10.1007/BF01044729. URL https://doi.org/10.1007/BF01044729.

[64] S. Lepri, A. Politi, and A. Torcini. Chronotopic lyapunov analysis. i. a detailed characterization of 1d systems. *Journal of Statistical Physics*, 82(5):1429–1452, Mar 1996. ISSN 1572-9613. doi: 10.1007/BF02183390. URL https://doi.org/10.1007/BF02183390.

[65] S. Lepri, A. Politi, and A. Torcini. Chronotopic lyapunov analysis: Ii. toward a unified approach. *Journal of Statistical Physics*, 88(1):31–45, Jul 1997. doi: 10.1007/BF02508463. URL https://doi.org/10.1007/BF02508463.

[66] A. Kenfack Jiotsa, A. Politi, and A. Torcini. Convective lyapunov spectra. *Journal of Physics A: Mathematical and Theoretical*, 46(25):254013, 2013. URL http://stacks.iop.org/1751-8121/46/i=25/a=254013.

[67] J. Schnakenberg. Network theory of microscopic and macroscopic behavior of master equation systems. *Rev. Mod. Phys.*, 48:571–585, Oct 1976. doi: 10.1103/RevModPhys.48.571. URL https://link.aps.org/doi/10.1103/RevModPhys.48.571.

[68] J. L. Lebowitz and H. Spohn. A gallavotti–cohen-type symmetry in the large deviation functional for stochastic dynamics. *Journal of Statistical Physics*, 95(1):333–365, Apr 1999. doi: 10.1023/A:1004589714161. URL https://doi.org/10.1023/A:1004589714161.

[69] T. Tomé. Entropy production in nonequilibrium systems described by a fokker-planck equation. *Brazilian Journal of Physics*, 36(4):1285–1289, Dec 2006. URL https://dx.doi.org/10.1590/S0103-97332006000700029.

[70] T. Tomé and M. J. de Oliveira. Entropy production in irreversible systems described by a fokker-planck equation. *Phys. Rev. E*, 82:021120, Aug 2010. doi: 10.1103/PhysRevE.82.021120. URL https://link.aps.org/doi/10.1103/PhysRevE.82.021120.

[71] Di Patti, F., Fanelli, D., and Carletti, T. Drift-induced benjamin-feir instabilities. *EPL*, 114(6):68003, 2016. doi: 10.1209/0295-5075/114/68003. URL https://doi.org/10.1209/0295-5075/114/68003.

[72] T. Brooke Benjamin and J. E. Feir. The disintegration of wave trains on deep water. *Journal of Fluid Mechanics*, 27(3):417430, 1967. doi: 10.1017/S002211206700045X.

[73] M. Asllani, T. Biancalani, D. Fanelli, and A. J. McKane. The linear noise approximation for reaction-diffusion systems on networks. *The European Physical Journal B*, 86(11):476, Nov 2013. doi: 10.1140/epjb/e2013-40570-8. URL https://doi.org/10.1140/epjb/e2013-40570-8.

[74] A. J. McKane, T. Biancalani, and T. Rogers. Stochastic pattern formation and spontaneous polarisation: The linear noise approximation and beyond. *Bulletin of Mathematical Biology*, 76(4):895–921, Apr 2014. ISSN 1522-9602. doi: 10.1007/s11538-013-9827-4. URL https://doi.org/10.1007/s11538-013-9827-4.

[75] J. D. Challenger, R. Burioni, and D. Fanelli. Turing-like instabilities from a limit cycle. *Phys. Rev. E*, 92:022818, Aug 2015. doi: 10.1103/PhysRevE.92.022818. URL https://link.aps.org/doi/10.1103/PhysRevE.92.022818.

[76] M. G. Neubert and H. Caswell. Allternatives to resilience for measuring the responses of ecological systems to perturbations. *Ecology*, 78(3):653–665. doi: 10.1890/0012-9658(1997)078[0653:ATRFMT]2.0.CO;2. URL https://esajournals.onlinelibrary.wiley.com/doi/abs/10.1890/0012-9658%281997%29078%5B0653%3AATRFMT%5D2.0.CO%3B2.

[77] S. Nicoletti, N. Zagli, D. Fanelli, R. Livi, T. Carletti, and G. Innocenti. Non-normal amplification of stochastic quasicycles. *Phys. Rev. E*, 98:032214, Sep 2018. doi: 10.1103/PhysRevE.98.032214. URL https://link.aps.org/doi/10.1103/PhysRevE.98.032214.

[78] T. Biancalani, F. Jafarpour, and N. Goldenfeld. Giant amplification of noise in fluctuation-induced pattern formation. *Phys. Rev. Lett.*, 118:018101, Jan 2017. doi: 10.1103/PhysRevLett.118.018101. URL https://link.aps.org/doi/10.1103/PhysRevLett.118.018101.

[79] Hans G. Othmer. *SIAM Review*, 24(4):483–485, 1982. ISSN 00361445. URL http://www.jstor.org/stable/2029552.

[80] M. C. Cross and P. C. Hohenberg. Pattern formation outside of equilibrium. *Rev. Mod. Phys.*, 65:851–1112, Jul 1993. doi: 10.1103/RevModPhys.65.851. URL https://link.aps.org/doi/10.1103/RevModPhys.65.851.

[81] M. Asllani, R. Lambiotte, and T. Carletti. Structure and dynamical behaviour of non-normal networks. *ArXiv e-prints*, March 2018.

[82] K. Kaneko. Spatiotemporal chaos in one- and two-dimensional coupled map lattices. *Physica D: Nonlinear Phenomena*, 37(1):60 – 82, 1989. ISSN 0167-2789. doi: https://doi.org/10.1016/0167-2789(89)90117-6. URL http://www.sciencedirect.com/science/article/pii/0167278989901176.

[83] C. Zankoc, T. Biancalani, D. Fanelli, and R. Livi. Diffusion approximation of the stochastic wilsoncowan model. *Chaos, Solitons & Fractals*, 103:504 – 512, 2017. ISSN 0960-0779. doi: https://doi.org/10.1016/j.chaos.2017.07.010. URL http://www.sciencedirect.com/science/article/pii/S0960077917302886.

[84] C. Zankoc, D. Fanelli, F. Ginelli, and R. Livi. Intertangled stochastic motifs in networks of excitatory-inhibitory units. *Phys. Rev. E*, 96:022308, Aug 2017. doi: 10.1103/PhysRevE.96.022308. URL https://link.aps.org/doi/10.1103/PhysRevE.96.022308.

[85] D. Fanelli, F. Ginelli, R. Livi, N. Zagli, and C. Zankoc. Noise-driven neuromorphic tuned amplifier. *Phys. Rev. E*, 96:062313, Dec 2017. doi: 10.1103/PhysRevE.96.062313. URL https://link.aps.org/doi/10.1103/PhysRevE.96.062313.

[86] J. L. Doob. Markoff chains–denumerable case. *Transactions of the American Mathematical Society*, 58(3):455–473, 1945. ISSN 00029947. URL http://www.jstor.org/stable/1990339.

[87] R. Livi and P. Politi. *Nonequilibrium Statistical Physics: A Modern Perspective*. Cambridge University Press, 2017. doi: 10.1017/9781107278974.

[88] R. Mannella and P. V. E. McClintock. Itô versus stratonovitch: 30 years later. *Fluctuation and Noise Letters*, 11(01):1240010, 2012.

doi: 10.1142/S021947751240010X. URL https://doi.org/10.1142/S021947751240010X.

[89] N. G. van Kampen. Itô versus stratonovich. *Journal of Statistical Physics*, 24(1):175–187, Jan 1981. ISSN 1572-9613. doi: 10.1007/BF01007642. URL https://doi.org/10.1007/BF01007642.

[90] Sekimoto K. Stochastic energetics. *Biophysics*, 37:S72, oct 1997. ISSN 05824052. URL https://ci.nii.ac.jp/naid/110001152186/en/.